DEFECT CHEMISTRY AND HARDENING OF FERROELECTRIC COBALT-DOPED BISMUTH FERRITE CERAMICS

Maja Makarovič

Doctoral Dissertation
Jožef Stefan International Postgraduate School
Ljubljana, Slovenia

Supervisor: Prof. Dr. Tadej Rojac, Jožef Stefan Institute, Electronic Ceramics Department, Ljubljana, Slovenia
Co-Supervisor: Prof. Dr. Sverre Magnus Selbach, Norwegian University of Science and Technology, Department of Materials Science and Engineering, Trondheim, Norway

Evaluation Board:
Asst. Prof. Dr. Matjaž Spreitzer, Chair, Jožef Stefan Institute, Advanced Materials Department, Ljubljana, Slovenia
Prof. Dr. Tor Grande, Member, Norwegian University of Science and Technology, Department of Materials Science and Engineering, Trondheim, Norway
Prof. Dr. Klaus Reichmann, Member, Graz University of Technology, Institute of Chemistry and Technology of Materials, Graz, Austria

MEDNARODNA PODIPLOMSKA ŠOLA JOŽEFA STEFANA
JOŽEF STEFAN INTERNATIONAL POSTGRADUATE SCHOOL

Maja Makarovič

DEFECT CHEMISTRY AND HARDENING OF FERROELECTRIC COBALT-DOPED BISMUTH FERRITE CERAMICS

Doctoral Dissertation

KEMIJA DEFEKTOV IN UTRJEVANJE FEROELEKTRIČNE BIZMUT-FERITNE KERAMIKE DOPIRANE S KOBALTOM

Doktorska disertacija

Supervisor: Prof. Dr. Tadej Rojac

Co-Supervisor: Prof. Dr. Sverre Magnus Selbach

Ljubljana, Slovenia, November 2020

"Success is not final, failure is not fatal: it is the courage to continue that counts."

Winston S. Churchill

Acknowledgments

This work would not have been possible without the help and support of many people.

First of all, I would like to express my deepest gratitude to my supervisor Prof. Dr. Tadej Rojac for his support, guidance, the critical evaluation of my work and the extensive knowledge he has shared with me all these years. I would also like to thank my co-supervisor Prof. Dr. Sverre Magnus Selbach for welcoming me to the Norwegian University of Science and Technology (NTNU) in Trondheim, and moreover, for all the patience and helpfulness while educating me about first-principle calculations. In addition, I would like to acknowledge the department leader Prof. Dr. Barbara Malič for giving me the opportunity to work at the Electronic Ceramics Department – K5 and for always taking care of us, her employees.

Next, I would like to thank Prof. Dr. Andreja Benčan and Prof. Dr. Goran Dražić for the (S)TEM analyses and Asst. prof. Dr. Hana Uršič for the AFM/PFM analysis. Many thanks go to Silvo Drnovšek for all kinds of technical support, Brigita Kmet for TEM sample preparation and Jena Cilenšek for thermal analysis measurements. The laboratory work was done faster with the great support of "my" student Katarina Žiberna. So, thank you. I appreciate the help and suggestions from current and former PhD students, especially Uroš Prah, Matej Šadl, Dr. Andraž Bradeško and Dr. Marko Vrabelj. I am grateful for all life-related rather than scientific debates with dr. Kostja Makarovič, Asst. Prof. Dr. Danjela Kuščer, Asst. Prof. Dr. Mojca Otoničar and Tamara Matevc. I would like to thank my awesome officemates (now already former) Dr. Tanja Vrabelj (née Pečnik) and Dr. Lovro Fulanović for the educational, relaxing and humorous atmosphere in the office. My special thanks are extended to all other co-workers from K5.

The contributions were not limited solely to K5 but also to other departments of the Jožef Stefan Institute. I would like to thank Assoc. Prof. Dr. Andrej Zorko for all the effort he has put into upgrading the EPR spectrometer and the time for recording the spectra. I appreciate the collaboration with Prof. Dr. Slavko Bernik, Dr. Darko Hanžel, Prof. Dr. Janez Kovač and Prof. Dr. Iztok Arčon. Next, I would like to acknowledge Edi Kranjc from the Slovenian National Institute of Chemistry for the X-ray measurements.

I would also like to thank Tadeja, Sergeja and Maša from Secretariat of Jozef Stefan International Postgraduate School for all the help and information regarding the study process.

I had the opportunity for a 6-month scientific visit to NTNU in Trondheim, which was an amazing experience. I would like to thank Assoc. Prof. Dr. Julia Glaum for the help with conductivity measurements and Dr. Didrik René Småbråten for all the patience, effort and nice explanations he shared with me about DFT calculations. I am grateful to Dr. Nikola Kanas for helping me with the Seebeck and conductivity measurements, and especially for making lab work even more enjoyable and amusing. I would like to thank my

great flatmate at Voll Studentby Clas Olaf Steinbru Andersen for all the walks and talks, and of course, for introducing me to cross-country skiing and Norsemen.

Next, I would like to thank Dr. Jurij Koruza for being my host during my 1-month research visit to the Technical University of Darmstadt and for all the exciting ideas he has shared with me. I deeply appreciate the help of Mihail Slabki and Christopher Schröck with the resonance measurements. I would also like to acknowledge Prof. Dr. Andreas Klein for fruitful discussions on point defects.

From the financial point of view, this work was supported by the Slovenian Research Agency, under grants P2-0105, PR-08350 and PR-08298. I would also like to acknowledge JECS Trust (Contract No. 2017298) for enabling the research visit to NTNU. UNINETT Sigma2 in Norway is acknowledged for computational resources for the DFT calculations through the project NN9264k.

I would also like to thank publishing houses for giving me a copyright permission to reuse some of the material published in their journals.

Apart from people that were somehow "directly" involved in the creation of this thesis, I would like to acknowledge people that contributed in another, "less scientific" way. Many thanks go to the best neighbors Anita and Gorgi for always welcoming me in their home and for all the fun. I deeply acknowledge my dearest friends Almina, Ana and Lovro for always being there for me, making the difficult times easier and the good times unforgettable.

Fortunately, I have the luxury of having a lovely family. I am grateful to my caring and protective brother Srđan, to my mother and father for their love and support and for showing me that it is important to fight for what you believe in, and especially for loved ones. I am so grateful to my uncle for giving my mother a second chance at life and for comforting me at difficult times.

Finally, I would like to thank my Urban for understanding and supporting me and for all the warmth and love.

Abstract

Bismuth ferrite, $BiFeO_3$ (BFO), has been recognized as a promising lead-free material for high-temperature piezoelectric applications due to its high Curie temperature of 825 °C. However, the practical use of BFO has been limited in particular by its elevated electrical conductivity. In addition, BFO shows the characteristics of ferroelectric hardening, reflected in pinched and biased polarization hysteresis loops and aging behavior. These phenomena have so far been explained by the presence of different types of point defects, including bismuth vacancies (V_{Bi}'''), oxygen vacancies ($V_O^{\bullet\bullet}$), Fe^{2+} (Fe_{Fe}') and Fe^{4+} ($Fe_{Fe}^{\bullet}$), as well as defect complexes, such as $V_{Bi}''' - V_O^{\bullet\bullet}$, $Fe_{Fe}' - V_O^{\bullet\bullet}$ and $V_{Bi}''' - Fe_{Fe}^{\bullet}$ (defects are given in Kröger-Vink notation). Despite being of key importance for designing the functional properties of BFO-based materials for high-temperature applications (>250 °C), the true origin and the complex inter-relationships between the electrical conductivity, point defects and hardening in BFO remains unclear and calls for a systematic study.

The objective of this PhD study was to controllably introduce point defects in BFO and investigate their influence on the electrical conductivity and domain-wall-pinning effects. This was achieved by introducing a Co dopant into the BFO along with post-annealing in different oxygen partial pressures.

All the $Bi(Fe_{1-x}Co_x)O_3$ ceramics contained comparable amounts of secondary phases (<1 wt%). It was found that the conductivity and hardening, the latter observed from polarization-electric-field hysteresis loops and the mechanical quality factor, increase with increasing Co concentration. The effect was attributed to the increased concentration of $V_O^{\bullet\bullet}$ and $Fe_{Fe}^{\bullet}$, hence it was concluded that Co acts as acceptor (Co_{Fe}').

The domain switching was impeded after annealing the ceramics in N_2, which was primarily attributed to the increased concentration of $V_O^{\bullet\bullet}$ and possibly Co_{Fe}'. *In-situ* measurements of the electrical conductivity and Seebeck coefficient demonstrated the p-type conductivity; however, the fast redox kinetics upon isothermal switching between O_2 and N_2 atmospheres gave an indication of the local redox reactions. This was further confirmed by conductive atomic force microscopy (c-AFM) analyses, which revealed that the conductivity of the domain walls (DWs) and grain boundaries is on average lower after annealing in N_2, thus demonstrating their p-type character. Furthermore, scanning transmission electron microscopy analyses confirmed the presence of V_{Bi}''' and $Fe_{Fe}^{\bullet}$ at the DWs in as-sintered samples and a reduced $Fe_{Fe}^{\bullet}$ concentration after N_2 annealing. In addition, the electron paramagnetic resonance confirmed the presence of $Co_{Fe}' - V_O^{\bullet\bullet}$ defect complexes. The tendency of $V_O^{\bullet\bullet}$ to be close to Co was further demonstrated by first-principle calculations, giving strong indications that Co acts as an acceptor, i.e., Co_{Fe}'.

Finally, the study showed that $Co_{Fe}' - V_O^{\bullet\bullet}$ defect complexes play the key role in the hardening behavior under switching conditions. On the other hand, the sub-switching converse piezoelectric response, in particular the large piezoelectric nonlinearity and hysteresis measured at low (Hz and sub-Hz) driving field frequencies, was found to be dominated by the p-type conductivity and thus $Fe_{Fe}^{\bullet}$ defects. The results thus point to a complex role of point defects where different types of defects can control the macroscopic response depending on the driving field conditions (amplitude and frequency).

Povzetek

Bizmutov ferit, $BiFeO_3$ (BFO), je pritegnil pozornost zaradi visoke Curiejeve temperature (~825 °C), ki mu daje potencial za uporabo v visokotemperaturnih piezoelektričnih aplikacijah. Kljub obetavnim lastnostim je uporaba tega materiala omejena predvsem zaradi visoke električne prevodnosti. Poleg tega ima preklapljanje domenskih sten v BFO karakteristike feroelektričnega utrjevanja, kar se kaže kot vpetost in zamik feroelektrične zanke. Takšno obnašanje se pripisuje raznim točkastim defektom, npr. bizmutovim vrzelim ($V_{Bi}^{'''}$), kisikovim vrzelim ($V_O^{\bullet\bullet}$), Fe^{2+} ($Fe_{Fe}^{'}$) in Fe^{4+} ($Fe_{Fe}^{\bullet}$), prav tako pa tudi kompleksom defektov, npr. $V_{Bi}^{'''} - V_O^{\bullet\bullet}$, $Fe_{Fe}^{'} - V_O^{\bullet\bullet}$, $V_{Bi}^{'''} - Fe_{Fe}^{\bullet}$. Vzrok za visoko električno prevodnost in feroelektrično utrjevanje v BFO keramiki torej ostaja nepojasnjen in kliče po sistematični študiji. Razumevanje teh mehanizmov bi lahko pomagalo pri načrtovanju funkcionalnih lastnosti keramike na osnovi BFO za visokotemperaturne aplikacije (>~250 °C).

Cilj raziskave je bil nadzorovano vnesti točkaste defekte v BFO in raziskati njihov vpliv na funkcionalne lastnosti materiala, predvsem na električno prevodnost in vpenjanje domenskih sten. To smo dosegli z dodatkom kobalta (Co) kot dopanta v BFO in naknadnim žganjem keramike pri različnih parcialnih tlakih kisika.

Vse sestave $Bi(Fe_{1-x}Co_x)O_3$ keramike so vsebovale primerljivo količino sekundarnih faz (<1 ut.%). Električna prevodnost in utrjevanje keramike, slednje opaženo iz preklapljanja feroelektričnih domen in piezoelektričnega odziva, je naraščalo s koncentracijo dopanta. To smo pripisali povečani koncentraciji $V_O^{\bullet\bullet}$ in $Fe_{Fe}^{\bullet}$, na podlagi česar smo zaključili, da se Co obnaša kot akceptor ($Co_{Fe}^{'}$).

Ugotovili smo, da je preklapljanje feroelektričnih domen oteženo po žganju v N_2, kar smo pripisali predvsem povečani koncentraciji $V_O^{\bullet\bullet}$ (in tudi $Co_{Fe}^{'}$). *In-situ* meritve električne prevodnosti in Seebeckovega koeficienta so potrdile prevodnost tipa p, vendar je hitra kinetika redoks reakcije nakazala na lokalizirane procese redukcije.

Lokalne meritve prevodnosti z uporabo mikroskopa na atomsko silo so pokazale, da se delež prevodnih domenskih sten in mej med zrni v povprečju zmanjša po žganju v N_2, kar potrjuje njihov značaj tipa p pa tudi lokalizacijo redoks procesov. Pri preiskavi domenskih sten z vrstičnim presevnim elektronskim mikroskopom smo ugotovili prisotnost $V_{Bi}^{'''}$ and $Fe_{Fe}^{\bullet}$ v sintranem vzorcu in zmanjšano koncentracijo $Fe_{Fe}^{\bullet}$ v vzorcu žganem v N_2. Z elektronsko paramagnetno resonanco smo identificirali komplekse defektov $Co_{Fe}^{'} - V_O^{\bullet\bullet}$. Modeliranje s teorijo gostotnega funkcionala v BFO keramiki dopirani s Co je potrdilo, da želijo biti $V_O^{\bullet\bullet}$ čim bližje Co centrov, kar je tudi močen indikator, da se Co obnaša kot akceptorski dopant, t.j., $Co_{Fe}^{'}$.

Rezultati raziskave kažejo, da imajo pri pogojih, pod katerimi pride do preklapljanja domen ključno vlogo pri feroelektričnem utrjevanju kompleksi defektov $Co_{Fe}^{'} - V_O^{\bullet\bullet}$. Po drugi strani pa imajo pri prevodnosti in pogojih, pod katerimi pride do vzbujanja, ne pa tudi preklapljanja domen, zlasti pri veliki piezoelektrični nelinearnosti in histerezi izmerjeni pri nizkih frekvencah, ključno vlogo $Fe_{Fe}^{\bullet}$. Rezultati torej kažejo, da lahko različni tipi točkastih defektov glede na pogoje vzbujanja (amplituda, frekvenca električnega polja) kontrolirajo makroskopske lastnosti.

Contents

List of Figures

List of Tables

Abbreviations

ABF	... annular bright field
AC	... alternating current
a.u.	... arbitrary units
BEI	... backscattered electron image
BFO	... bismuth ferrite, $BiFeO_3$
BFCO	... Co-doped $BiFeO_3$
BNT	... barium natrium titanate, $(Bi,Na)TiO_3$
BSE	... backscattered electron
BT	... barium titanate, $BaTiO_3$
c-AFM	... conductive atomic force microscopy
DART	... dual AC resonance tracking
DC	... direct current
DFT	... density functional theory
DOS	... density of states
DTA	... differential thermal analysis
DW	... domain wall
EELS	... electron-energy-loss spectroscopy
EPR	... electron paramagnetic resonance
FE-SEM	... field-emission scanning electron microscope
GB	... grain boundary
GS	... grain size
Gs	... ground state
HAADF	... high-angle annular dark field
IPA	... isopropanol
KBT	... potassium bismuth titanate, $(K,Bi)TiO_3$
KNN	... potassium sodium niobate, $(K,Na)NbO_3$
M-W	... Maxwell-Wagner
p	... perovskite
PALS	... positron annihilation lifetime spectroscopy
PAW	... projector-augmented wave
pc	... pseudo-cubic
PE	... polyethylene
PEDOT:PSS	... poly(3,4-ethylenedioxythiohene):polystyrene-sulfate
PFM	... piezo-response force microscopy
PT	... lead titanate, $PbTiO_3$
PZT	... lead zirconate titanate, $Pb(Zr,Ti)O_3$
RT	... room temperature
STEM	... scanning transmission electron microscope
TG	... thermogravimetry
VASP	... Vienna ab-initio simulation package
XANES	... X-ray absorption near-edge structures

XAS ... X-ray absorption spectroscopy
XPS ... X-ray photoelectron spectroscopy
XRD ... X-ray powder diffraction
YSZ ... yttria-stabilized zirconia

Symbols

a	...	lattice constant
A	...	area of the grain
B	...	magnetic field strength
c	...	lattice constant
C	...	charge-carrier concentration
C^T	...	off-resonance free capacity
D_m	...	Feret's diameter mean value
d_{33}	...	piezoelectric coefficient
d_{33}^{init}	...	initial piezoelectric coefficient (extrapolated at zero field)
$d_{33}(E_0)$	...	total (field-dependent) piezoelectric coefficient
E	...	electric field
E_a	...	activation energy
E_c	...	coercive field
E_{cut}	...	energy cutoff
E_{def}^f	...	defect formation energy
E_{defect}^f	...	total energy for the defect cell
E_g	...	electronic bandgap
E_{ib}	...	internal bias field
E_{ref}^f	...	total energy for the reference system (without defect)
E_{rev}	...	reverse electric field
E_0	...	electric field amplitude
f_a	...	antiresonance frequency
f_r	...	resonance frequency
g	...	proportionality factor
h	...	Planck's constant
I	...	electric current
j	...	current density
k_{eff}	...	effective coupling coefficient
k_p	...	planar coupling coefficient
l_{RT}	...	initial dimension of the sample at room temperature
l_T	...	dimension of the sample at the selected temperature
m	...	mass of the sample
M_x	...	magnetic moment on X atom
P	...	polarization
P_D	...	defect polarization
P_i^V	...	probability of finding an O^{2-} vacancy at O^{2-} site i
P_r	...	remanent polarization
P_s	...	spontaneous polarization
q	...	total charge
Q_m	...	electromechanical quality factor

r	...	radius of the sample
S	...	Seebeck coefficient
T_C	...	Ferroelectric Curie temperature
T_N	...	Neel temperature
$tan\,\delta$	...	tangent of the dielectric/piezoelectric phase angle
$tan\,\delta^{init}$	...	tangent of the piezoelectric phase angle extrapolated at zero field
V_0	...	input voltage
Z	...	impedance value at the resonance frequency
ΔE	...	energy difference
ΔE_{seg}	...	segregation enthalpy
Δf_{111}	...	change in non-180° domain texture
Δl	...	change in dimension of the sample (expansion/contraction)
ΔL	...	amplitude of the output displacement
α^*	...	irreversible nonlinear coefficient
δ	...	phase angle between the displacement and voltage signals
$\varepsilon_{intrinsic}$	...	lattice strain
ε'	...	real part of the complex dielectric permittivity
ε''	...	imaginary part of the complex dielectric permittivity
ε''_d	...	imaginary dielectric permittivity related to polarization losses
ε_0	...	dielectric permittivity of vacuum
Θ	...	X-ray diffraction angle
μ_B	...	Bohr magneton
ν	...	operating frequency
ρ_{geo}	...	geometrical density
σ_{DC}	...	specific DC electrical conductivity
σ'	...	real part of the electrical conductivity
σ_1, σ_2	...	conductivity in the two grains measured along the vertical direction
Φ	...	diameter
ω	...	driving field frequency

Chapter 1

Introduction

In the Introduction, the fundamental phenomena and the current status of the topics relevant to this thesis are presented. First, the macroscopic hardening and softening characteristics of ferroelectric materials based on $Pb(Zr,Ti)O_3$ are presented, alongside the formation and type of point defects and defect complexes in these materials. The second part includes an overview of hardening in $BiFeO_3$-based ceramics. Here, the influence of point defects on electrical conductivity and switching behavior is introduced. Finally, the relationship between conductive domain walls and the piezoelectric response is discussed.

1.1 Hardening and Softening Concepts in Ferroelectrics

1.1.1 Hardening and softening from macroscopic perspective

Ferroelectric ceramic materials are widely used in piezoelectric devices, such as sensors, actuators, transducers and memory devices [1]. One of the most important contributions to the application-relevant dielectric and piezoelectric properties of this class of materials is that arising from the displacements of domain walls (DWs), i.e., interfaces separating homogeneous ferroelectric and ferroelastic domain regions inside the ferroelectric material [2]. The reason is that these interfaces can move under an external electric or stress field (as shown schematically in Figure 1.1a,b), even if the fields are well below the coercive field, contributing to the total piezoelectric and dielectric response in addition to the intrinsic (lattice) effect (Figure 1.1c). Depending on the DW mobility, which can in principle be controlled by defect engineering, as will be explained later, this so-called extrinsic contribution related to local DW displacements can represent up to 70 % of the total macroscopic piezoelectric or dielectric response [2].

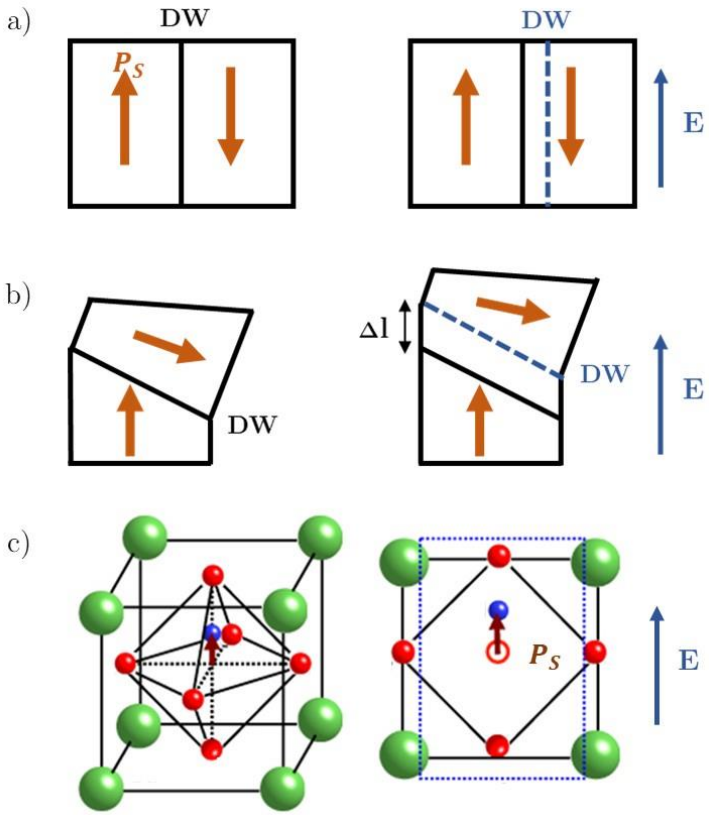

Figure 1.1: Contributions to the total macroscopic piezoelectric response in ferroelectric materials. Schematic presentation of a) ferroelectric (180°) and b) ferroelectric-ferroelastic (non-180°) DW displacements under application of sub-switching electric field. The dashed blue line indicates the position of the DW after displacement and Δl corresponds to changes in dimensions (expansion). c) Intrinsic (lattice) contribution to piezoelectricity; the dotted blue line indicates expansion of the unit cell in the field direction with respect to initial state (full black line) under applied electric field [3]. DW, E and P_s refer to the domain wall, electric field and spontaneous polarization, respectively.

The DW motion is strongly affected by DW interactions with charged point defects. In lead zirconate titanate, $Pb(Zr,Ti)O_3$ (PZT), which is the technologically most important and market-dominating ferroelectric ceramics, these interactions may be tuned by aliovalent doping, resulting in softening and hardening effects, which are the most important concepts for tailoring functional properties of this group of materials for specific applications [4]. Even though the doping level is limited to low values (less than 5 at.%), already a small degree of deviation from the perfect lattice, e.g., on the level of 0.1 at.% of defect concentration, can have a crucial impact on the properties [4], [5]. The most important characteristics of soft and hard PZT are collected in Figure 1.2 and Table 1.1.

Softening can be obtained by donor doping (e.g., La^{3+} replacing Pb^{2+} or Nb^{5+} replacing Zr^{4+}/Ti^{4+}) where donor centers (e.g., $Nb_{Ti}^{\bullet}$)[1] are assumed to be compensated by A-site vacancies ($V_{Pb}^{\prime\prime}$). Donor doping with Nb can be expressed as

[1] In this thesis, the Kröger-Vink notation is used to describe charged point defects [165]. The main body of the notation identifies whether the defect is a vacancy "V", or an ion such as "Nb". The subscript denotes the site that the defect occupies. The superscript identifies the effective charge of the defect relative to the perfect crystal lattice. For this part of notation, dots ($\bullet$) represent positive effective charges, dashes (') represent negative charge and x represent neutral charge.

$$\frac{1}{2}Nb_2O_5 + \frac{1}{2}V_O^{\bullet\bullet} + Ti_{Ti}^x \rightarrow TiO_2 + Nb_{Ti}^{\bullet} + \frac{1}{2}O_O^x \tag{1.1}$$

Relative to undoped PZT, soft PZT ceramics are characterized by an open hysteresis loop (see Figure 1.2a), low coercive field, high dielectric permittivity (Figure 1.2b), high piezoelectric coefficient, high dielectric (Figure 1.2b) and mechanical losses, low mechanical quality factor (Figure 1.2d), low electrical conductivity (Figure 1.2g), easy poling/depoling and absence/weak aging (i.e., change of dielectric, piezoelectric, ferroelectric properties with time). In addition, the properties of soft PZT ceramics exhibit a strong dependence on the electric field, stress and frequency (Figure 1.2c,e,f).

On the other hand, hardening can be achieved by acceptor doping (e.g., K^+ replacing Pb^{2+} or Fe^{3+} replacing Zr^{4+}/Ti^{4+}) and acceptor centers (e.g., Fe'_{Ti}) are assumed to be compensated by oxygen vacancies ($V_O^{\bullet\bullet}$). Acceptor doping with Fe can be expressed as

$$\frac{1}{2}Fe_2O_3 + Ti_{Ti}^x + \frac{1}{2}O_O^x \rightarrow TiO_2 + Fe'_{Ti} + \frac{1}{2}V_O^{\bullet\bullet} \tag{1.2}$$

In exact opposition to soft PZT, hard PZT ceramics are characterized by a pinched hysteresis loop (Figure 1.2a), high coercive field, low dielectric permittivity (Figure 1.2b), low piezoelectric coefficients, low dielectric (Figure 1.2b) and mechanical losses, high mechanical quality factor (Figure 1.2d), moderate electrical conductivity (Figure 1.2g), difficult poling/depoling and significant aging (Figure 1.2h). In addition, the properties of hard PZT ceramics show little dependence on the electric field, stress and frequency (Figure 1.2c,e,f).

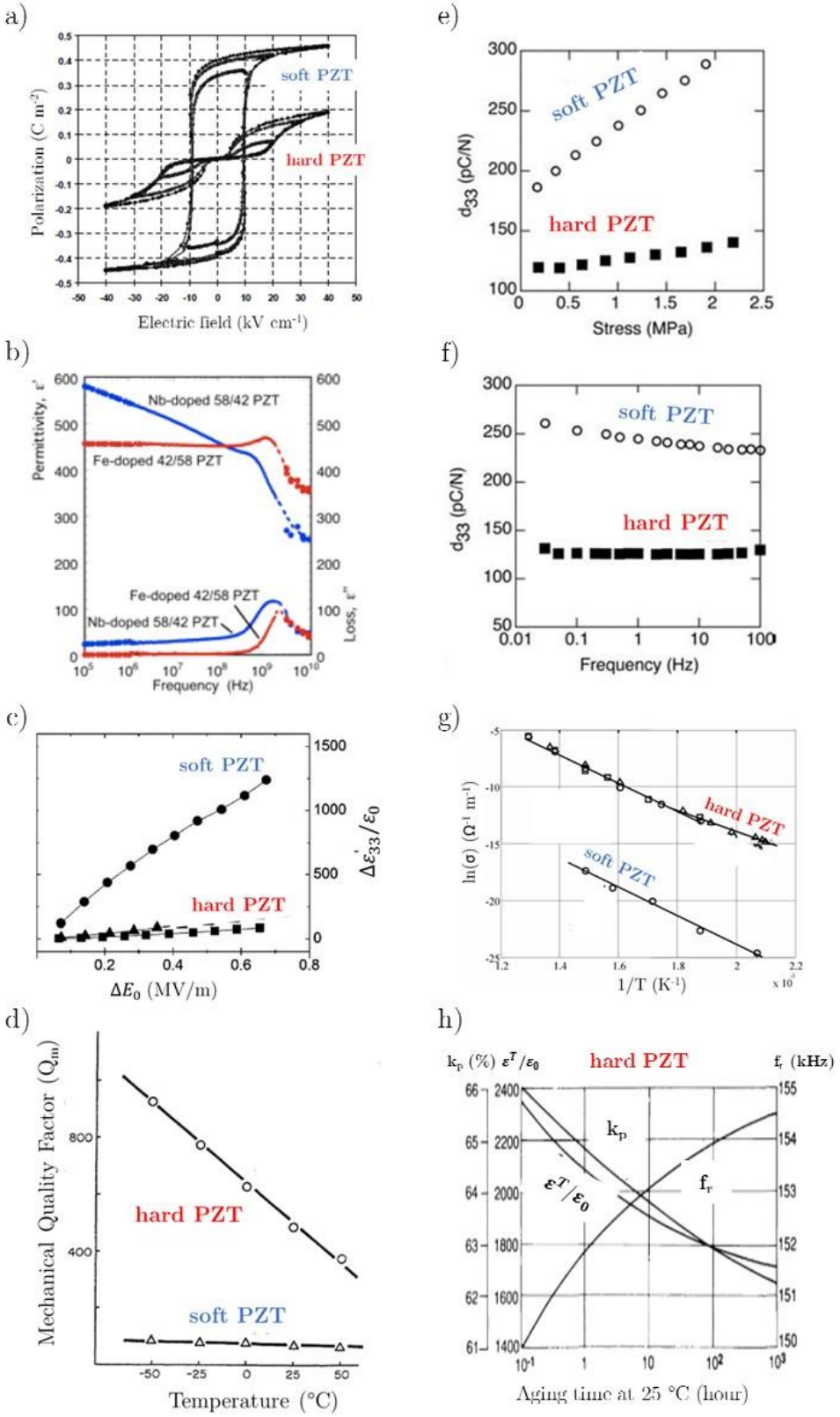

Figure 1.2: Comparison between soft and hard PZT ceramics: a) high-field ferroelectric hysteresis loops [6], b) dielectric permittivity and dielectric loss as a function of frequency [7], c) dielectric permittivity as a function of electric field amplitude [8], d) mechanical quality factor as a function of temperature [9], e) direct d_{33} coefficient as a function of alternating stress field [10], f) direct d_{33} coefficient as a function of frequency [10], e)

Arrhenius plot of bulk conductivity [11] and f) aging of dielectric permittivity, electromechanical coupling coefficient and resonance frequency for hard PZT [12].

Table 1.1: Comparison of soft and hard PZT ceramics: dopants, compensating defects, properties and applications.

	Soft PZT	Hard PZT
Dopants	Donors	Acceptors
	A-site: La^{3+}, Bi^{3+}	A-site: K^{+}, Na^{+}
	B-Site: Nb^{5+}, Ta^{5+}	B-site: Fe^{3+}, Mn^{3+}
Assumed compensation	V''_{Pb}	$V_O^{\bullet\bullet}$
Properties:		
coercive field	low	high
dielectric permittivity	high	low
dielectric losses	high	low
piezoelectric coefficients	high	low
mechanical quality factor	low	high
electromechanical coupling factor	high	low
electrical conductivity	low	high
poling/depoling	easy	difficult
aging	absent/weak	pronounced
Typical applications	actuators	transducers
	sensors	motors
	generators	transformers

It is generally considered that softening properties are associated with highly mobile DWs; however, it is not clear what is causing it. Several possibilities have been suggested, including the following: i) the higher domain-wall mobility results from donor dopants compensating the effects of acceptor cations that are naturally present in undoped materials (e.g., V''_{Pb} due to volatilization of Pb during high temperature treatment) [4], ii) V''_{Pb} that compensate donor dopants, e.g., $Nb^{\bullet}_{Ti}$, help to reduce internal stresses in ceramics and make domain walls more mobile [4], [13], and iii) softening is related to electron transfer between defects, which minimize space charges at DWs [11]. Nevertheless, density functional theory (DFT) calculations showed there is no binding energy between oppositely charged defects in soft materials (i.e., the donor site and A-site vacancy) and no preferential alignment with respect to P_s (Figure 1.3). Therefore, the defect complexes are unlikely to exist in soft materials, and even if they do exist, their interaction with P_s is weak. Furthermore, the absence of defect complexes in soft materials has also been supported with electron paramagnetic resonance (EPR) measurements [14].

On the other hand, hardening results from a reduced DW movement, i.e., stabilized domain structure, as a consequence of the interaction with defect complexes (Figure 1.3), which act as strong pinning centers [15]. Details of hardening mechanisms are explained in the next chapters. It is clear that point defects play a key role in both the softening and hardening mechanisms as a result of either weak or strong interactions with DWs, respectively.

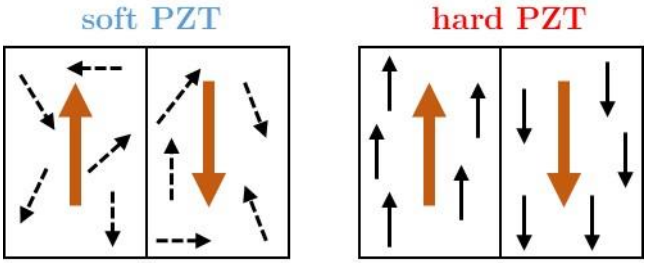

Figure 1.3: Schematic representation of possible defect states in soft and hard PZT, based on theoretical (DFT) [16] and experimental (EPR) data [14]. Small black arrows denote defect dipoles, which are in the case of soft PZT denoted by dashed arrows as they most probably do not exist. Large orange arrows denote P_s within domains.

1.1.2 Hardening and aging mechanisms

Ferroelectric hardening reveals itself through deformation of the polarization loop, which can be observed as a shift of the loop along the axis of the electric field in the poled state (so-called bias or imprint; Figure 1.4a,c) or pinching of the loop in the unpoled state (Figure 1.4b,c) [17]. The loop deformation is in both cases associated with a strong pinning interaction of the charged point defects with DWs (Figure 1.3, right schematic). The domain configuration is stabilized by defects, whereas an internal bias field (E_{int}) is generated, which hinders polarization switching under the application of an electric field more extensively in one field direction than the opposite. The internal bias field can be calculated as [18]

$$E_{int} = \frac{E_c^+ + E_c^-}{2} \tag{1.3}$$

where E_c^+ and E_c^- correspond to the positive and negative coercive fields, respectively (i.e., measured in the positive and negative field cycle; see Figure 1.4a).

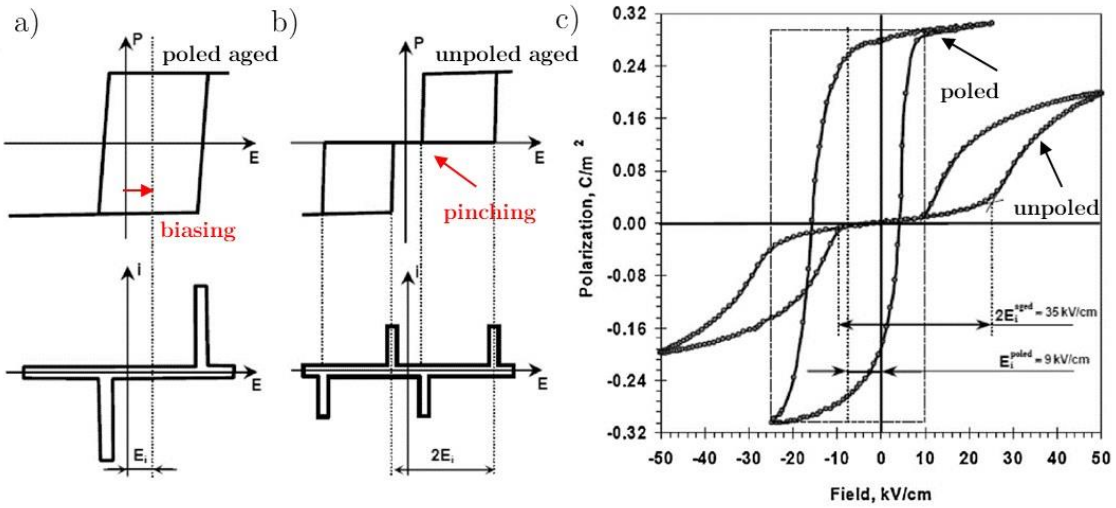

Figure 1.4: Schematic representation of polarization-electric field (P-E) and current-electric field (I-E) hysteresis loops of a) poled aged and b) unpoled aged ceramics [17]; c) measured hysteresis loops of 1 at.% Fe-doped PZT ceramics in unpoled (aged) and poled (aged) states [6]. The red arrows in a) and b) denote biasing and pinching, respectively.

Several studies have shown that the stabilization of the domain structure and thus the hardening, is closely related to aging [17], [19]. Unlike aging, as described in the previous section, which refers to the degradation of properties with time (see Figure 1.2h), in this case, aging is considered as the electrostatic rearrangement (migration) of mobile charged defects, usually into complexes (meaning binding of the oppositely charged defects), which align in the direction of P_s in order to conform the electrostatic and elastic configuration set by the P_s orientation (Figure 1.5). The three most commonly discussed aging/hardening mechanisms in the literature are [17]:

1) The volume (bulk) effect involves the alignment of charged defects along the polarization within ferroelectric domains (in the bulk of the material, hence "volume" effect).
2) The domain-wall effect is characterized by the diffusion of charged defects into the domain walls resulting in pinning of their positions.
3) The grain-boundary effect involves the diffusion of defects to grain boundaries or interfaces between different phases (electrodes, secondary phases), which form space-charge layers that stabilize the domain configuration.

Common to all these mechanisms is that mobile charged defects, regardless of their location, act, more or less, as strong pinning centers for the domain-wall movements and switching, resulting in a pinched/biased polarization loop, as explained earlier (Figure 1.4). Aging can be caused by one or more mechanisms described above; however, it has been theoretically suggested and experimentally confirmed that the prevailing mechanism in acceptor-doped PZT/$PbTiO_3$ (PT)/$BaTiO_3$ (BT) is most likely the volume (bulk) effect [20]–[22].

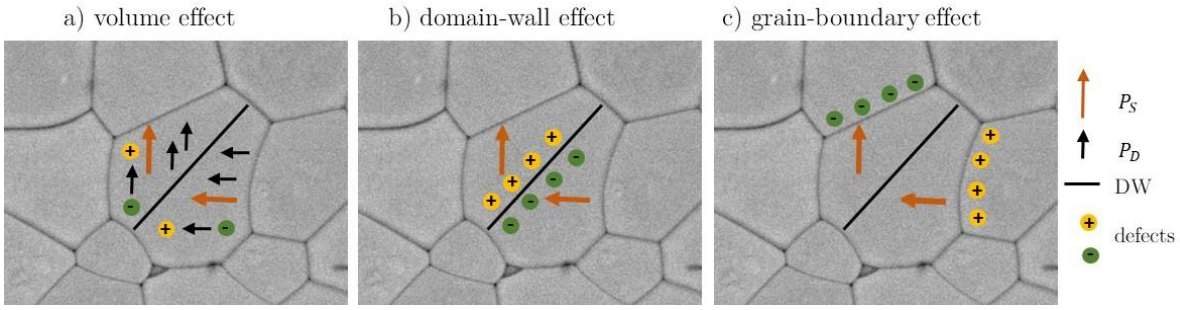

Figure 1.5: Three most commonly discussed aging mechanisms: a) volume (bulk) effect, b) domain-wall effect and c) grain-boundary (interface) effect. Orange and black arrows denote the direction of spontaneous (P_s) and defect (P_D) polarization, respectively, and the solid black line represents the DW. The yellow and green circles denote positively and negatively charged point defects, respectively. The schematic representations correspond to the aging mechanisms proposed by Carl and Hardtl and are only illustrative (exact details of which charges and how they distribute in different regions is in most cases unknown) [17].

1.1.3 Formation and location of defect complexes

The most commonly accepted explanation of aging is that the material starts to age in the process of sintering, immediately after cooling through the Curie temperature (T_C), where the sample undergoes the paraelectric-to-ferroelectric phase transition.

Following earlier studies [17], [20], [22], Zhang and Ren [19] proposed a simplified picture of the volume-effect aging mechanism through the defect-symmetry principle (called the "symmetry-conforming mechanism" in (acceptor) Mn^{3+}-doped $BaTiO_3$ single crystals, using the same early concept of the alignment of defects in the P_s direction. In

this view, above T_C the material is in a paraelectric phase with cubic symmetry (Figure 1.6a). Under these conditions, the acceptor compensating defects, i.e., $V_O^{\bullet\bullet}$, are randomly distributed, which means that the probability of finding $V_O^{\bullet\bullet}$ at any of the six sites (i=1-6) within oxygen octahedra next to Mn^{3+} ion is equal. Upon cooling below T_C, the crystal symmetry changes to tetragonal; however, the point defects cannot migrate so fast, which results in cubic defect symmetry inside the tetragonal symmetry (Figure 1.6b). However, such a configuration is electrostatically and elastically unstable since the positions for $V_O^{\bullet\bullet}$ are not equivalent with respect to the Mn^{3+} ion in a tetragonal structure. Sites closer to Mn^{3+} have a larger defect probability, thus the defect probability is changed to $P_1^V > P_2^V = P_3^V = P_4^V = P_5^V > P_6^V$ (Figure 1.6c). This is because, electrostatically, the negatively charged $V_O^{\bullet\bullet}$ tend to stay closer to the positively charged acceptor sites (due to Coulomb attraction forces). In addition, equal P_s and P_D directions lower the overall elastic energy associated with matching of the spontaneous and defect-related strains. The process of the reorientation of the defect to conform the P_s symmetry requires short-range migration (hopping), i.e., redistribution of the oxygen vacancies in the preferred orientation and consequently also time. In the fully aged sample, the defect symmetry is tetragonal and the defect polarization (P_D) is aligned in the same direction as P_s (Figure 1.6c).

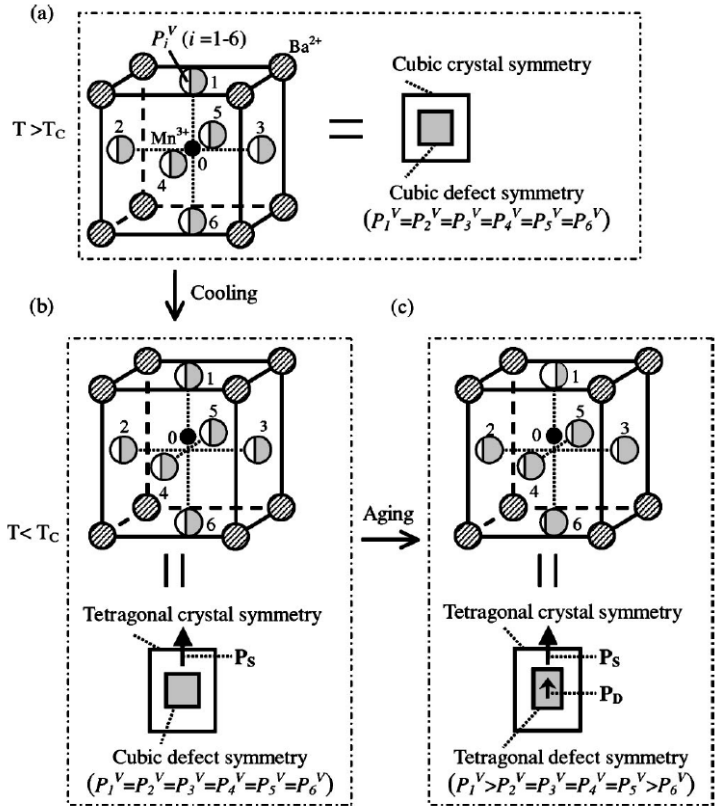

Figure 1.6: Aging in Mn^{3+}-doped $BaTiO_3$ perovskite [19]. a) Above T_C the material exhibits a cubic crystal and defect symmetry. b) Upon cooling below T_C the material undergoes a transition from the cubic to the tetragonal crystal symmetry; however, the point defects cannot migrate so fast and thus the defect symmetry remains cubic. c) After aging (i.e., redistribution of defects) both the crystal and defect symmetry are tetragonal (hence the name "symmetry confirming mechanism"). P_i^V refers to the probability of finding an O^{2-} vacancy at an O^{2-} site i, P_s refers to spontaneous polarization and P_D refers to defect polarization.

The formation of defect complexes was investigated using DFT calculations. Several studies on Fe-doped $PbTiO_3$ showed that the acceptor sites tend to bind with $V_O^{\bullet\bullet}$, forming defect complexes. [16], [23], [24] Furthermore, it was suggested that these defect complexes align in the direction of P_s and act as strong pinning centers for the domain wall movement. For example, Chandrasekaran *et al.* [16] performed a DFT study on Fe-doped PT where the energy was calculated for defect complexes in different orientations with respect to P_s. It was found that the lowest energy configuration (most stable), i.e., the ground state (Gs), is when $Fe'_{Ti} - V_O^{\bullet\bullet}$ are oriented in the direction of P_s (Figure 1.7a). The energy of antiparallel alignment (Figure 1.7c) was found to be 0.38 eV higher than the ground state. Interestingly, it was shown that the highest energy, i.e., 0.52 eV higher than the ground state, is in the case of the perpendicular alignment of defect complexes with respect to P_s (Figure 1.7b). These results are not consistent with the study presented in ref. [19] (see Figure 1.6), where only electrostatic effects were considered. The high energy of the perpendicular alignment (Figure 1.7b) thus implies that the elastic effects play a very important role in the energetics of the defect complex alignment.

In contrast to the findings on Fe-doped PT (hard ferroelectric), the calculation of energy differences between different defect configurations in Nb-doped PT (soft ferroelectric) showed that the ground-state configuration (direction of P_s) is only 0.06 eV lower in energy than the perpendicular or antiparallel configuration, indicating that there is no preferential defect alignment with the P_s. In addition, it has been shown that $Nb_{Ti}^{\bullet} - V_{Pb}''$ do not have a tendency for binding, since their binding energy is only 0.04 eV [16].

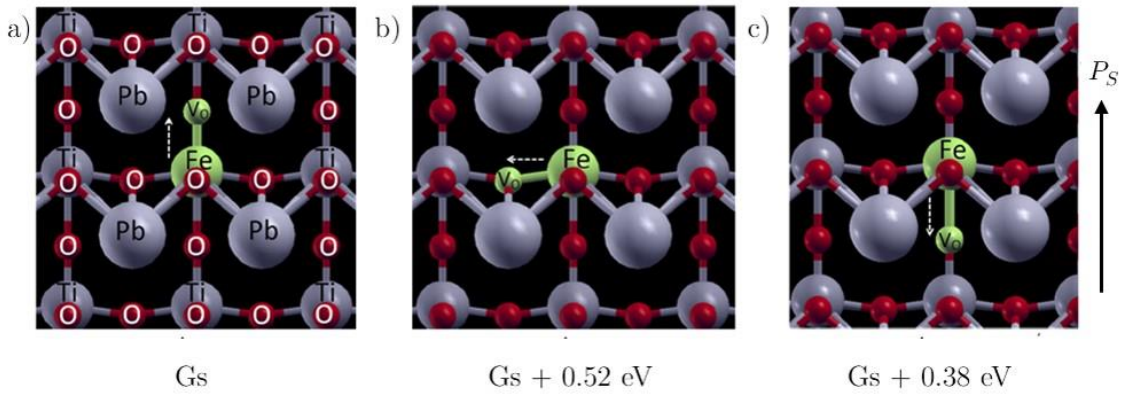

Figure 1.7: Energy differences of defect complexes in Fe-doped $PbTiO_3$ depending on the orientation to P_s a) parallel to P_s (Gs stands for the ground state – configuration with the lowest energy), b) perpendicular to P_s (the energy is 0.52 eV higher than Gs) and c) antiparallel to P_s (the energy is 0.38 eV higher than Gs). The black arrow indicates the direction of P_s, while the white dashed arrow indicates the direction of defect polarization P_D [16].

The DFT study on Fe-doped PT [16] investigated the stability of $Fe'_{Ti} - V_O^{\bullet\bullet}$ defect complexes at different locations, i.e., at the DW interface or within the domain (in the interior), and for different orientations with respect to P_s, i.e., parallel or antiparallel to P_s. In total, four different configurations were studied, as shown in Figure 1.8a (bottom panel). It was found that the lowest energy is obtained when the defect complex is located at the DW with P_D aligned parallel to P_s (position 0 in Figure 1.8a). However, when the defect complex is located at DW with P_D opposing P_s, the position in the interior with polarization parallel to P_s becomes more favorable (compare positions -1 and 1 in Figure 1.8a, upper graph). These results suggest that, regardless of the defect complex location, the orientation in the direction parallel to P_s is energetically favorable and also that the

pinning effects are apparently a combination of bulk and domain-wall effects (as shown in Figure 1.5a,b) [16].

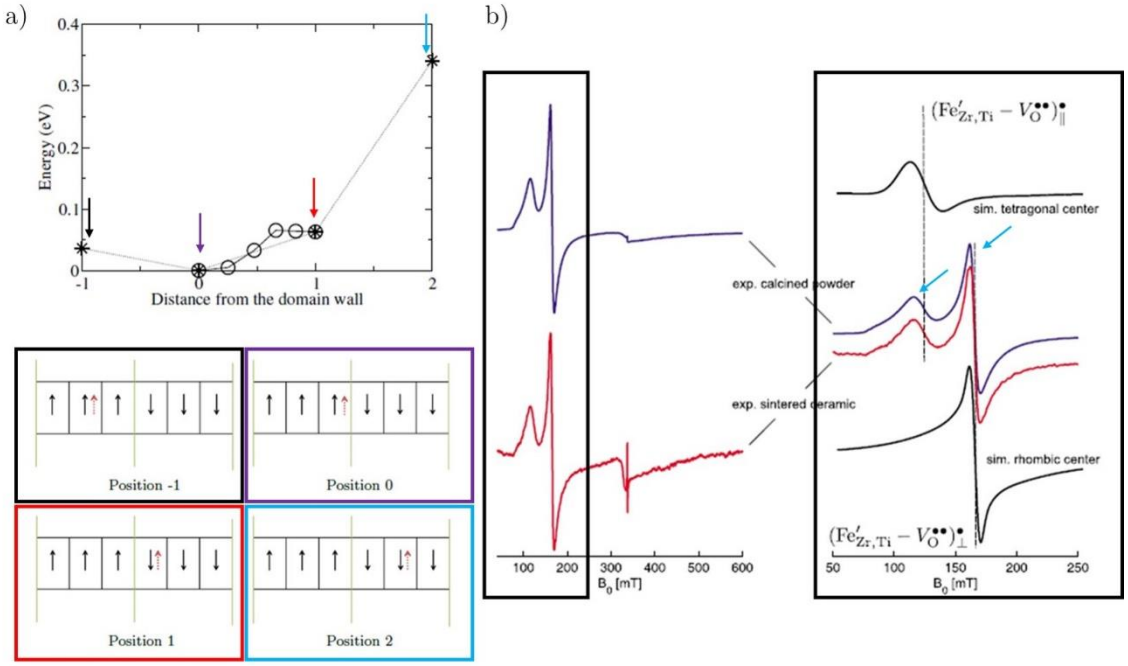

Figure 1.8: Location of defect complexes with respect to DWs. a) DFT study on Fe-doped PT: Energy profile of the supercell for different positions of $(\mathrm{Fe}'_{\mathrm{Ti}} - \mathrm{V}_{\mathrm{O}}^{\bullet\bullet})^{\bullet}$ relative to the domain wall. The labels -1, 0, 1 and 2 are explained in the bottom panel, where the defect complex position and orientation are represented by the small dashed-red arrow and P_s is represented with the black arrow [16]. b) EPR spectra of Fe-doped PZT: Spectra for calcined powder (top) and sintered ceramic (bottom) are enlarged in the right panel and compared to the numerical simulations for the axial (top) and rhombic (bottom) $(\mathrm{Fe}'_{\mathrm{Ti}} - \mathrm{V}_{\mathrm{O}}^{\bullet\bullet})^{\bullet}$ site symmetries (black spectra) [25]. Blue arrows in the right panel denote two main resonances, i.e., at 110 mT (center of axial site symmetry) and 160 mT (center of rhombic site symmetry).

Chandrasekaran *et al.* [16] also found (still theoretically) that in the case of isolated $V_O^{\bullet\bullet}$, the stability of the defect when located at the DW is always higher than when located in the domain interior. Similar observations were reported by He and Vanderbilt [26], who also showed that even when the $V_O^{\bullet\bullet}$ is placed away from the DW, during the relaxation of the model the DW will be spontaneously shifted toward the vacancy position. These theoretical results clearly suggest that $V_O^{\bullet\bullet}$ are strongly attracted to the DWs, particularly when isolated from the acceptors.

In order to investigate whether the defect complexes are located within domains or DWs, EPR analysis in Fe-doped PZT has been adopted [25]. The X-band EPR spectra of Fe-doped PZT are shown in Figure 1.8b. The two main resonances at low fields, i.e., at 110 mT (center of axial site symmetry) and 160 mT (center of rhombic site symmetry) (denoted with blue arrows in right panel of Figure 1.8b), are characteristic for the formation of $(Fe'_{Ti} - V_O^{\bullet\bullet})^{\bullet}$ defect complexes. Two different samples were analyzed: i) a calcined powder, where a considerably reduced amount of non-180° DWs is expected due to mechanical stress release and ii) sintered dense ceramics, where markedly developed domain structure is expected due to higher internal (intergranular) stresses. It can be observed that

both the ceramic and powder spectra show an identical intensity ratio of the resonances from the axial and rhombic centers. These results suggest that the concentration of defect complexes at DWs (if there are any) is below the EPR detection limit, which means that their concentration at DWs should be at least nine orders of magnitude smaller than within the domains. The authors assumed that the defect complexes are most probably not located close to the DWs, but mostly inside the domains. However, it is not clear whether defects are preferentially distributed close to the grain boundaries or uniformly through the grains, which leaves open the question about grain-boundary (GB) effect. In addition, the theoretical model by Genenko *et al.* [27] showed that when the defects are placed near grain boundaries, the clamping pressure on the DWs should be two orders of magnitude stronger than when the defects are placed between the DWs, i.e., in the domain interior.

On the other hand, an *in-situ* optical microscopy study on Mn^{3+}-doped $BaTiO_3$ single crystals [19] showed that upon electric field cycling, the initial multi-domain state changes to a single-domain state; however, after removing the electric field, the initial multi-domain state was restored. Considering that single crystals exhibit no grain boundaries and that in a single-state domain there would be no domain walls to be dragged back, aging was explained solely by the volume effect.

Taking into account the overall results and literature on hardening in "classic" ferroelectrics (PZT, BT, PT), one might conclude that although the volume effect is in general considered as the prevailing mechanism, the exact location of defect complexes is still disputable, and it is thus not clear whether and how other mechanisms (DW, GB effects) contribute to the overall hardening and aging mechanisms in different ferroelectric materials.

1.1.4 Identification of defects complexes

Hardening features have been observed in several lead-based as well as lead-free perovskite materials. In all these cases, acceptor dopant—$V_O^{\bullet\bullet}$ or A-site vacancy—$V_O^{\bullet\bullet}$ defect complexes have been considered to lie at the origin of the hardening [28], [29]. Much research has been conducted in order to identify the defect complexes and, in particular, EPR has proven to be an extremely powerful tool for investigating point defects. In this chapter, the results of EPR analyses and the identification of defect states in different materials are presented, showing the complexity of defect associations.

In $PbTiO_3$, which is commonly used as the model system for the more complex PZT, defect complexes, such as $(Fe'_{Zr/Ti} - V_O^{\bullet\bullet})^{\bullet}$ and $(Cu''_{Zr/Ti} - V_O^{\bullet\bullet})^{x}$ have been identified, aligned parallel to the polarization direction in the aged state [30]–[34]. The $(Fe'_{Zr/Ti} - V_O^{\bullet\bullet})^{\bullet}$ defect dipoles are electrically overcompensated and it is naturally assumed that some "free" Fe'_{Ti} would be expected. However, in a study by Mestric *et al.* [31], no EPR signals that could be attributed to the "free" Fe'_{Ti} defect states were identified, therefore, an alternative charge compensation with V''_{Pb} has been suggested [31]. This hypothesis is supported by the loss of PbO during processing, resulting in the formation of a $V''_{Pb} - V_O^{\bullet\bullet}$ divacancy pair; however, no characteristic feature associated with a cation vacancy (V''''_{Pb}) could be observed in the EPR spectra. On the other hand, in the study by Keeble *et al.* [32] some isolated Fe'_{Ti} defects with low concentration were found. The compensating mechanism of the overcompensated $(Fe'_{Zr/Ti} - V_O^{\bullet\bullet})^{\bullet}$ in Fe-doped PT and PZT is thus not completely clear.

In lead-free Mn-doped $BaTiO_3$ crystals, Zhang et al. [35] reported on a $(Mn''_{Ti} - V_O^{\bullet\bullet})^{x}$ defect aligned in the direction of P_s. On the other hand, in another study on Mn-doped $BaTiO_3$, two types of defects have been observed, i.e., $(Mn''_{Ti} - V_O^{\bullet\bullet})^{x}$ and Mn''_{Ti}, where the

former were suggested to represent the minority defects [36]. In this same study it was hypothesized that some other defects compensating Mn''_{Ti} are present, which cannot be detected by EPR.

In Fe-doped $(Bi_{0.5}Na_{0.5})TiO_3$ (BNT) ceramics, $(Fe'_{Zr/Ti} - V_O^{\bullet\bullet})^{\bullet}$ defect complexes were found, similar as in Fe-doped PT [37]. In contrast, the study of CuO-doped (K,Na)NbO_3 (KNN) revealed some peculiarities in the defect structure of this system if compared to others, e.g., PZT or BT, most probably due to the greater effective charge when replacing Cu^{2+} with Nb^{5+} (e.g. Cu'''_{Nb} in KNN vs. Mn''_{Ti} in BT)[38]. Two types of defect complexes have been identified in this case, i.e., dimeric $(Cu'''_{Nb} - V_O^{\bullet\bullet})'$ and trimeric $(V_O^{\bullet\bullet} - Cu'''_{Nb} - V_O^{\bullet\bullet})^{\bullet}$ complexes. Their concentrations were found to be comparable, indicating that these defects probably mutually compensate each other.

Point defects were also investigated by positron annihilation lifetime spectroscopy (PALS) due to its particular sensitivity to cation vacancy[2] defects in perovskites. In Fe-doped PZT, V''_{Pb} and $V''''_{Zr/Ti}$ as well as cation-oxygen divacancy, i.e., $V''_{Pb} - V_O^{\bullet\bullet}$ and $V''''_{Zr/Ti} - V_O^{\bullet\bullet}$, defect pairs were identified [39]. In addition, it has been found that by increasing the Fe concentration (and thus $[V_O^{\bullet\bullet}]$), the ratio $[V''''_{Zr/Ti}]/[V''_{Pb}]$ increases, indicating charge compensation with the formation of $V''''_{Zr/Ti}$. This view is not consistent with the compensating mechanism proposed in ref. [31] or [32], where the formation of V''_{Pb} or some "free" Fe'_{Ti} is assumed. On the other hand, the PALS analysis in (unintentionally) Fe-doped $PbTiO_3$ indicates that $(Fe'_{Ti} - V_O^{\bullet\bullet})^{\bullet}$ are compensated by V''_{Pb} as their concentration increased with an increased concentration of Fe^{3+} [39]. These examples clearly illustrate the complexity of the defect-compensation mechanisms in PZT.

A short summary of defects identified with PALS and EPR in Pb-based and Pb-free ferroelectrics is given in Table 1.2.

Table 1.2: Identified defects in some lead-based and lead-free ferroelectric perovskites investigated by positron annihilation lifetime spectroscopy (PALS) and electron paramagnetic resonance (EPR).

Method	Material [reference]	Identified defects
PALS	Fe-doped PZT ceramics [39]	V''_{Pb}, $V''''_{Zr/Ti}$, $V''_{Pb} - V_O^{\bullet\bullet}$, $V''''_{Zr/Ti} - V_O^{\bullet\bullet}$
	(unintentionally) Fe-doped $PbTiO_3$ crystals [39]	V''_{Pb}
EPR	Fe-doped $PbTiO_3$ ceramics [30]–[32]	$(Fe'_{Zr/Ti} - V_O^{\bullet\bullet})^{\bullet}$
	Mn-doped $BaTiO_3$ crystals [35]	$(Mn''_{Ti} - V_O^{\bullet\bullet})^{x}$
	Mn-doped $BaTiO_3$ crystals [36]	$(Mn''_{Ti} - V_O^{\bullet\bullet})^{x}$, Mn''_{Ti}
	Fe-doped $(Bi_{0.5}Na_{0.5})TiO_3$ ceramics [37]	$(Fe'_{Zr/Ti} - V_O^{\bullet\bullet})^{\bullet}$
	CuO doped (K,Na)NbO_3 ceramics [38]	$(Cu'''_{Nb} - V_O^{\bullet\bullet})'$ and $(V_O^{\bullet\bullet} - Cu'''_{Nb} - V_O^{\bullet\bullet})^{\bullet}$

In all the above-mentioned studies, $V_O^{\bullet\bullet}$ are considered as the only mobile defects at room temperature. This is because there are available neighboring sites within the oxygen

[2] Positrons will not be bound at anion vacancies due to their positive charge, or, will bind very weakly. On the other hand, the binding at cation vacancies is much stronger. Therefore, the trapping of positrons will mainly be observed at negative cation vacancies, or complexes of cation and anion vacancies, although clusters of anions may also provide traps for positrons [166].

octahedra between which the $V_O^{\bullet\bullet}$ may easily exchange its position by hopping (for easier visualization see schematic representation of perovskite structure in Figure 1.6). Therefore, it is often assumed that the presence and mobility of $V_O^{\bullet\bullet}$ are crucial for the hardening (aging). However, in the study by Slouka *et al.* [40], where the PZT ceramics were investigated using tracer diffusion and electrochemical impedance spectroscopy, it has been suggested that the concentration of $V_O^{\bullet\bullet}$ in Fe-doped PZT is at the ppm level, which is much lower than required for the complete compensation of the acceptor dopant. Furthermore, Fe-doped PZT showed a distinct increase in resistance upon switching the atmosphere from air to nitrogen, which is an indication of electron-hole conduction. Finally, it has been suggested that trapped holes, in particular Pb^{4+} ions, are potential majority charge carriers that compensate acceptors and interact with DWs, similarly as $V_O^{\bullet\bullet}$-related defect complexes. However, no further study and explanation about the influence of Pb^{4+} ions on hardening in PZT has been provided, or at least extensively studied. In order to investigate the interaction of Pb^{4+} with DWs, one could for example measure the hysteresis loops of acceptor-doped and undoped PZT with excess of Pb^{2+} as it has been shown that this results in the promoted formation of Pb^{4+} [41], [42].

1.1.5 Hardening-softening transitions

Literature reports that hysteresis loops in hard ferroelectrics can be de-pinched (opened/relaxed) in two different ways. One way is by heating the sample over the T_C and then cooling rapidly (quenching) to room temperature, resulting in a disordered configuration (random distribution) of defects (similarly as shown in Figure 1.3 for soft PZT) [10]. The degree of hysteresis relaxation depends on the cooling rate and thus the thermal conductivity of the quenching media, typically a liquid, to which the heat of the sample is transferred, when dropped into the media (Figure 1.9a). However, the disordered configuration of defects is not stable and after some time the loop becomes pinched again [6].

In contrast to hard ferroelectrics, the quenching of soft ferroelectrics has no effect on the shape of the hysteresis loop (Figure 1.9), indicating that defects are already randomly distributed (Figure 1.3, soft PZT). This is in agreement with the DFT study on Nb-doped PT mentioned before, which shows no preferential alignment or even creation of defect complexes. The absence of aging or weak aging in soft ferroelectrics could thus be related to i) a lower concentration of $V_O^{\bullet\bullet}$ (and thus the absence of strong pinning centers) with respect to hard ferroelectrics, due to the effects of donor compensation, ii) absence of mobile point defects (e.g., neither donor centers nor V_{Pb}'' are mobile from room temperature up to T_C) or iii) no tendency of defects to bind together, which thus remain randomly distributed.

The second option for relaxing the hysteresis loop is to apply a continuous AC electric field cycling. The degree of the hysteresis relaxation was shown to depend on frequency, amplitude, temperature and total number of cycles [6]. The influence of the latter is, for illustration, presented in Figure 1.9b. Hysteresis relaxation upon the application of an AC electric field is supposed to be due to the reorientation of defect complexes and consequently the reduced clamping of domain walls. The redistribution of defect complexes under an applied electric field has also been supported by DFT calculations [23] and EPR spectroscopy [43].

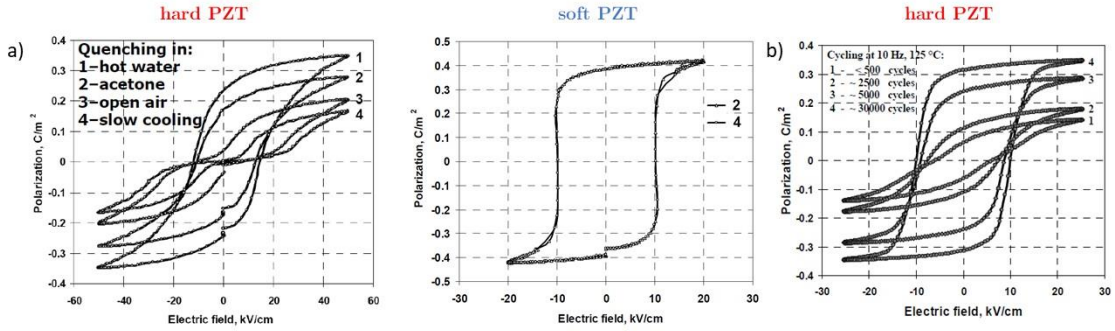

Figure 1.9: Hysteresis relaxation, i.e., de-aging [6]. a) The effect of quenching in hard (1 at.% Fe doped; left) and soft (1 at.% Nb doped; right) PZT (58/42) ceramics in different media: hot water (1), acetone (2), air (3) and after slow cooling in the furnace (4). b) The effect of electric field cycling at 10 Hz and 25 kV cm^{-1} in 1 at.% Fe-doped PZT (58/42) ceramics.

A thorough study of the interrelations between de-aging by field cycling and oxygen vacancy hopping was performed on 0.1–1 at.% Fe-doped PZT (58/42) ceramics [44]. It has been shown that the activation energy (E_a) for de-aging by electric field cycling (0.55–0.7 eV) is similar to E_a for charge-hopping conduction (0.6–0.8 eV), implying that the hysteresis relaxation is associated with the short-range migration of oxygen vacancies, i.e., reorientation of defect complexes. The E_a of DC conductivity was found to be higher (~0.9-1.2 eV) and it was thus claimed that the migration of charge carriers over longer distances contributes to de-aging under large field and higher temperature, resulting in a rectangular shape of the loop (see, for example, the *P-E* loop number 4 in Figure 1.9b). However, it should be pointed out that similar E_a (1.1-1.4 eV) has been in several studies attributed to p-type conductivity and trapped holes [40], [45].

1.2 Literature Review of Charged Defects, Electrical Conductivity and Hardening in BFO-Based Ceramics

1.2.1 Defect chemistry and electrical conductivity

Defect chemistry is highly relevant, in particular for the performance of BFO-based piezoelectric ceramics. In fact, this is a material family showing commonly high levels of electrical conductivity, one of the most important shortcomings for practical piezoelectric applications, especially for high-temperature operation [46]–[48].

A recently proposed thermodynamic point-defect model for BFO-based materials [49] assumes two defect reactions related to: i) volatilization of Bi_2O_3 at elevated temperatures (eq. (1.4)), resulting in the formation of V_{Bi}''' and $V_O^{\bullet\bullet}$ [50], [51], and ii) reduction/oxidation of Fe^{3+} (eq. (1.5) and (1.6), respectively), which is determined by the partial pressure of O_2 during annealing/cooling and leads to either the formation of reduced Fe^{2+} (Fe'_{Fe}), resulting in n-type conductivity, or oxidized Fe^{4+} ($Fe^{\bullet}_{Fe}$) states, resulting in p-type conductivity. The origin of n- and p-type conductivity can therefore be rationalized through either electron hopping between the Fe^{2+} (Fe'_{Fe}) and Fe^{3+} (Fe^{x}_{Fe}) sites or hole hopping between the Fe^{4+} ($Fe^{\bullet}_{Fe}$) and Fe^{3+} (Fe^{x}_{Fe}) sites, respectively [52].

$$2Bi_{Bi}^{x} + 3O_{O}^{x} \leftrightarrow 2V_{Bi}^{'''} + 3V_{O}^{\bullet\bullet} + 2Bi(g) + \frac{3}{2}O_2(g) \quad (1.4)$$

$$2Fe_{Fe}^{x} + O_{O}^{x} \leftrightarrow 2Fe_{Fe}^{'} + V_{O}^{\bullet\bullet} + \frac{1}{2}O_2(g) \quad (1.5)$$

$$2Fe_{Fe}^{x} + V_{O}^{\bullet\bullet} + \frac{1}{2}O_2(g) \leftrightarrow 2Fe_{Fe}^{\bullet} + O_{O}^{x} \quad (1.6)$$

The oxygen partial pressure at which the transition from p- to n–type occurs upon decreasing $p(O_2)$ depends on the temperature and composition. For example, in 0.9BFO-0.1($K_{0.5}Bi_{0.5}$)TiO_3 (KBT) ceramics a minimum in electrical conductivity (p- to n-type transition or vice versa) was found at $p(O_2)$ ~10^{-2} atm in the temperature range 700-800 °C (Figure 1.10a) [49]. On the other hand, unmodified BFO and 5 at.% Sr-doped BFO displayed p-type conductivity within the $p(O_2)$ range from 0.21 to 10^{-6} atm at comparable temperatures (Figure 1.10b) [53]. The reason for observing the p- to n-type transition in BFO-KBT already at $p(O_2)$ ~ 10^{-2} atm could be explained by considering KBT as an n-type semiconductor, resulting in the suppression of p-type conductivity in BFO [54]. However, it should be pointed out that in all three cases presented in Figure 1.10, the conductivity is of p-type in $p(O_2)$ rich conditions (e.g., air – 0.21 atm), indicating that BFO-based systems (rich in BFO; either doped or solid solutions), in principle exhibit qualitatively similar or comparable behavior as it will be shown later.

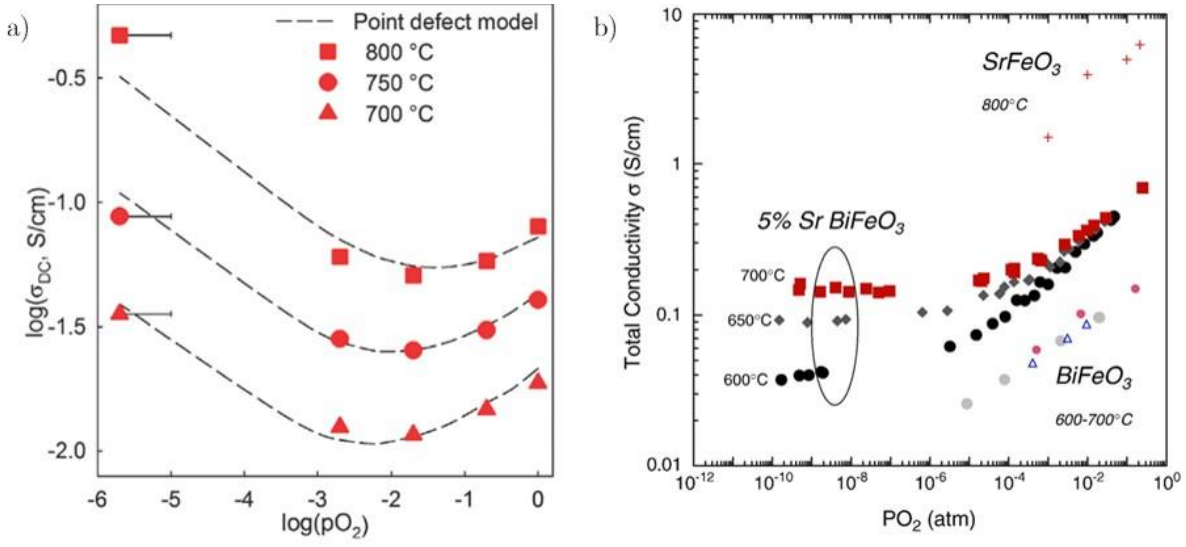

Figure 1.10: Electrical conductivity as a function of $p(O_2)$ in BFO-based materials. a) Transition from n- to p-type conduction regime on increasing $p(O_2)$ at 700, 750 and 800 °C for 0.9BFO-0.1KBT ceramics [49]. b) Unmodified BFO and 5 at.% Sr doped BFO showing p-type conductivity within $p(O_2)$ range from 0.21 to 10^{-6} atm in the temperature range 600-700 °C [53].

A number of studies suggest that the origin of the high conductivity in BFO-based materials is associated with oxygen vacancies and/or Fe^{2+}, rather than Fe^{4+} [55]–[62].

However, when seeking for evidence of their existence, the majority of the literature is relying on X-ray photoelectron spectroscopy (XPS) [59]–[61]. Note, however, that even though the X-rays in XPS can penetrate a few micrometers into the sample, only the photoelectrons generated relatively close to the surface have enough energy to escape and be detected, which means that this method provides information exclusively from the surface [63]. In addition, there are several studies demonstrating that the electrical conductivity of BFO-based materials decreases by thermal treatment in an oxygen-poor atmosphere (e.g., in N_2 [49], [53], [64]–[67]), which is exactly the opposite as would be expected in the case that the Fe^{2+} would be the charge carriers responsible for the conductivity.

A study by Morozov *et al.* [64] on 0.7BFO-0.3KBT ceramics showed that upon annealing the samples in N_2 up to 700 °C, the drop of conductivity occurs within the temperature range 400-500 °C and retains upon cooling down to RT (Figure 1.11a, blue curve 1). Upon heating the samples in O_2, the conductivity returns back to the initial value (Figure 1.11a, red curve 2), demonstrating the complete redox reversibility. In addition, the onset of oxidation at ~270 °C, as seen by the irregular change in the conductivity (see vertical dotted red line in Figure 1.11a), suggests a significant oxygen mobility already at such low temperatures. The inset in Figure 1.11a further demonstrates that the conductivity at RT in 0.7BFO-0.3KBT is highly sensitive to the annealing atmosphere as it has been decreased by almost 4 orders of magnitude after annealing in N_2 with respect to O_2/synthetic air (here, the plateau of the AC conductivity at low frequencies is related to the DC conductivity component; for details see chapter 4.2.1.2). The negligible difference between the conductivity after annealing in O_2 and synthetic air could be explained with the small difference in $p(O_2)$, i.e., 1 vs 0.21 atm, respectively.

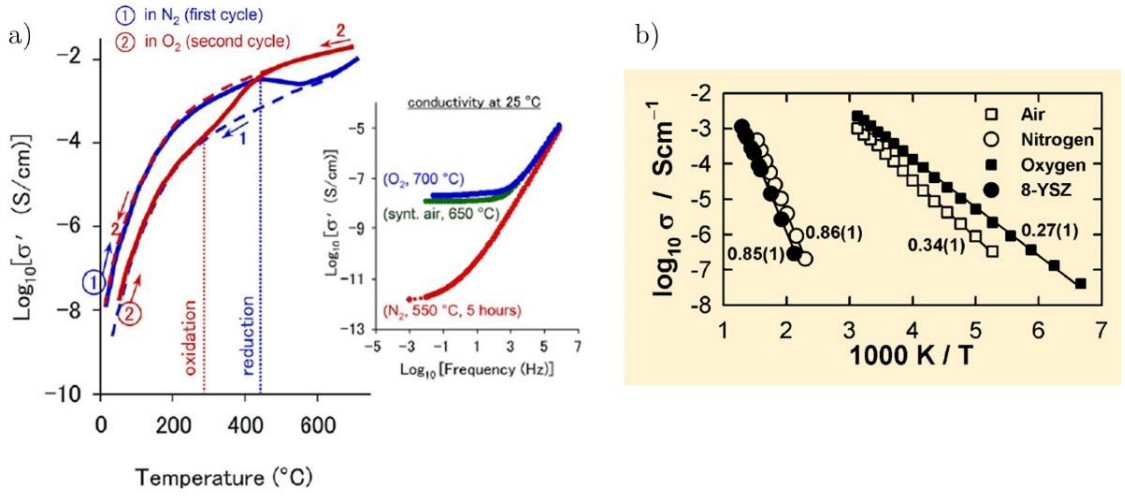

Figure 1.11: Indication of p-type behavior in BFO-based materials from macroscopic conductivity measurements. a) Real part of AC conductivity (1 Hz) as a function of temperature for 0.7BFO-0.3KBT during annealing in (1) nitrogen (first cycle) and (2) oxygen (second cycle). The arrows show the directions of heating and cooling. Inset shows the frequency dependence of AC conductivity measured at room temperature after annealing in different atmospheres [64]. b) Arrhenius plot for Ca-doped BFO ceramics processed under different atmospheric conditions compared with a classic oxide-ion conductor, i.e., 8 mol % YSZ [65].

The decrease of electrical conductivity in a $p(O_2)$-poor atmosphere was reported also for acceptor, Ca-doped BFO ceramics [65] (Figure 1.11b). It was shown that by sintering and cooling the samples from 800 °C in N_2, the conductivity is reduced up to 3 orders of magnitude with respect to air- or oxygen-processed samples and that changes in the conductivity are fully reversible upon changing the $p(O_2)$. In addition, it has been reported that the E_a of samples processed in N_2 is in the range ~0.82–1.04 eV, which is comparable to an E_a of 8 mol % yttria-stabilized zirconia (8-YSZ), the well-known oxide ion conductor. On the other hand, the samples heated in O_2 exhibit an activation energy of ~0.27-0.40 eV, which corresponds to the p-type conductivity associated with Fe^{4+}.

Furthermore, the p-type character in BFO-based materials has also been directly confirmed by Seebeck-coefficient measurements. For example, in 0.9BFO-0.1KBT ceramics a positive Seebeck coefficient was measured in oxygen and air, indicating p-type conductivity, while a negative value was measured in N_2, indicating n-type conductivity (Figure 1.12a) [49]. These results are in agreement with the observed p- to n-type transition from electrical conductivity measurements (see Figure 1.10a) and thus the proposed defect chemistry model (eq. (1.4)-(1.6)). In addition, as can be seen from Figure 1.12a, the material responds instantly to the change of atmosphere, indicating significant mobility of the point defects at this temperature (i.e., 650 °C). Similar observations were also reported in a study by Morozov *et al.* in 0.7BFO-0.3KBT ceramics [64].

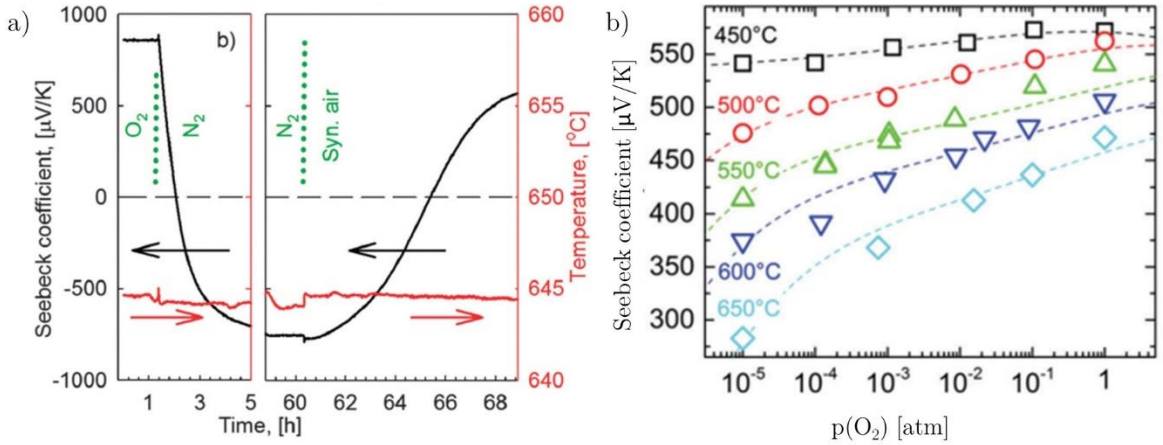

Figure 1.12: Indication of p-type behavior in BFO-based materials from Seebeck coefficient measurements in a) 0.9BFO-0.1KBT ceramics upon changing the atmosphere from O_2 via N_2 to synthetic air at 650 °C [49] and b)undoped BFO ceramics as a function of $p(O_2)$ at various temperatures [66].

The positive sign of the Seebeck coefficient and thus the p-type conductivity was also found in nominally undoped BFO within the entire $p(O_2)$ range, i.e., 10^{-5} to 1 atm (Figure 1.12b) [66]. However, in this specific study by Schrade *et al.*, the Seebeck coefficient showed a small dependence on $p(O_2)$, while the measurements of electrical conductivity showed almost no $p(O_2)$ dependence (not shown here). This is not consistent with the study by Brinkman *et al.* [53] on undoped BFO and studies on Ca-doped BFO [65] or BFO-KBT [49], [64] solid solutions, where a strong $p(O_2)$/atmosphere dependence was observed (see Figure 1.10b, Figure 1.11a). Nevertheless, considering that these ceramics used in that study exhibited very low relative densities (~83 %) and that no reports about the microstructure and the concentration of secondary phases were provided, one might conclude that these results should probably be considered with caution.

The presence of Fe^{4+} ions, which are responsible for the p-type conductivity in BFO-based ceramics, has also been confirmed by high-resolution synchrotron X-ray absorption spectroscopy (XAS). It was found that X-ray absorption near-edge structures (XANES) spectra of Co-doped BFO samples exhibit a shift of the Fe K-edge towards a higher energy relative to Fe K-edge in Fe_2O_3 (Fe^{3+}), indicating the coexistence of Fe^{3+} and Fe^{4+} (Figure 1.13) [68]. This shift has not been observed in undoped BFO, which could be related to the higher concentration of Fe^{4+} in Co-doped samples, which would be consistent with Co acting as an acceptor. The presence of Co^{2+} was confirmed in another study on Co-doped BFO ceramics [69]. On the other hand, in $BiCoO_3$ and $BiCoO_3$–$BiFeO_3$ solid solutions, the oxidation state of Co is presumably 3+. These compounds where only Co is present or when Co concentration is significantly higher to that reported in ref. [68], have received a lot of interest due to high polarization, however, it should be noted that they are stable only at high pressure (e.g., 3 GPa or more) [70]–[72].

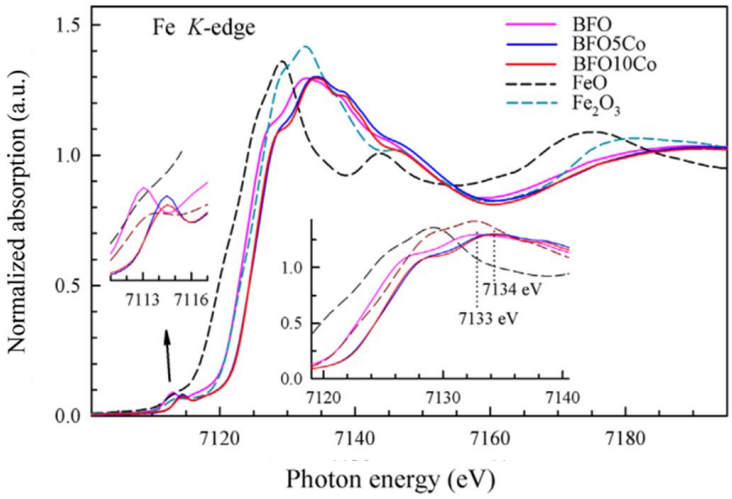

Figure 1.13: Fe K-edge XANES spectra of BFO, Co-doped BFO samples and standards (FeO, Fe_2O_3) [68]. In addition to experimental studies, the presence of Fe^{4+} is further supported by theoretical studies on BFO using DFT [73]–[75]. Furthermore, the DFT calculations showed that under oxygen-rich conditions the formation of $V_{Fe}^{\prime\prime\prime}$ and, in particular, $V_{Bi}^{\prime\prime\prime}$ is energetically preferred over $V_O^{\bullet\bullet}$. In addition, the cation vacancies form shallow acceptor levels within the bandgap, which means that they are easily ionized, resulting in the formation of holes and p-type conductivity. On the other hand, it has been shown that under oxygen-poor conditions the formation of $V_O^{\bullet\bullet}$ is most preferable.

In addition to the defects that are responsible for the electrical conductivity, recent literature data on BFO also elaborates possible defect complexes in this perovskite, which are often assumed to dominate the DW pinning behavior (see chapter 1.1.3). From this perspective, Geneste *et al.* [75] investigated the cation and oxygen vacancies in BFO, as well as cation-oxygen divacancies in different atomic configurations. They found that the association energies of cation-oxygen vacancies (i.e., $V_{Bi}^{\prime\prime\prime} - V_O^{\bullet\bullet}$, $V_{Fe}^{\prime\prime\prime} - V_O^{\bullet\bullet}$) are almost always negative, indicating that they are attracted to each other and tend to form defect complexes. Figure 1.14 displays the association energies of $V_{Bi}^{\prime\prime\prime} - V_O^{\bullet\bullet}$ and $V_{Fe}^{\prime\prime\prime} - V_O^{\bullet\bullet}$ divacancies as a function of the total charge state (q) for different $V_{Bi}^{\prime\prime\prime}/V_{Fe}^{\prime\prime\prime} - V_O^{\bullet\bullet}$ distances. The most stable configurations are those with the shortest distances and the strongest attraction can be found for the association of fully ionized vacancies, i.e. $V_{Bi}^{\prime\prime\prime}/V_{Fe}^{\prime\prime\prime}$ and $V_O^{\bullet\bullet}$ (total charge q=-1), probably due to electrostatic interaction. The most stable

configuration corresponds to the shortest angle between the polarization and electric dipole of the defect complex, presumably leading to the imprint (biasing) effect.

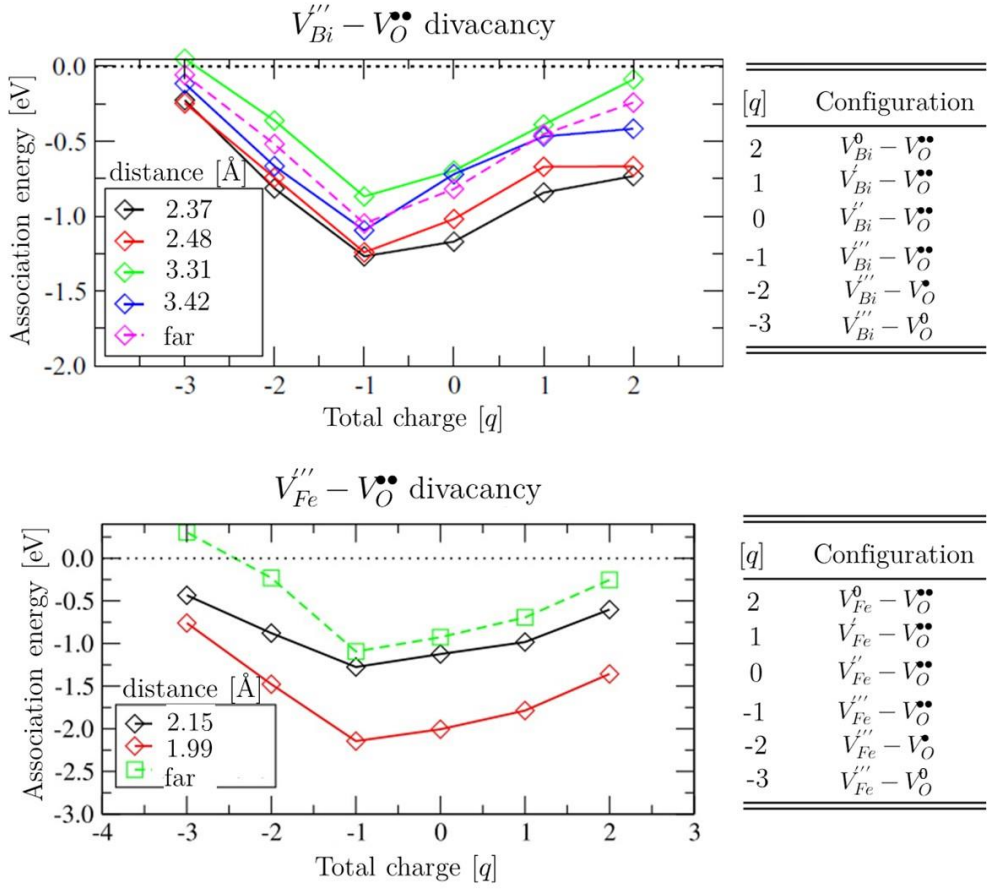

Figure 1.14: Association energies of $V'''_{Bi} - V^{\bullet\bullet}_O$ and $V'''_{Fe} - V^{\bullet\bullet}_O$ divacancies as a function of the total charge (q) depending on the distance between the cation and oxygen vacancy (given in Å) [75]. The total charge depends on the degree of ionization, for example, q=-1 corresponds to fully ionized vacancies, i.e., V'''_{Bi}/V'''_{Fe} and $V^{\bullet\bullet}_O$.

1.2.1.1 Effect of doping

The literature data on doping in BFO ceramics and thin films is vast. Despite the inherent processing problems related to BFO and the persistence of secondary phases in ceramics, some general conclusions, particularly on the effect of donor dopants on the conductivity, can be made.

The current data on acceptor-doped BFO reports both decreased and increased electrical conductivity with respect to undoped BFO. For example, the study by Mazumder *et al.* [76] showed that doping BFO ceramics with Pb^{2+} decreases the electrical conductivity by decreasing the Fe^{2+} concentration, as explained by the authors. However, after a certain level of dopant (~>5 at.%), the conductivity started to increase. In the case of 5 at.% Mn-doped BFO ceramics, the electrical conductivity was reduced by four orders of magnitude with respect to the undoped BFO [77]. The authors concluded that the possible valence state of Mn doping could be 2+, resulting in the conversion of Fe^{2+} into Fe^{3+} and consequently lower conductivity. None of these mechanisms, however, are supported by any additional experimental or theoretical data.

In strong contrast to the studies in ref. [76], [77], several other studies suggest that the electrical conductivity of BFO ceramics is increased by the introduction of acceptor dopants, such as Pb^{2+}, Ca^{2+}, Sr^{2+}, Ba^{2+} [78], Zn^{2+} [79] and Ni^{2+} [80] due to an increased concentration of $V_O^{\bullet\bullet}$, which has been in ref. [78] supported by Mossbauer spectroscopy.

The literature on the donor doping of BFO is, in general, consistent, in that almost all of the studies report on a decrease of the electrical conductivity with respect to undoped BFO by using different donor dopants, such as Nb^{5+} and Ti^{4+}. For example, it has been shown that doping with Nb^{5+} decreases the electrical conductivity of BFO by ~6 orders of magnitude [81]. However, the Nb introduction significantly reduced the grain size, i.e., from ~100 μm in undoped BFO to ~1 μm in 1 mol% Nb-doped sample. The decreased conductivity could be related to the possible segregation of Nb at the grain boundaries and thus increased grain-boundary resistance. Indeed, Nb^{5+} is a low diffusing ion [82] and in combination with the relatively low sintering temperatures used for BFO, i.e., typically ~800 °C, it could result in little or no diffusion.

Much research has been done on doping BFO with Ti^{4+} and it has been shown in several studies [83]–[85] that the conductivity decreases by several orders of magnitude, which is commonly explained through the inhibited formation of $V_O^{\bullet\bullet}$.

1.2.2 Domain-switching behavior: aging and de-aging

Investigations of the ferroelectric properties of BFO-based materials are often challenging due to the unfortunate combination of high electrical conductivity (up to ~10^{-2} $\Omega^{-1}m^{-1}$) and high coercive field (up to 80 kV cm^{-1}) of BFO [48]. Considering the high leakage current and low breakdown field, it is often the case that authors report sub-coercive (unsaturated) *P-E* loops [46], [55], which often display a rounded shape, suggesting a dominant role of the electrical conductivity on the polarization response. Remnant polarization and coercive fields are often wrongly determined from such loops. This problem has been addressed in ref. [86] by comparing the loops commonly reported for BFO-based materials (such as those in ref. [46], [55]) with those obtained from domestic objects such as the skin of an Ag-electroded banana. It has been shown that these kinds of polarization loops are characteristic for materials with a high electrical conductivity and they have little to do with the ferroelectric behavior, thus care should be taken in the analysis of the *P-E* loops of BFO.

Some representative saturated *P-E* loops from the literature are presented in Figure 1.15. BFO exhibits typical hardening features in both non-poled (aged) and poled samples (compare Figure 1.15 and Figure 1.4c). The pinched or double hysteresis loop in BFO was first studied by Yuan *et al.* [62] and has been, due to the analogy with hard PZT (Figure 1.9), explained using the symmetry-conforming principle [19], i.e., the formation of acceptor centers–oxygen vacancy defect complexes (Figure 1.6).

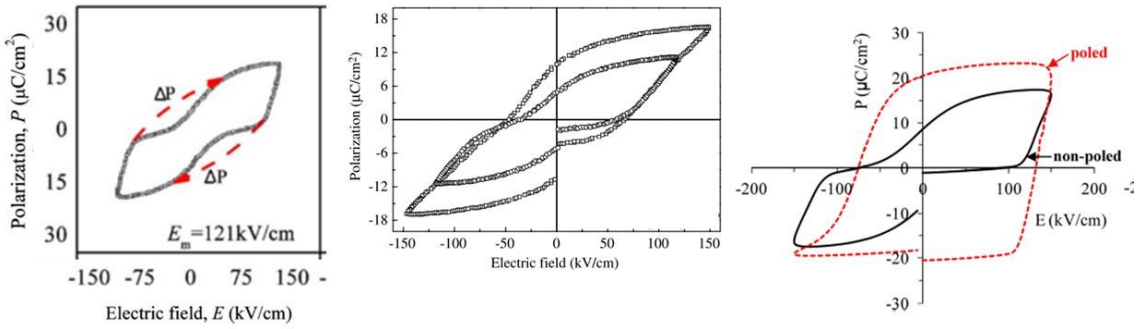

Figure 1.15: Macroscopic hardening features in P-E loops of BFO ceramics [62], [87], [88]; for P-E loop denoted with "poled", the sample was poled at 80 kV cm^{-1} of DC electric field.

The de-aging of BFO ceramics is qualitatively the same as observed in hard PZT (Figure 1.9a, [6]) and has been similarly demonstrated by quenching, as shown in Figure 1.16 [89]. In this case, the sintering of BFO ceramics at 760 °C was followed by annealing to various temperatures, i.e., 450 °C, 760 °C and 900 °C, and subsequent quenching in water. The P-E loops after quenching from 450 and 760 °C show only minor changes with respect to as-sintered samples (denoted as non-Q). On the other hand, the P-E loop after quenching from 900 °C was depinched and exhibited significantly lowered E_c and increased P_r with respect to as-sintered ceramics. These results confirm that the defects can be disordered by annealing above T_C (~830°C) followed by quenching, and that the origin of the loop deformation is indeed due to the presence of defects, similar to those observed in hard PZT (see Figure 1.9a).

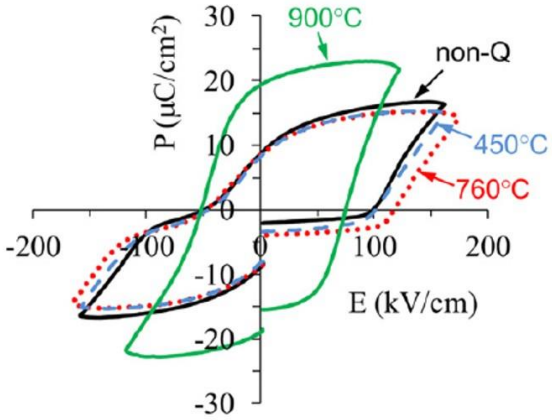

Figure 1.16: P-E loops of sintered ceramics (denoted as non-quenched, non-Q) and subsequently quenched in water from 450 °C, 760 °C and 900 °C [89].

Furthermore, considering the similarities in the ferroelectric behavior of hard PZT and that of BFO-based materials, it is not surprising that the same defects as identified in hard PZT (acceptor centers–oxygen vacancy defect complexes) have been considered to also lie at the origin of hardening in BFO materials. However, no evidence or systematic study about the type and/or location of defects and their influence on ferroelectric switching in BFO has been provided so far.

1.2.3 Conductive domain walls and piezoelectric response

Enhanced domain-wall conductivity was first demonstrated for 109° and 180° domain walls in BFO thin films by Seidel *et al.* [90] (Figure 1.17a). They described the observed enhanced conductivity of the walls by two different mechanisms, i.e., electrostatic potential steps, which should attract charged defects to the walls, and reduction of the band gap, both of which should increase domain-wall conductivity. Later, the former mechanism was also suggested by Farokhipoor *et al.* [91], i.e., the domain-wall conductivity is dominated by the accumulation of charged point defects, which control the local transport properties. Conductive domain walls have also been discovered in BFO ceramics by Rojac *et al.* (Figure 1.17b), both in as-sintered (unpoled) and poled samples [92]. That defects control the DW conductivity by accumulating on the walls was subsequently confirmed by direct atomic-scale analysis [93].

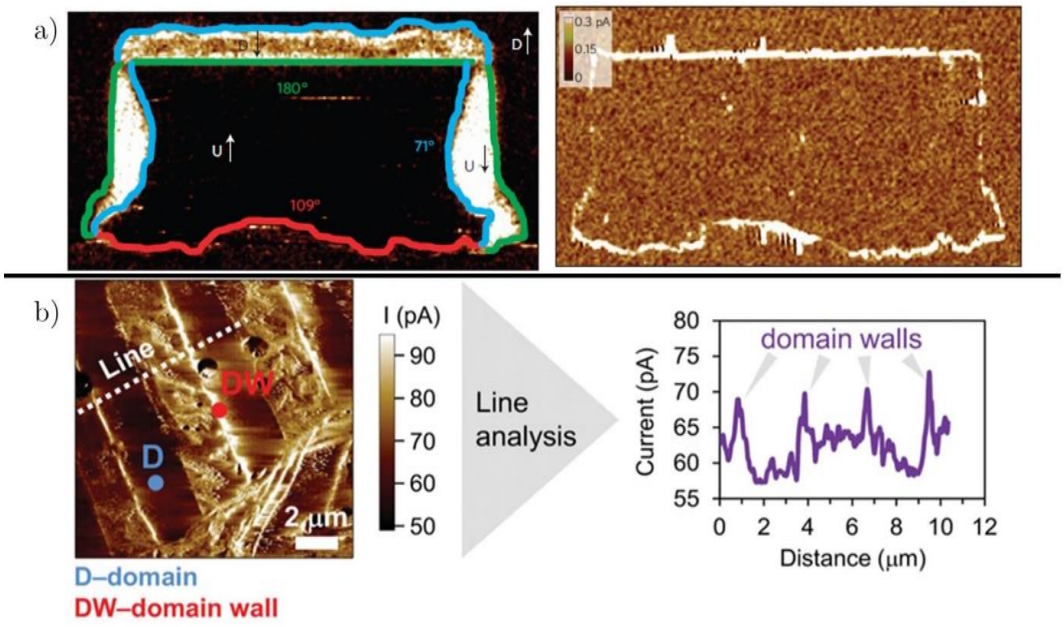

Figure 1.17: Identification of conductive DWs in $BiFeO_3$ a) thin films and b) ceramics. a) In-plane PFM image of a written domain pattern in BFO (110) thin films showing 71°, 109° and 180° domain walls (left panel) and corresponding c-AFM image showing conduction along 109° and 180° domain walls (right panel) [90]. b) c-AFM image of a selected area in ceramic sample (left panel) and current profile across DWs (right panel) [92].

The atomic-scale chemical and structural evidence of the segregation of V'''_{Bi} and $Fe^{\bullet}_{Fe}$ defects at conductive DWs in BFO ceramics demonstrated the p-type DW conduction (Figure 1.18) [52]. Furthermore, the comparison of the conductive atomic force microscope (c-AFM) signal at DWs in the air-sintered sample and N_2-annealed sample showed that their conductivity is significantly reduced after annealing in N_2, confirming the local p-type conduction. However, in contrast to the p-type conductivity of DWs identified in BFO ceramics, the studies on BFO thin films suggest n-type conductivity at DWs, as it has been shown that their conductivity decreases with increasing $p(O_2)$ [91], [94]. This could be related to different processing conditions in terms of temperature and $p(O_2)$ when preparing ceramics or thin films, and thus to the defect chemistry.

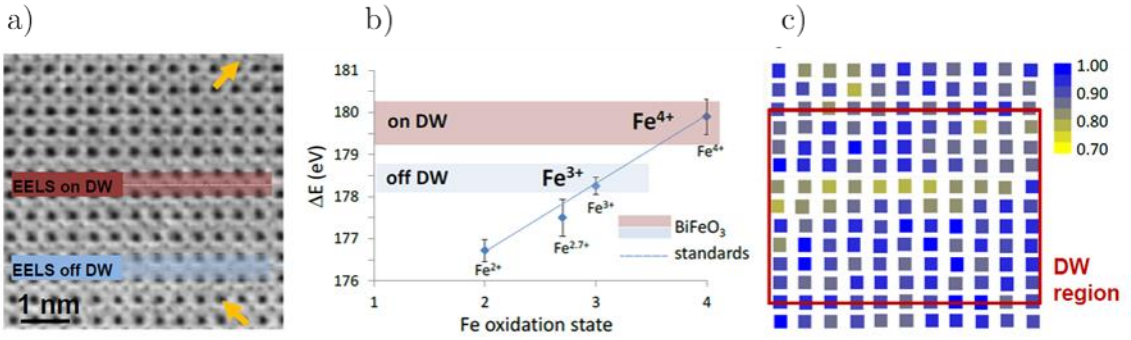

Figure 1.18: Accumulation of charged defects at DWs in BFO. a) ABF-STEM image indicating on and off DW areas where EELS analyses were performed. b) Energy onset difference (ΔE) between O-K and Fe-L_3 edges, used for determining the oxidation state of Fe, shown for on and off the DW regions in BFO and compared with ΔE determined on standards (data points and dashed line). c) Normalized distribution map of Bi-column intensities across the DW showing ~20 % reduction of intensity in the middle of the DW which confirms the presence of accumulated V_{Bi}'''.

The movement of conductive DWs in BFO ceramics and their contribution to the macroscopic piezoelectric response under sub-switching conditions were investigated by measurements of the converse piezoelectric effect [92]. The ceramics exhibited a particular frequency dispersion observed as an abrupt increase in d_{33} and piezoelectric $tan\,\delta$ at low frequencies, i.e., <4 Hz (Figure 1.19a). Such behavior is different from the frequency independent behavior in hard PZT (similar to that in Figure 1.2f) or logarithmic frequency dependence in soft PZT (Figure 1.19a), interpreted in terms of the field-induced motion of DWs in a medium with random pinning centers [10]. Furthermore, it was shown that the large nonlinear and hysteretic response at low driving frequencies (Figure 1.19b), is related to the irreversible displacement of conductive DWs, which was later directly confirmed by *in-situ* X-ray powder diffraction (XRD) analysis [95]. The measured unusual negative piezoelectric phase angle (Figure 1.19b), also confirmed by *in-situ* XRD analysis [95], gave strong indications of the Maxwell-Wagner piezoelectric effect, which was explained in terms of the internal field redistribution in grains owing to the presence of conductive DWs.

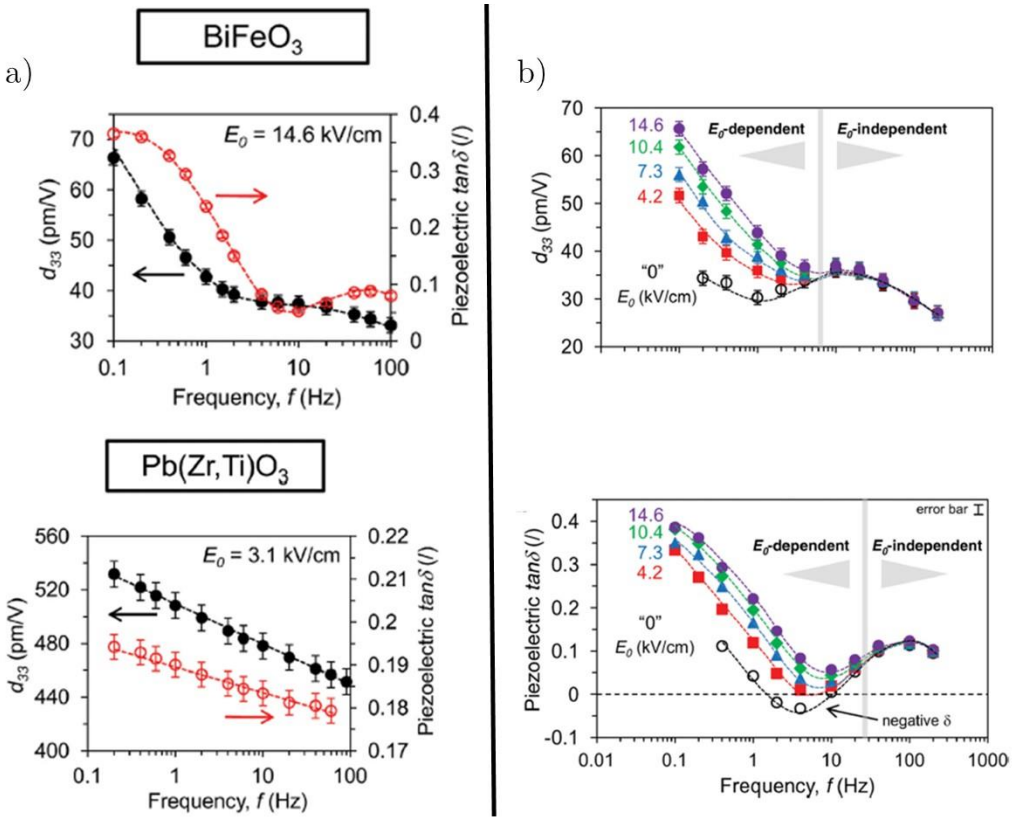

Figure 1.19: Converse piezoelectric response of BFO and Nb-doped morphotropic PZT under sub-switching conditions. a) Piezoelectric d_{33} coefficient and piezoelectric $tan\,\delta$ as a function of the frequency of the driving electric field for BFO and Nb-doped PZT. The samples were measured at different fields E_0 but a comparable E/E_c ratio (~0.2) b) Frequency dispersion and field dependence of d_{33} coefficient and piezoelectric $tan\,\delta$ of BFO.

The observed large DW displacements at low frequencies in BFO is supported by the model proposed by Postnikov *et al.* [96]. According to this model, the DWs are pinned by accumulated defects, as is indeed the case in BFO (Figure 1.18), however, under the application of sub-switching fields, for a prolonged time depinning occurs and defects move together with the DWs. Therefore, the model suggests that the irreversible DW displacements become strongly time dependent and should occur at low driving-field frequencies, which was indeed experimentally observed in BFO ceramics (Figure 1.19).

The movement of defects along with the DWs after the application of an electric field has been recently proven with an *ex-situ* electric field STEM experiment [93]. In contrast to an unpoled (pristine) sample, where V_{Bi}''' and $Fe_{Fe}^{\bullet}$ tend to accumulate at DWs (as shown in Figure 1.18), no evidence of V_{Bi}''' accumulation was found by STEM analysis inside the switched DW. However, the EELS analysis on the newly created DW revealed the presence of Fe^{4+}. These results suggest that V_{Bi}''' are unable to follow the DWs' displacements due to their low diffusivity and that at DWs in poled samples mostly $Fe_{Fe}^{\bullet}$ are accumulated. The movement of the hole defects together with the DWs is in agreement with the persistence of DW conductivity in poled BFO ceramics [92]. Furthermore, these results suggest that the pinning in BFO is associated with individual defects and not defect complexes as in BT, PT and PZT [20], [28]. This is in agreement with DFT calculations showing that V_{Bi}''' and $Fe_{Fe}^{\bullet}$ do not have a tendency for close association [75]. The question that was not answered in that study or others, however, is whether and how $V_O^{\bullet\bullet}$ play a role in the dynamic pinning mechanism.

The DW dynamics in BFO ceramics at sub-switching conditions has recently been investigated using time-resolved, stroboscopic *in-situ* XRD analysis [95]. Figure 1.20a shows the extracted lattice strain ($\varepsilon_{intrinsic}$) and change in non-180° domain texture (Δf_{111}) as a function of the frequency obtained at an electric field amplitude of 60 kV cm^{-1}. The lattice strain increases while the change in the non-180° domain texture decreases with increasing frequency. These results demonstrate the decoupling of lattice strain and DW motion in BFO ceramics, which becomes very evident at frequencies below ~10 Hz. Furthermore, they found that under the application of an electric field at low frequencies (e.g., 1 Hz), the phase angle of the lattice-strain response is negative (strain leads the driving field), while the phase angle of the macroscopic strain (measured from the sample's surface displacement), which takes into account lattice strain and local domain-wall-induced strain from individual grains, is positive (strain lags behind the driving field) (see Figure 1.20b). While domain-wall motion shows a conventional positive phase-angle response and dominates the macroscopic phase angle, the authors showed evidence of a negative phase angle arising from the lattice response.

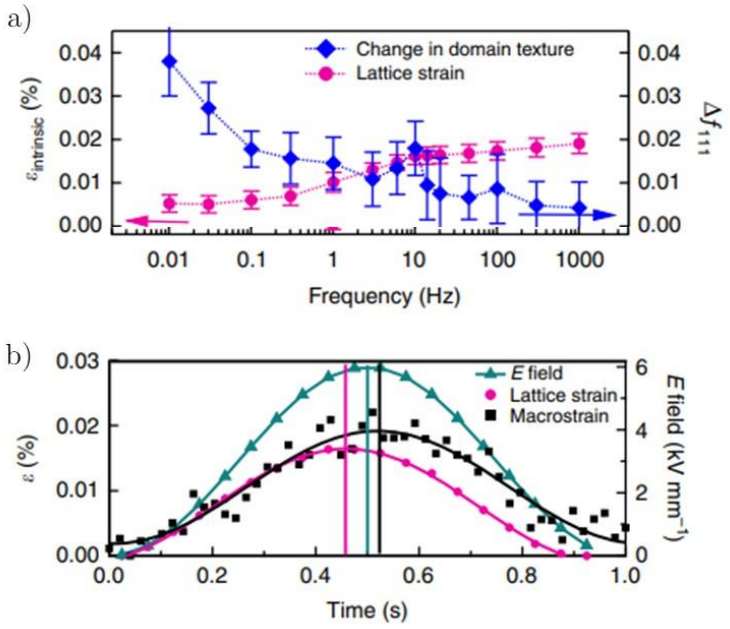

Figure 1.20: Stroboscopic *in-situ* XRD analysis of DW dynamics in BFO ceramics at sub-switching conditions [95]. a) Calculated total lattice strain ($\varepsilon_{intrinsic}$) and change in non-180° domain texture (Δf_{111}) as a function of frequency under the application of 60 kV cm^{-1}. b) Time dependence of driving electric field, macroscopic strain and lattice-strain response at 1 Hz of unipolar cycling. The macroscopic strain maximum (black curve and markers) is in time scale appearing after the electric field maximum (green curve and markers), while the lattice strain (red curve and markers) is appearing before the field maximum. This shows that the lattice-strain response is advancing the field, directly proving the negative phase angle related to Maxwell-Wagner (M-W) effects.

The unusual negative phase angle in the lattice-strain response is a strong indication of the non-uniform electric field distribution inside the ceramics, which has been attributed to conductive domain walls in BFO ceramics. Based on the overall data, the authors proposed a model shown schematically in Figure 1.21.

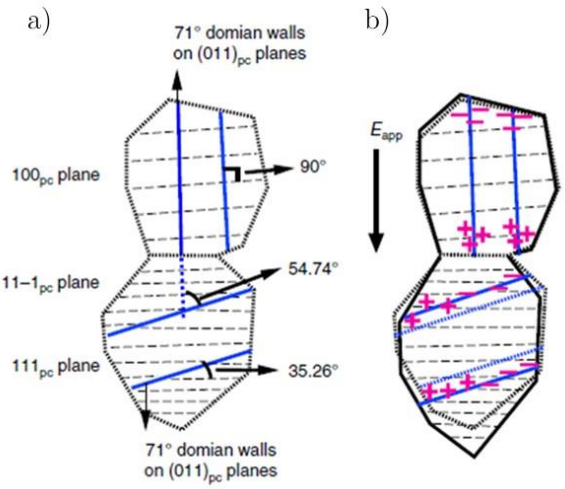

Figure 1.21: Schematic representation of two grains in poled BFO [95]. a) Solid blue lines and dashed black lines represent 71° domain walls and diffraction planes, respectively. The angles of 90°, 54.74° and 35.26° correspond to the angles between DW and electric field vector and are different due to different crystallographic orientations. b) Charge distribution on conductive DWs after the application of electric field is different for grains with different crystallographic orientations with respect to the field axis. This results in different effective fields within individual grains and consequently different contributions to lattice strain and a change in the non-180 DW motion in different grains.

The model considers two grains, in this case in the $\{100\}_{pc}$ and $\{111\}_{pc}$ crystallographic orientations (pc refers to pseudo-cubic), where the direction represents the crystallographic planes aligned perpendicular to the applied electric field vector. The 71° DW lying along the 011_{pc} planes is in the $\{100\}_{pc}$ oriented grain family nearly parallel to the electric field vector; in contrast, these same DWs in the $\{111\}_{pc}$ grain family will form an angle of 57.74 ° with the electric field vector. This means that the conductive DW have different orientations with respect to the electric field direction when present in different grain families. The migration of point defects at low driving frequencies causes a drop of the electric field in the upper grain due to the higher conductivity of that grain considering that the conductive DW is oriented parallel to the electric field. Inversely, the field drop in the upper grain will be counterbalanced by the increase of the field in the bottom grain. Due to the specific orientation of the grains with respect to the electric field axis, the upper grain will mainly respond via lattice strain, while the bottom grain will respond with an additional domain-wall contribution. Therefore, at low frequencies, due to the particular inverse electric-field distribution in the two grains, a decoupling between the lattice strain and the DW motion occurs (see Figure 1.20a, below ~10 Hz), i.e., the lattice strain decreases and the domain-wall contribution increases with decreasing frequency (due to the mentioned redistribution of internal fields). The model was shown to support well the experimental data and predicted not only the measured strain decoupling but also the measured negative phase angle of the lattice-strain response (Figure 1.20b).

Chapter 2

Aims and Hypothesis

BFO is macroscopically characterized by elevated electrical conductivity and ferroelectric hardening behavior, as evidenced by a large number of independent studies [46], [55], [57], [61], [87], [89]. The literature, however, is inconsistent about the origin of this behavior as it has been attributed to different types of defects including V_{Bi}''', $V_O^{\bullet\bullet}$, Fe_{Fe}' and $Fe_{Fe}^{\bullet}$ as well as defect complexes, such as $V_{Bi}''' - V_O^{\bullet\bullet}$, $Fe_{Fe}' - V_O^{\bullet\bullet}$ and $V_{Bi}''' - Fe_{Fe}^{\bullet}$ [46], [47], [56], [78], [83], [97]–[99]. Therefore, the origin of the elevated electrical conductivity and hardening in BFO remains unclear and calls for a systematic study. The explanation of these complex defect-related mechanisms would be important in terms of designing properties in the current hot-topic BFO-based solid solutions, such as those with $PbTiO_3$ [100] and $BaTiO_3$ [101], [102], which are either already commercialized [103] or considered as piezo-ceramics for high-temperature applications (T>200°C).

The purpose of the thesis was to controllably introduce charged point defects in BFO and investigate how these defects affect the electrical and electromechanical properties of the material, in particular the electrical conductivity, dielectric and piezoelectric response as well as polarization switching behavior. The aim was to investigate the microscopic DW pinning mechanisms, which should be understood in the first place. To achieve this, a combined approach of doping[3] BFO with Co along with the post-annealing of doped ceramics in different partial pressure of oxygen was adopted.

The first part of the thesis is focused on the influence of cobalt concentration on the defect chemistry and ferroelectric hardening in BFO ceramics. The aims of the work within this first part were:

- To synthesize $Bi(Fe_{1-x},Co_x)O_3$ ceramics, where x = 0, 0.0025, 0.005, 0.01 and 0.015 with high density, good level of homogeneity and minimum presence of secondary phases.
- To investigate the relationship between the Co concentration and electrical conductivity as well as ferroelectric hardening in terms of domain switching and piezoelectric response.
- To evaluate the oxidation state of Co in order to fully understand its effect on the measured properties.

The hypotheses for the first part were:

- Taking into account the known difficulties to prepare single-phase BFO [104], [105], the prepared Co-doped ceramics will contain secondary phases. However, considering the similar ionic radii of Co and Fe ions (0.61 Å for Co^{3+} versus 0.645 Å for Fe^{3+}; [106]), an efficient incorporation of Co ions into the BFO's perovskite structure is expected. This would potentially result in a comparable concentration

[3] Note that this is not doping from a chemical point of view but rather a chemical substitution as the two end members in the solid solution ($BiFeO_3$ and $BiCoO_3$) have the same crystal structure (perovskite).

of secondary phases in all compositions, still allowing us to evaluate the effect of the dopant.

- Considering the recent study on Co-doped BFO ceramics, which confirmed the presence of Fe^{4+} states induced by Co doping [68], the electrical conductivity will increase with Co concentration as Fe^{4+} are the main defects controlling the p-type conductive behavior of this material.

The second part of the thesis is focused on the influence of the annealing atmosphere on the defect chemistry and ferroelectric hardening of Co-doped BFO ceramics. The aims of the work within this part were:

- To explore the influence of annealing atmosphere on electrical conductivity and domain switching of Co-doped BFO ceramics.
- To determine whether the electrical conductivity of Co-doped BFO ceramics under different partial pressure of oxygen is p- or n-type.

The hypotheses for the second part were:

- Considering the recent evidence that Co introduces Fe^{4+} states in BFO ceramics [68], it is assumed that Co-doped BFO ceramics will retain their p-type behavior; therefore, the electrical conductivity will decrease by post-annealing in nitrogen due to the reduction of Fe^{4+} into Fe^{3+}.
- Since oxygen vacancies are strong pinning centers for domain walls, as known for PZT, the hardening will be enhanced by increasing the concentration of oxygen vacancies, i.e., by the post-annealing of sintered samples in a low partial pressure of oxygen.

The third part of the thesis is focused on the identification of charged point defects and defect complexes and their location in Co-doped BFO ceramics to fully assess the microscopic pinning mechanism. The aims of the work within this part were:

- To analyze the local electrical properties, in particular the electrical conductivity of grain boundaries, domain walls and domains within a grain, in Co-doped BFO ceramics annealed in different partial pressure of oxygen.
- To identify charged point defects and the possible presence of defect complexes in Co-doped BFO ceramics by experimental methods, including chemical analysis (electron-energy-loss spectroscopy) using scanning transmission electron microscopy and electron paramagnetic resonance.
- To investigate the influence of Co introduction on the electronic properties of BFO ceramics and thus the defect chemistry, using ab-initio computations (density functional theory, DFT).

The hypotheses for the third part were:

- Considering that BFO ceramics contain p-type conductive domain walls [52], it is assumed that the domain wall conductivity in Co-doped BFO ceramics will decrease after post-annealing in nitrogen.
- Like with $Fe'_{Zr/Ti} - V_O^{\bullet\bullet}$ defect complexes in Fe-doped (hard) PT/PZT [16], [30], in BFO the acceptor centers (Co'_{Fe}) and oxygen vacancies ($V_O^{\bullet\bullet}$) will tend to bind together, creating strong and orientable pinning centers through which hardening in BFO could be controlled. Since electron-hole defects are more mobile than $V_O^{\bullet\bullet}$, the pinning effect of the holes accumulated at DWs (Fe^{4+} states) will be much weaker than those mediated by $V_O^{\bullet\bullet}$-related complexes.

Chapter 3

Materials and Methods

3.1 Processing of Undoped and Co-Doped BFO Ceramics

3.1.1 Chemicals, equipment and accessories

The lists of chemicals, accessories and equipment that were used in the processing procedures within this investigation are collected in Table 3.1 and Table 3.2, respectively.

Table 3.1: List of chemicals in alphabetical order.

Chemicals	Specification and producer	Role
Bi_2O_3	99.999%, Alfa Aesar, Ward Mill, Massachusetts, USA	Starting powder for synthesis
C_2H_5OH	Absolute ethanol, RS-Anhydrous-for analysis, Carlo Erba, Milano, Italy	Liquid medium for milling purposes
Co_3O_4	99%, Alfa Aesar, Ward Mill, Massachusetts, USA	Starting powder for synthesis
Fe_2O_3	99.99 %, Alfa Aesar, Ward Mill, Massachusetts, USA	Starting powder for synthesis
Pt foil	99.999%, Zlatarna Celje, Celje, Slovenia	Substrate for calcining the powders

Table 3.2: List of equipment and accessories in alphabetical order.

Item	Specification and manufacturer
Chamber furnace	Custom-made, Terna d.o.o., Ljubljana, Slovenia
Grinding jars	Polyethylene (PE), custom-made, JSI, Ljubljana, Slovenia
Isostatic press	401C-0063, Autoclave Engineers, Erie, Pennsylvania, USA
Milling balls	Yttria-stabilized-zirconia (YSZ), Tosoh Corporation, Tokyo, Japan
Planetary mill	PM400, Retsch, Haan, Germany
Tube furnace	Custom-made, Terna d.o.o., Ljubljana, Slovenia
Uniaxial press	PW 10, P/O/Weber GmbH, Ramshalden, Germany

3.1.2 Solid-state powder synthesis and sintering

The processing steps for the synthesis of undoped and Co-doped BFO ceramics are schematically shown in Figure 3.1. Ceramic powders with the nominal formula $Bi(Fe_{1-x},Co_x)O_3$, for x = 0, 0.0025, 0.005, 0.01 and 0.015, subsequently referred to as the 0.0 Co, 0.25 Co, 0.5 Co, 1.0 Co and 1.5 Co, were prepared by solid-state synthesis using Bi_2O_3, Fe_2O_3 and Co_3O_4 as the starting powders.

The starting powders were separately pre-milled in a planetary mill prior to homogenization. The Bi_2O_3 and Fe_2O_3 were separately milled in a 125-mL PE vial with 210 g of Φ3 mm YSZ milling balls. The Co_3O_4 powder was milled in a 54-mL PE vial with 96 g of Φ3 mm YSZ milling balls. The milled and dried reagents were weighed in a stoichiometric ratio taking into account weight losses and purity, and homogenized in a 54-mL PE vial with 96 g of Φ3 mm YSZ milling balls.

All the powders and powder mixtures were milled and dried under the conditions described in the following. The milling was performed for 4 h in a planetary mill set at 200 min^{-1} of the main-disc rotational frequency. The drying step was performed at 120 °C until a constant weight was reached and afterwards sieved through a 55-mesh sieve.

The homogenized mixtures were then placed in a covered alumina crucible on a Pt-foil and calcined at 740 °C for 4 h in a chamber furnace with heating and cooling rates of 10 °C min^{-1}. The calcination step was followed by milling, drying and sieving using the same conditions as for the homogenization.

The calcined powders were compacted into a cylindrical samples of Φ8 mm (or Φ10 mm) by applying 50 MPa of uniaxial pressure. The pellets with green density of ~50% were further isostatically pressed at 300 MPa and sintered in air at 800 °C for 4 h in a tube furnace with heating and cooling rates of 10 °C min^{-1}.

Ceramic samples used for *in-situ* measurements of the DC conductivity and Seebeck coefficients were prepared as follows. The calcined powders were mixed with a 20 wt% aqueous solution of organic binder (refined D-camphor, E. Merck, Darmstadt, Germany) and uniaxially pressed with 50 MPa into bars of approximate dimensions 40 x 5 x 5 mm^3. Afterwards, the bars were additionally isostatically pressed with 300 MPa and placed in an alumina crucible on a Pt foil. Following the binder burnout at 200 °C for 4 h with a heating rate of 1 °C min^{-1}, the samples were sintered at 800 °C for 4 h with heating and cooling rates of 10 °C min^{-1}.

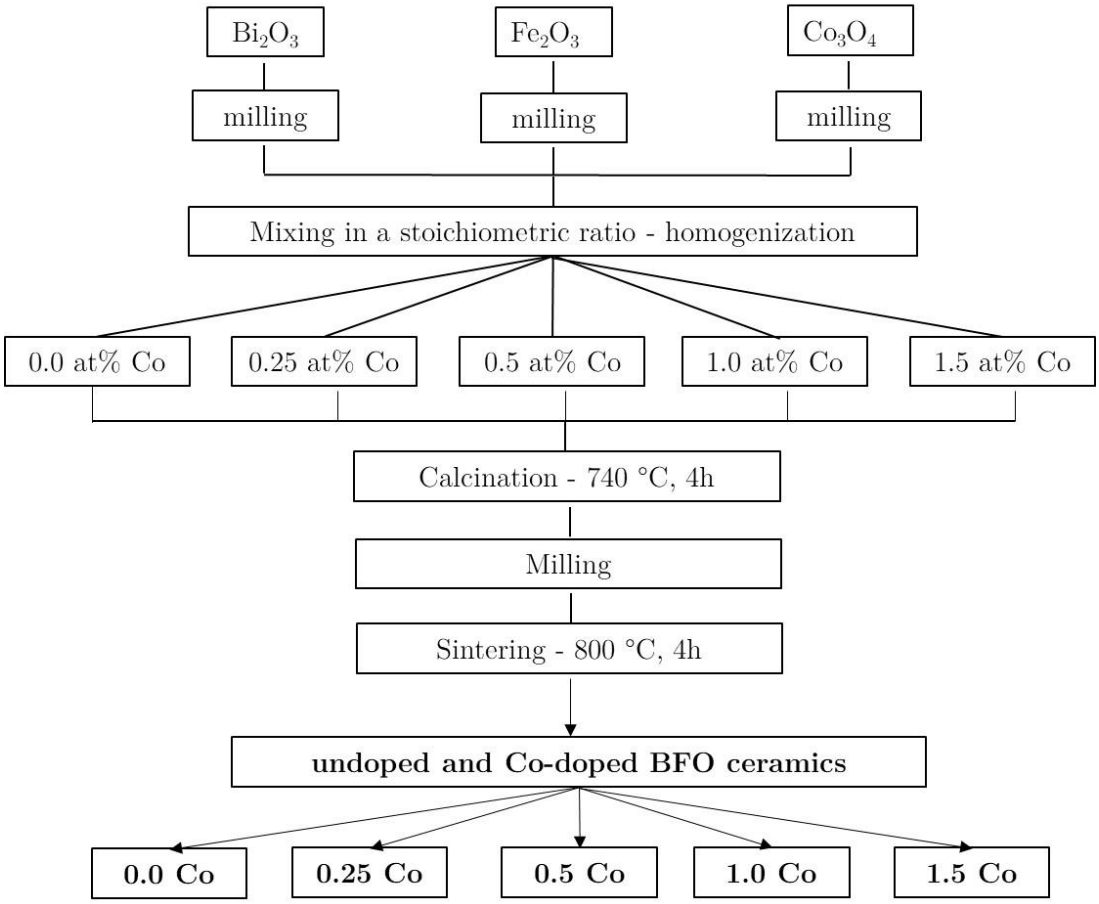

Figure 3.1: Schematic illustration of the processing steps for the solid-state synthesis of BFO ceramics with different Co dopant concentrations.

3.1.3 Post-annealing of sintered samples

The influence of annealing atmosphere on domain switching and electrical conductivity at room temperature was investigated for sintered pellets that were post-annealed i) in flowing N_2 (Messer, 4.6) at 700 °C with zero holding time and with a heating/cooling rate of 2 °C min^{-1}, or ii) in 10 atm O_2 at 700 °C with a 24-h hold time and a heating rate of 5 °C min^{-1} and a cooling rate of 0.5 °C min^{-1}. As-sintered samples were used as a reference.

3.2 Characterization Methods

3.2.1 Powders

The particle size and particle size distribution of the reagents, homogenized mixtures and calcined powders during milling were monitored by granulometric analyses. The measurements were performed in isopropanol (IPA) using a static, light-scattering granulometer (Microtrac S3500 Particle Size Analyzer, Montgomeryville, Pennsylvania, USA). Prior to the measurement, the samples were dispersed in IPA and placed in an ultrasound bath.

The weight loss of the powders upon annealing was determined by thermogravimetry (TG) coupled with differential thermal analysis (DTA) (Netzsch STA 409 C/CD, Selb, Germany) using a heating rate of 10 °C min^{-1}. The measurements were performed in an

alumina crucible in air. The weight losses upon heating were considered in the calculation of the stoichiometric mixtures for different compositions.

The phase composition of the powders was determined by X-ray powder diffraction (XRD) analysis using an X'Pert PRO MPD diffractometer with Cu-Kα1 radiation (PANalaytical, Almerlo, The Netherlands) and the X'Celerator detector. The patterns were recorded in the 2θ range from 10° to 78° using a step of 0.016°, with an integration time of 100 s. The data were analyzed with the X'Pert High Score software package and for the qualitative phase analysis the crystallographic cards from the PDF-2 database were used.

3.2.2 Sintering behavior

Dimensional changes of all the pressed powders as a function of temperature were analyzed by optical dilatometry (Leitz, Wetzlar, Germany) in the stage of the homogenized mixtures to obtain the so-called reaction curves and determine the optimal calcination temperatures, as well as after the calcination to obtain sintering curves. For these analyses, the powder compacts were pressed into cylindrical samples of Φ6 mm with a uniaxial pressure of 100 MPa. The changes in dimensions were continuously recorded upon heating with a heating rate of 10 °C min^{-1}. The relative shrinkage ($\Delta l/l_{RT}$) was calculated according to the following equation

$$\frac{\Delta l}{l_{RT}} = \frac{l_{RT} - l_T}{l_{RT}} \tag{3.1}$$

where l_{RT} is the initial sample diameter at room temperature (RT) and l_T is the sample diameter at a selected temperature (T).

The densities of the sintered samples were calculated from the dimensions of the pellets and their masses, as well as with the pycnometer method.
The geometrical (ρ_{geo}) densities were calculated from the measured height, diameter and mass of the pellets using the following equation

$$\rho_{geo} = \frac{m}{\pi r^2 h} \tag{3.2}$$

where m is the mass, r is the radius and h is the height of the cylindrically shaped sample. The density of the samples using a gas-displacement density analyzer (Micromeritics, AccuPyc III 1340 Pycnometer, Georgia, USA) was determined by subjecting the sample to ten consecutive measurements and calculating the average.
For the calculation of the relative density, the theoretical density of $BiFeO_3$ (8.34 g cm^{-3}) was used and the influence of Co on the density was neglected due to the low concentration of the dopant (up to 1.5 at.%).

3.2.3 Phase composition, structure and microstructure of the prepared ceramics

The **phase composition** of the sintered ceramics was investigated using XRD analysis as described in Section 3.2.1, in this case on crushed ceramics. The amount of secondary phase $Bi_{25}FeO_{40}$ was determined by fitting the XRD patterns within the whole 2θ range with the Rietveld refinement method using the Topas R (Bruker AXS, Karlsruhe, Germany) software package [107]. The pseudo-Voight function was used to describe the peak shape, while the background was fitted using a 2nd-order Chebychev function. The quality of the

fit was assessed from the R_{wp} factors of the refined patterns, which were in the range between 8 and 10 %.

The **microstructures** of the sintered samples were investigated using a field-emission scanning electron microscope (FE-SEM) (JSM 7600 F, Jeol, Tokyo, Japan). The ceramic samples were embedded in a resin (Versocit-2, Struers A7S, Ballerup, Denmark), ground using SiC papers with gradations 1200 and 2000 and polished using 3-μm and $\frac{1}{4}$-μm diamond pastes (Struers A7S, Ballerup, Denmark). The samples for the grain size (GS) analysis were additionally thermally etched at 750 °C for 15-30 minutes, depending on the etching level assessed by observation of the sample surfaces using an optical microscope. Prior to the SEM analysis, the samples were deposited on a carbon tape and coated by sputtering a few-nm-thick layer of carbon (Balzers SCD 005, BAL-TEC GmbH, Witten, Germany) in order to provide surface conductivity and avoid charging problems during the SEM imaging. The images were obtained at 15 kV of accelerating voltage, with a working distance of 15 mm. The images were acquired using a COMPO detector (Backscattered Electron Image, BEI).

The GS and GS distributions were determined from SEM images of thermally etched surfaces using Image Tool Software [108]. The GS values are expressed as the Feret's diameter mean values (D_m), which were calculated from the measured area values of the grains (A) using the following equation [109]:

$$D_m = \sqrt{\frac{4A}{\pi}} \tag{3.3}$$

3.2.4 Atomic-scale structure and chemistry

For the investigations using a scanning transmission electron microscope (STEM), the samples were ground, polished down to 100 μm and after dimpling thinned down to electron transparency using a Gatan PIPS ion-milling system. The STEM studies were carried out using a probe Cs-corrected Jeol ARM 200 CF STEM operated at 200 kV.

High-angle annular dark-field (HAADF) images used for analyzing the direction of the Fe displacements from the center of Bi sub-lattice were taken in the $[010]_{pc}$ zone axis and the scan rotation was set so that the a and c crystal directions were parallel to the horizontal and vertical slides of the image, respectively.

Normalized Bi-column intensities were measured using the approach by LeBeau & Stemmer [110], where the average intensity of the background and HAADF STEM detector signal were measured from the image of a HAADF detector (without sample) at non-saturating settings of brightness and contrast. Afterwards, the detector's background intensity was subtracted from the images. The resulting intensity was divided by the background-corrected average intensity signal of the detector. This normalized intensity corresponds to the relative scattering of each atom column. In order to determine the concentration of Bi vacancies inside each column, the experimental intensities were compared with the calculated intensities. The calculations were performed using quantitative STEM (QSTEM) code [111].

Electron-energy-loss spectroscopy (EELS) experiments were collected in STEM mode using a GATAN Quantum ER Dual EELS electron-energy-loss spectrometer, which enables the simultaneous acquisition of low and core loss. The local oxidation state of iron was determined from the energy onset difference between the O-K and Fe-L_3 edges (ΔE) in different standard materials (see Table 3.3). The energy onset was determined at 10% of O-K and Fe-L_3 edge height.

Table 3.3: Experimental ΔE values determined on standards for different Fe oxidation states.

Standard	Producer	Fe oxidation state	ΔE [eV]
$FeTiO_3$	Alfa Aesar; product number 1317	2+	176.7±0.3
$Co_{0.6}Fe_{2.4}O_4$	Synthesized by Gyergyek *et al.* [112]	2.7+	177.5±0.4
Fe_2O_3	Alfa Aesar; product number 14680	3+	178.3±0.2
$BaFeO_3$	Synthesized as reported in ref. [113]	4+	179.9±0.4

3.2.5 Domain structure and local electrical conductivity measurements

Ceramic samples used for the piezo-response force microscopy (PFM) and conductive atomic force microscopy (c-AFM) analyses were post-annealed (after the sintering) in air at 840 °C with zero holding time and a heating/cooling rate of 10 °C min^{-1}. Such a preparation procedure was adopted in order to increase the grain and domain size and thus to allow easier identifications of the domains and domain walls. For comparison, a set of such pre-annealed samples was additionally annealed in flowing N_2 (Messer, 4.6) at 700 °C with zero holding time and with a heating/cooling rate of 2 °C min^{-1}. The sample surfaces were grounded with SiC papers, polished with a diamond paste and, finally, chemically etched by polishing for 2 h. For the chemical etching, a suspension consisting of 60 ml of OP-S colloidal suspension (Struers), 0.3 g of dissolved potassium hydroxide and 440 ml of deionized water was used. The final thicknesses of the as-prepared samples were ~150 μm.

The PFM and c-AFM images were recorded using an atomic force microscope (AFM, Asylum Research, Molecular Force Probe 3D, Santa Barbara, CA, USA). A tetrahedral Si tip on a Si cantilever, both coated with Ti/Ir (Asyelec, AtomicForce F&E GmbH), was used. Out-of-plane PFM images were obtained in Dual AC Resonance Tracking (DART) mode using 8 V of AC voltage at the tip. The c-AFM experiments were conducted in ORCA mode by applying a DC voltage between the tip and a bottom electrode. A range of DC voltages (from 9 to 32 V) was used for the c-AFM imaging. The c-AFM images shown in Figure 4.18, were obtained by applying 10 V DC. In all cases, the scanning frequency was 0.8 Hz with 256 of scan points per individual line. A periodic electrical noise in the c-AFM images, observed as streaks in the background, was removed by applying a magnitude space where the noise was manually removed. After the noise removal, the image was transformed back to the spatial domain.

Note that for statistical purposes, we defined a single GB as the boundary surrounding one individual grain. This means that, in the case when a part or more parts of one GB was found to be conductive, the whole GB was considered as conductive and all the neighboring grains were excluded from further analysis. On the other hand, we defined a single DW as the boundary separating two neighboring domains.

3.2.6 Macroscopic electrical and electromechanical properties

3.2.6.1 Room-temperature measurements

Sample preparation for dielectric, ferroelectric and electrical conductivity measurements was performed with the following procedure. The samples were cut from the sintered pellets using a diamond wire saw and ground on both sides using SiC grinding paper with the

degradation 1200 to a thickness between 0.2 and 0.3 mm. Afterwards, the samples were sputtered with Au electrodes using a circular mask with a diameter of 5 mm (Cinquepascal SRL, Trezzano, Italy).

Dielectric measurements were performed using a 4284A precision LCR meter (Hewlett Packard, Tokyo, Japan) in the frequency range 10^6-10^2 Hz, while the measurements in the low-frequency range 10^3-10^{-2} Hz were performed with a charge amplifier (Type 5018, Kistler, Winterthur, Switzerland) coupled with a lock-in amplifier (model SR830 DSP, Stanford Research System, Sunnyvale, California) to measure the first harmonic charge response. The lock-in amplifier was also used as a voltage source. The driving field amplitude was 0.02 kV cm^{-1}.

Current-density-electric-field (*j*-*E*) response was measured using a Keithley 237 (Keithley Instruments, Ohio, USA) high-voltage source measure unit. The samples were exposed to step-like voltages within the range ±0.02 kV cm^{-1}. In this range, from negative to positive polarity, 11 field steps were applied. Upon each step, the voltage was maintained constant for 1 h for the current to stabilize, before being recorded (the time-stabilized current is represented as the leakage current). The specific DC electrical conductivity (σ_{DC}) was determined from the *j*-*E* curves as the curve slope (Ohmic behavior).

The **high-field polarization versus electric field (*P*-*E*) hysteresis loops** were measured using a TF analyzer 2000 (aixACCT Systems GmbH, Aachen, Germany) coupled with a high-voltage amplifier (Model 609E-6, TREK Inc., Lockport, New York, USA). The samples were immersed in silicone oil and the hysteresis loops were recorded by applying single sinusoidal waveforms at 100 Hz and selected electric field amplitudes to the samples.

Samples for **piezoelectric measurements** (under resonance and off-resonance conditions) were poled in a silicone-oil bath at RT under a DC field. The poling conditions (given in Table 3.4) were selected considering the E_c and breakdown strength of a specific Co-doped BFO composition with the aim to obtain a comparable d_{33} value for all compositions.

In terms of the **resonance measurements**, the electromechanical quality factor Q_m and planar coupling coefficient k_p were determined using the BODE 100 vector network analyzer and the IEEE-resonance method [114]. The Q_m values were evaluated as [115]

$$Q_m = \frac{1}{2\pi f_r |Z| C^T k_{eff}^2} \tag{3.4}$$

where f_r corresponds to the resonance frequency, $|Z|$ is the impedance value at the resonance frequency, C^T is the off-resonance free capacity (taken at 1 kHz) and k_{eff} is the effective coupling coefficient determined as

$$k_{eff}^2 = \frac{f_a^2 - f_r^2}{f_a^2} \tag{3.5}$$

where f_a corresponds to the anti-resonance frequency. The k_p values were evaluated as

$$k_p = \left[2{,}51 \frac{f_a - f_r}{f_r} - \left(\frac{f_a - f_r}{f_r}\right)^2 \right]^{1/2} \tag{3.6}$$

Direct d_{33} coefficients were measured using a standard Berlincourt piezometer (Take Control PM10, Birmingham, UK) operated at a frequency of 110 Hz. The **converse piezoelectric measurements** were performed using a home-made setup composed of a fiber-optic displacement sensor (MTI 2100), a low-distortion voltage generator (SRS

DS360), a voltage amplifier (Trek 609E-6), an oscilloscope (LeCroy 9310C), and two lock-in amplifiers (SR80 DSP) to precisely measure the harmonic signals of the input voltage and output displacement response. The measurements were carried out at room temperature in the frequency range between 90 and 0.1 Hz. At each frequency, the piezoelectric response was measured as a function of the increasing external electric field amplitude from 3.5 kV cm^{-1} up to a maximum of 16 kV cm^{-1} with individual increments of 2.5 kV cm^{-1}. The d_{33} value was calculated as $\Delta L/V_0$, where ΔL and V_0 are the amplitudes of the output displacement and input voltage, respectively, and δ is the phase angle between the displacement and voltage signals. The values of ΔL, V_0 and δ were directly measured using the lock-in technique.

Table 3.4: Conditions for DC poling of Co-doped BFO ceramic samples used for resonance and converse piezoelectric measurements.

Composition	Poling conditions for resonance measurements (field, time)	Poling conditions for converse piezoelectric measurements (field, time)
0.25 Co	70 kV cm^{-1}, 15 min	90 kV cm^{-1}, 10 min
0.5 Co	75 kV cm^{-1}, 15 min	90 kV cm^{-1}, 15 min
1.0 Co	90 kV cm^{-1}, 15 min	95 kV cm^{-1}, 20 min
1.5 Co	95 kV cm^{-1}, 15 min	100 kV cm^{-1}, 40 min

3.2.6.2 Temperature- and atmosphere-dependent conductivity, thermoelectric (Seebeck coefficient) and dielectric measurements

Electrical conductivity as a function of temperature in different flowing gases (N_2, O_2) was measured **using a direct current (DC) four-point method**, as previously reported by Wærnhus *et al.* [116]. The measurements were performed on sintered bars with dimensions of about 15×4×4 mm^3. A constant voltage of 1.5 V (GW Instek GPS3030DD) was applied over the sample. The resulting voltage drop and current across the sample were measured by the voltage electrodes (placed 5 mm apart) and current electrodes, both connected to Keithley 2000 multimeters. The temperature was controlled by an S-type thermocouple. The DC electrical conductivity measurements were provided during annealing the samples in three consecutive cycles. The samples were annealed from RT to 700 °C with zero holding time and with a heating and cooling rate of 2 °C min^{-1} first in a flow of O_2 (Linde, 5.0), afterwards in N_2 (Linde, 5.0) and finally again in O_2.

The **Seebeck coefficient** (S) was measured on ceramic bars analogous to those used for DC conductivity measurements. The measurements were made using a ProboStat™ setup (NorECs AS, Norway), covered by an alumina tube. The setup was placed inside a vertical tubular furnace where the middle thermocouple was connected to the temperature controller. The top and bottom thermocouple (S-type) and electrodes (Pt) were connected to the sample, and monitored with Omega software (NorECs AS, Norway) via a Keithley 2000 multimeter. The Seebeck-coefficient measurements were made during annealing the samples in three consecutive cycles. The samples were annealed from RT to 700 °C with zero holding time and with a heating/cooling rate of 2 °C min^{-1} first in a flow of synthetic air (Linde, 5.0), afterwards in N_2 (Linde, 5.0) and finally again in synthetic air.

Ceramic samples for **dielectric measurements** as a function of temperature and the partial pressure of oxygen were ground down to ~3 mm and covered with a gold paste and annealed at 750 °C with 1 h holding time in order to consolidate the electrode. The measurements were performed using a frequency analyzer (Alpha-A High Performance

Frequency Analyser, Novocontrol Technologies, Germany), connected to a ProboStat™ setup in a vertical tubular furnace. The measurements were performed at a frequency of 1 Hz during continuous heating and cooling in synthetic air and N_2, following the same program as in the case of the DC electrical conductivity measurements and Seebeck-coefficient measurements described above.

3.2.7 Electron paramagnetic resonance

The X-band (9.5 GHz) electron paramagnetic resonance (EPR) measurements were performed on a home-built spectrometer using a Varian double cavity. The EPR spectra were recorded in the temperature range from room temperature up to 400 °C using a preheated-nitrogen-flow heating system with temperature stabilization. Powder samples were prepared by crushing the sintered pellets and were sealed in quartz tubes under vacuum. The principal values of the g factor tensor were obtained after simulating the recorder derivative EPR spectra with home-made software, assuming isotropic powder averaging and Lorentzian line-shape. The relationship $h\nu = g\mu_B B$ was used, where h is Planck's constant, ν is the operating frequency, μ_B is the Bohr magneton and B is the magnetic field strength.

3.3 Density Functional Theory

3.3.1 General considerations

All density functional theory (DFT) calculations were performed with the Vienna *Ab-initio* Simulation Package (VASP, version 5.4.4) [117], [118] using the projector-augmented wave (PAW) method [119]. The pseudopotentials used in this work are Bi_d ($5d^{10}6s^26p^3$), Fe_pv ($3p^63d^74s^1$), Co_sv ($3s^23p^63d^84s^1$) and standard O ($2s^2p^4$) [118] supplied with VASP.

The Brillouin zone integration was made with a gamma-centered k-point grid. For the trigonal BFO unit cell with 30 atoms, a k-point density of $6 \times 6 \times 3$ was used, with corresponding k-point densities for larger cell sizes, i.e., $3 \times 3 \times 3$ for the 120-atom supercells. All calculations in this work were made with an energy cutoff (E_{cut}) of 550 eV, for which convergence was reached.

All calculations were performed using the PBEsol functional [120], an exchange-correlation functional especially developed for solids. The implementation of the Hubbard-U correction introduced by Dudarev *et al.* [121] was used with U = 4 eV on the Fe $3d$ and Co $3d$ states to reproduce the experimental electronic band gap of BFO [122], [123]. The magnetic ordering of the Fe sublattice was initialized with G-type collinear antiferromagnetic ordering in concordance with the magnetic order of bulk BFO [124]. The magnetic moments on the Fe and Co atoms were initially set to 5 and 4 μ_B, respectively.

3.3.2 Crystal structure and geometry optimization

Optimizations of the crystal structures were performed by relaxing the atomic positions and lattice parameters until the Hellmann-Feynman forces [125] acting on all the ions were below a certain threshold. For the 30-atom supercells a force-based convergence criterion of 0.01 eV $Å^{-1}$ was used, while 0.03 eV $Å^{-1}$ was used for the 120-atom supercells. The charge-density optimization for each ionic step was performed until the total energy differences between two subsequent electronic steps were below a set threshold of 10^{-8} eV.

The lattice parameters and atomic positions of the BFO were initialized in the hexagonal setting of the trigonal space group R3c, as reported in ref. [126]. Full relaxation of the atomic positions, cell volume and cell shape for stoichiometric BFO was performed. The ionically converged structure was obtained by repeating the relaxation until convergence in one ionic step to avoid Pulay stresses [127].

Calculations on Co-doped BFO (BFCO) and all geometry optimization of defect cells with V_{Bi}''' and $V_O^{\bullet\bullet}$, were performed with fixed cell volumes and shapes from the resulting stoichiometric BFO supercell. For BFCO, one Fe atom was replaced by Co in a fully relaxed 120-atoms BFO supercell, giving a formula $Bi_{24}Fe_{23}CoO_{72}$, i.e., $Bi(Fe_{0.958}Co_{0.042})O_3$. In the case of defect cells, one V_{Bi}''' or $V_O^{\bullet\bullet}$ was introduced, with the resulting stoichiometry $Bi_{0.958}FeO_3$ ($Bi_{0.958}(Fe0_{.958}Co_{0.042})O_3$) and $BiFeO_{2.958}$ ($Bi(Fe_{0.958}Co_{0.042})O_{2.958}$).

3.3.3 Electronic properties

The electronic properties and charge-compensation mechanisms were determined from the electronic density of states (DOS), Bader charges and iron/cobalt magnetic moments. Atomic charges were calculated using a Bader charge analysis [128], where the charge enclosed within a zero flux surface surrounding an atom, or Bader volume, is used to determine the total charge of the atom.

3.3.4 Defect formation energy

The formation energy (E_{def}^f) of neutral defects was calculated as

$$E_{def}^f = E_{defect}^f - E_{ref}^f - n_{def}\mu_{def} \tag{3.7}$$

where E_{defect}^f is the total energy for the defect cell investigated and E_{ref}^f is the total energy for the reference system in which the defect is introduced. n_{def} and μ_{def} are the number and chemical potential of a defect introduced to the system, relative to the chosen reference state. The chemical potentials of Bi and O used for calculation of E_{def}^f in oxygen-rich conditions are -7.54 eV and -5.41 eV, respectively [129].

Chapter 4

Results and Discussion

4.1 Structure, Microstructure, Phase Composition and Dopant Incorporation in Co-Doped BFO Ceramics

4.1.1 Structural analysis

The normalized diffraction patterns of BFO ceramics with 0.0, 0.25, 0.5, 1.0 and 1.5 at.% of Co are shown in Figure 4.1. The primary phase in all the compositions can be described with the crystallographic card of the rhombohedral $BiFeO_3$ (JCPDS Card No. 86-1518; space group *R3c*). However, an extra peak with low intensity can be observed at 2θ=28°, appearing just above the background signal, which can be attributed to the $Bi_{25}FeO_{40}$ secondary (sillenite) phase (denoted by * in the inset). The intensity of this peak is similar in all the compositions, meaning that the amount of sillenite phase is comparable for the different samples. This was confirmed quantitatively by Rietveld refinements of the XRD patterns displayed here, which showed that the amount of the sillenite phase in all the samples does not exceed ~1 wt%.

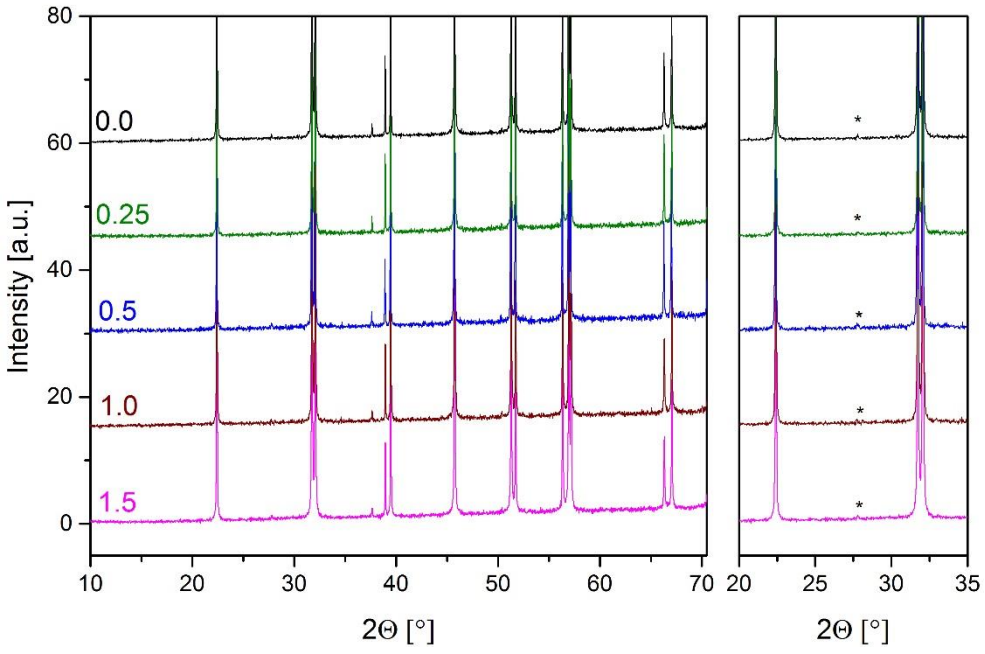

Figure 4.1: XRD patterns of BFO ceramics doped with 0.0, 0.25, 0.5, 1.0 and 1.5 at.% Co. The inset shows an enlarged part of the pattern, highlighting the weak peak of the secondary phase, appearing just above the background signal (*=sillenite phase, $Bi_{25}FeO_{40}$).

4.1.2 Microstructural analysis

The microstructures of undoped and Co-doped BFO ceramics were examined by scanning electron microscope (SEM). The backscattered electron (BSE) images of the undoped and doped samples are shown in Figure 4.2.

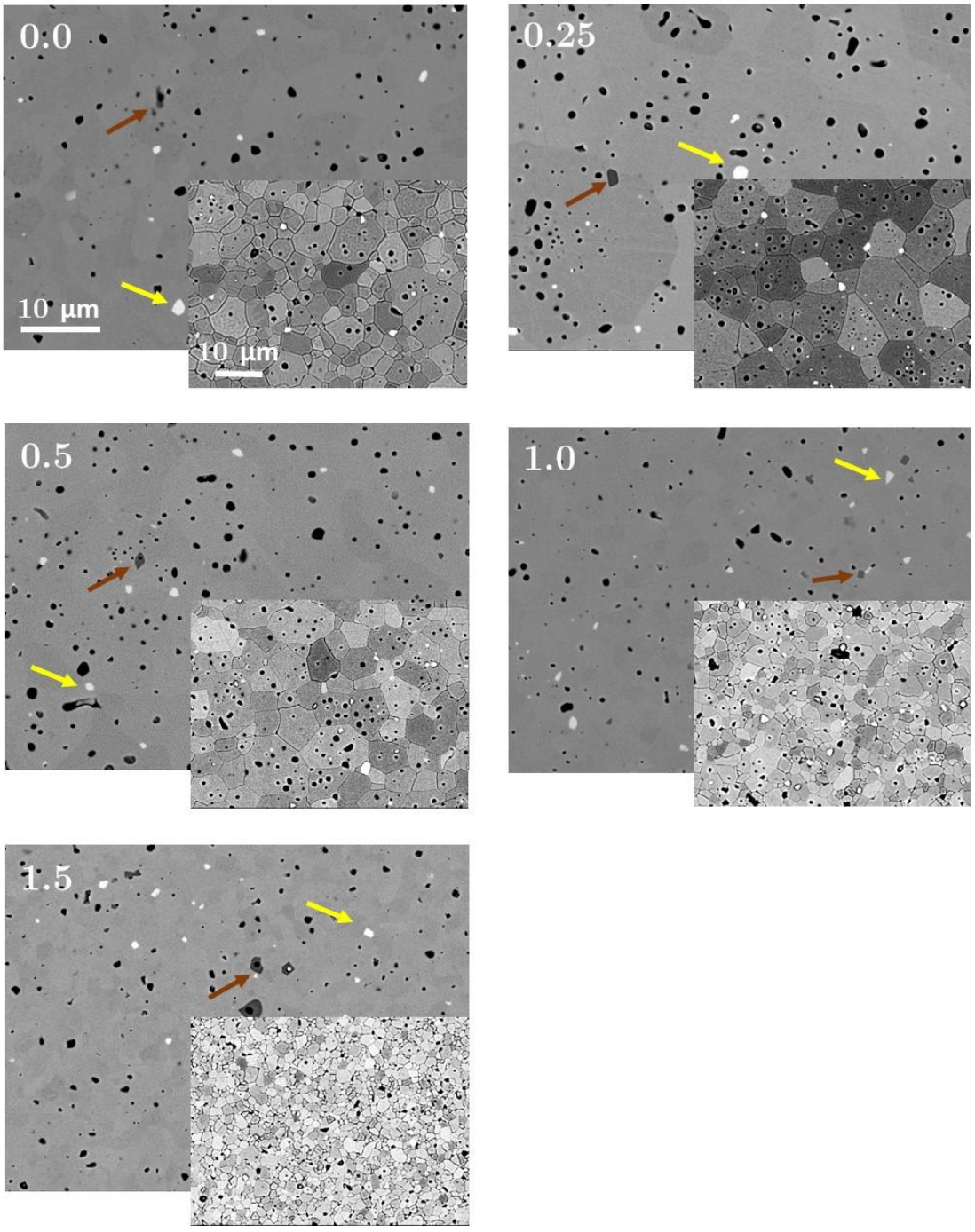

Figure 4.2: BSE-SEM micrographs of polished and thermally etched (shown as inset) undoped and Co-doped BFO ceramics. The scale bars of the SEM images are shown for undoped BFO and correspond to all the compositions. The yellow and brown arrows denote sillenite and mullite phase, respectively, while the black regions are pores.

All the compositions exhibit a relatively dense microstructure, which is in agreement with the measured relative densities (94.5-97.0%) collected in Table 4.1. However, clearly some secondary phases are present, such as those marked with yellow (sillenite phase, $Bi_{25}FeO_{40}$) and brown (mullite phase, $Bi_2Fe_4O_9$) arrows, which is to be expected considering the known difficulties in preparing single-phase BFO for thermodynamic and kinetic reasons [104], [105]. Nevertheless, no distinct differences in the amounts of secondary phases between the different compositions can be observed.

Table 4.1: Relative densities and grain sizes of BFO ceramics with different concentrations of Co dopant.

Co concentration [at.%]	Relative density [%]	Grain size [µm]
0.0	97.0%	3.4±1.9
0.25	94.5%	8.2±4.4
0.5	95.0%	5.7±3.1
1.0	96.0%	2.0±1.1
1.5	97.0%	1.2±0.5

As it can be observed from the micrographs of thermally etched ceramics (see, e.g., undoped BFO), the pores are trapped inside grains indicating very fast grain growth, where the pores are left behind by rapidly moving grain boundaries. In general, the grain growth kinetics strongly depends on the impurity concentration as already a small amount can drastically change the type and concentration of defects and influence the mobility of the grain boundaries [130]. Intragranular pores are predominantly present in samples with none (undoped) or a low concentration of Co (0.25, 0.5%), while they are less pronounced in samples with 1 and 1.5% Co where the GS is notably smaller. This indicates that Co incorporation reduces the grain-boundary mobility (samples with 1 and 1.5% Co are in fact characterized by smaller grains and less intergranular porosity). Finally, the GS clearly decreases by increasing the concentration of Co roughly from 8 μm (0.25% Co) to 1 μm (1.5% Co). Interestingly, undoped BFO has a grain size smaller than those doped with 0.25% Co (Table 4.1) so that the maximum grain size is observed with 0.25% Co.

Similar observations on increasing GS at low dopant concentrations (≤ 0.4 at.%) and an abrupt decrease of GS at higher (≥ 1.0 at.%) dopant concentrations have been reported in La-doped PZT ceramics [131]. The authors consider the idea that a small dopant concentration leads to the formation of cation vacancies, thereby increasing the bulk diffusion and growth of large grains. Furthermore, they assumed that at higher dopant concentrations, the grain growth and thus the grain size is governed by an impurity-drag mechanism. Nevertheless, no experimental evidence to support this interpretation has been provided.

On the other hand, the inhibited grain growth through the addition of dopants is a very common observation in BFO [76], [81], [84], [132] as well as in other ceramic systems [133]–[135]. The two mechanisms by which the grain growth could be inhibited are the pinning effect and the solute-drag effect. The pinning effect occurs when small particles of secondary phase are pinned onto the grain boundaries, thereby restricting the diffusion processes that cause grain growth. On the other hand, the solute-drag effect occurs when the dopant segregates at grain boundaries because of the low solubility in the host structure, slowing down the diffusion processes and consequently resulting in inhibited grain growth [136]. Another factor that could decrease the mobility of the grain boundaries is grain (mis)orientation, as reported in, e.g., Sr-doped $(K_{0.5}Na_{0.5})NbO_3$ ceramics [133]. It

was found that at higher dopant concentrations (~>6%), the increasing A-site cation disorder results in sub-grains with a size of the order of tens of nm, which are divided from each other by low-angle grain boundaries, with a strongly limited grain-boundary mobility.

Furthermore, in the case of aliovalent doping, such as with Co^{2+} ions (this is explained later in Chapter 4.2), defects will be formed in order to maintain the charge neutrality condition. These defects may also strongly affect the grain growth [84], [132]. Nevertheless, the possible origin of inhibited grain growth in BFO ceramics by Co introduction will be discussed hereafter.

4.1.3 Chemical analysis on the atomic scale

In order to get an insight into the possible segregation of secondary phases (e.g., liquid phase potentially arising from the melting of the sillenite phase) or the Co dopant at the grain boundaries and evaluate whether this is the origin of the inhibited grain growth in compositions with higher Co concentration, the 1.5 at.% Co-doped BFO sample was analyzed using Scanning Transmission Electron Microscopy (STEM) and Electron-Energy-Loss Spectroscopy (EELS). In Figure 4.3, a high-angle annular dark-field (HAADF) STEM image is shown with an identified grain boundary (GB). The dopant segregation at the grain boundary was evaluated by performing EELS analysis across the GB (dashed box). By inspecting the Co-L_3 edge in the EELS spectra (at ~780 eV), no peak enhancement can be observed indicating there is no Co segregation at the GBs or, alternatively, it is below the limit of detection (~1-2%). Furthermore, no secondary phases can be observed at the GBs, therefore, it can be concluded that the GBs are clean.

Considering these results, we can conclude that the inhibited grain growth by Co introduction is not associated with segregation of a dopant or a secondary phase at the GBs. Moreover, as no nanograins were found by STEM analysis, we can infer the possibility of inhibited grain growth due to effect of point defects [84], [132] rather than grain orientation (as mentioned above) [133], [136].

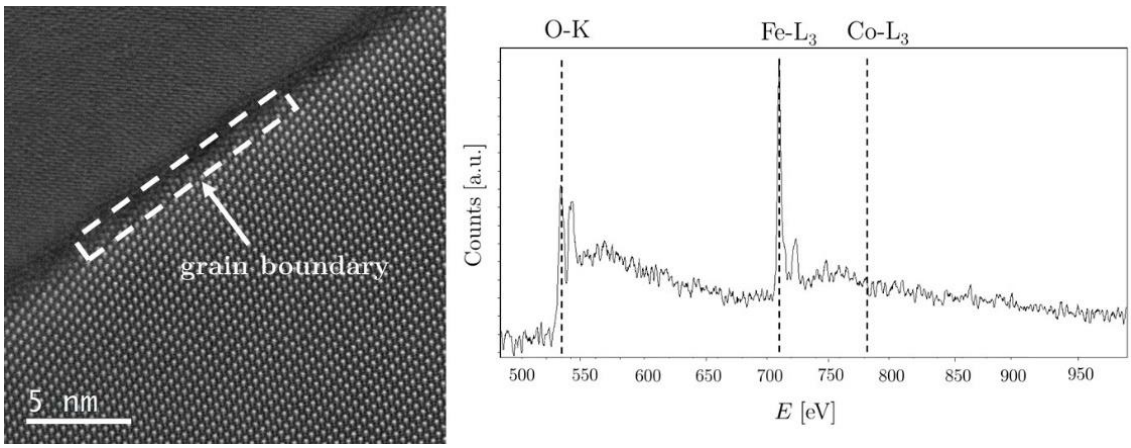

Figure 4.3: HAADF-STEM image showing a grain boundary in BFO doped with 1.5 %Co and adjacent EELS spectrum acquired across the grain boundary (dashed box). Dashed lines denote the positions of the O-K, Fe-L_3 and Co-L_3 edges.

4.1.4 Summary

To sum up, XRD and SEM analyses of undoped and Co-doped BFO ceramics revealed that the ceramics contain a small concentration (<1 wt.%) of secondary phases (Figure 4.1, Figure 4.2). This could potentially result in sub-stoichiometric BFO ceramics, and thus influence the electrical conductivity and ferroelectric hardening of the ceramics. However, we note that a comparable concentration of secondary phases in these samples still allows us to evaluate the effect of the dopant. In addition, we found that Co incorporation into the perovskite affects the grain growth, which could possibly be associated with a change in diffusivity due to the doping-related point defects [130]. This is because no dopant or secondary-phase segregation was found by STEM/EELS analysis on the grain boundaries (Figure 4.3). Although the different grain sizes depending on the Co concentration are taken into account when interpreting the macroscopic properties presented in subsequent chapters, strong grain-size effects on properties are not expected for grain sizes bigger than ~1 μm (see Table 4.1.), as suggested by studies on PZT or BT [137], [138].

4.2 Control of Hardening in Co-Doped BFO Ceramics

4.2.1 Influence of Co concentration

Prior to presenting the results on the influence of Co concentration on ferroelectric hardening and electrical conductivity in BFO ceramics, it should be noted that undoped BFO showed high losses observed as a rounded shape of the *P-E* loop. For this reason, undoped BFO was not included in the comparative study on the influence of Co concentration; nevertheless, some key results are presented in Appendix A.1.

4.2.1.1 Domain switching

Polarization-electric field (*P-E*) loops of BFO ceramics with 0.25, 0.5, 1.0 and 1.5 at.% of Co, measured at 100 kV cm^{-1}, are displayed in Figure 4.4. All the loops exhibit a pinched and biased shape, typical for BFO ceramics [47], [87], [89]. This behavior has been previously discussed in terms of DW pinning mediated by charged point defects [62], [89]. It can be observed that the pinching of the *P-E* loop increases as the content of Co increases (indicated with the arrow in Figure 4.4a). Moreover, the applied electric field of 100 kV cm^{-1} is insufficient for the domain switching in 1 and 1.5 at.% Co-doped sample, evidenced by the underdeveloped *P-E* loops. The *P-E* loops of these two samples eventually develop the shape characteristic for domain switching by applying a higher electric field of 130 kV cm^{-1} (Figure 4.4b). Also in this case, it is clear that the pinching increases with Co concentration (see arrow in Figure 4.4b).

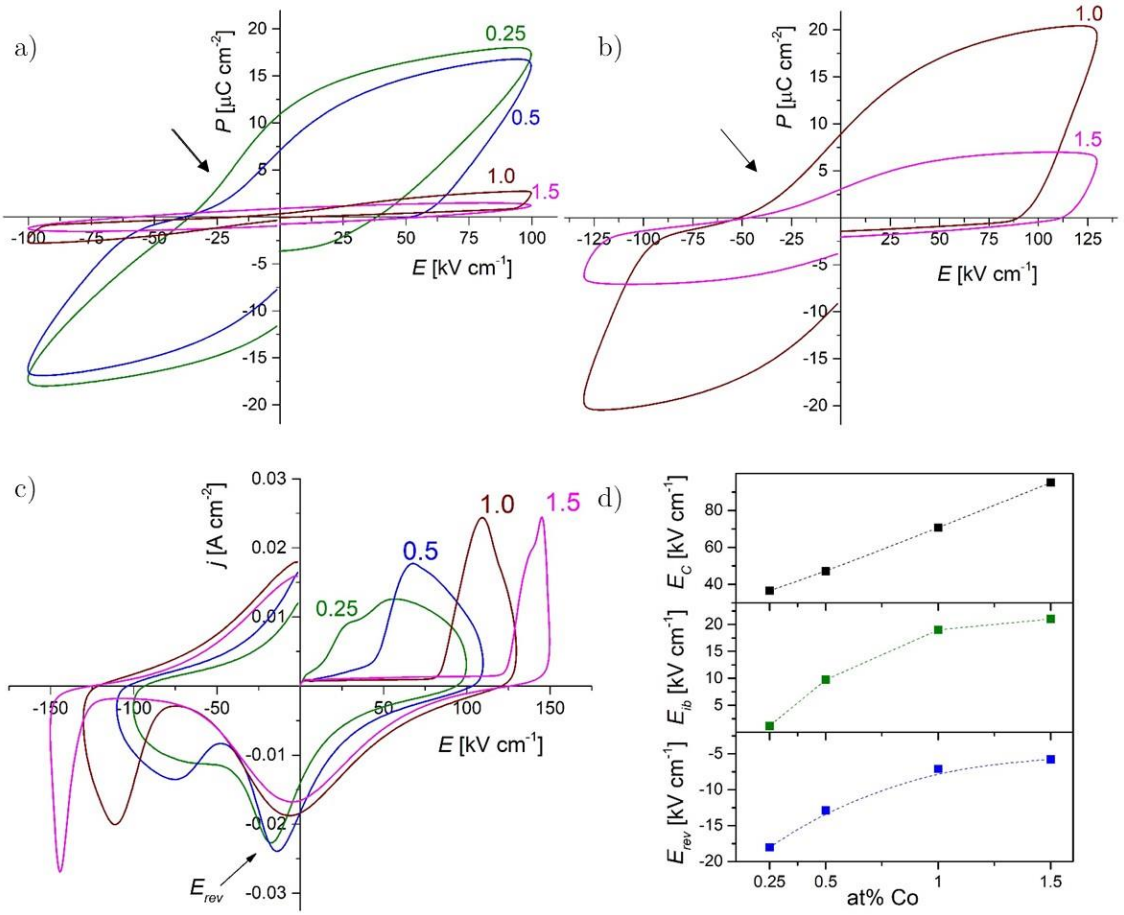

Figure 4.4: Ferroelectric properties of Co-doped BFO ceramics. *P*-*E* hysteresis loops of BFO ceramics with a) 0.25, 0.5, 1.0 and 1.5 at.% of Co measured at 100 kV cm^{-1} and b) with 1 and 1.5 at.% of Co measured at 130 kV cm^{-1}. c) *j*-*E* hysteresis loops of Co-doped BFO ceramics; the arrow indicates the electric field that corresponds to E_{rev}. d) Compositional dependence of E_c, E_{ib} and E_{rev}.

Current density vs. electric field (*j*-*E*) loops of all the Co-doped compositions are shown in Figure 4.4c. The displayed loops were measured at different electric field amplitudes, i.e., 100 kV cm^{-1} (0.25 Co), 110 kV cm^{-1} (0.5 Co), 130 kV cm^{-1} (1.0 Co) and 150 kV cm^{-1} (1.5 Co) due to the different coercive field and breakdown field for the different compositions. Considering these conditions, the coercive field (E_c), internal bias (E_{ib}) and reverse electric field (E_{rev}) as a function of the Co concentration were determined, and the results are presented in Figure 4.4d. As explained in the following, these three parameters were chosen because they are very sensitive to hardening effects and can therefore give a clear indication about the pinning of DWs mediated by charged point defects [4], [15], [17].

E_{ib} is evidenced as a shift of the *P*-*E* loop along the *E*-axis as a consequence of defect orientation and its interaction with the applied electric field (see Chapter 1.1.2 and equation (1.3)). E_{rev} corresponds to the field of the current-density peak observed after the main switching event when reversing the field polarity from positive to negative (see arrow in Figure 4.4c). This current-density peak and the associated E_{rev} reflect the back-switching of domains, provoked by the defect-mediated pinning [17], [139]; this means that the higher E_{rev} (i.e., the more the peak is closer to zero field), the stronger the back-switching, and thus the pinning effects. Finally, the average coercive field E_c is also expected to increase as the pinning effects become stronger [4], [17]. As it can be observed

in Figure 4.4d, all three parameters, i.e., E_c, E_{ib} and E_{rev}, clearly increase with increasing Co concentration. These results suggest an increasing hardening effect with increasing acceptor dopant concentration, similar to that observed in acceptor (Fe)-doped PZT [17].

4.2.1.2 Electrical conductivity

Figure 4.5 shows the real (ε') and imaginary (ε'') parts of the dielectric permittivity and the real part of the electrical conductivity (σ') as a function of frequency (ω) for Co-doped ceramics. The significant increase in ε'' (>1 Hz) at low frequencies in all samples (Figure 4.5b; note the logarithmic scale) implies that the dielectric response at low frequencies is dominated by the electrical conduction. However, the dispersion of both ε' and ε''at low frequencies indicates that the conduction processes not only dissipate energy but also contribute to the dielectric polarization of the material, which could be attributed to Maxwell-Wagner-like (M-W) and/or hopping conductivity mechanisms [44], [48], [140]. In addition, except for the 0.25 Co sample, all the samples show small relaxation-like features in the ε' curves (Figure 4.5a). As can be observed from the frequency dependence of σ' in Figure 4.5c, all four compositions exhibit a clear plateau at low frequencies (see dashed lines). From the frequency-dependent σ', it is possible to estimate the specific electrical DC conductivity (σ_{DC}) using equation 4.1, which is derived by assuming a leaky capacitor with losses composed of the dielectric loss and the electrical conductivity loss:

$$\sigma' = \sigma_{DC} + \omega\varepsilon_0\varepsilon_d'' \tag{4.1}$$

where ε_d'' is the imaginary dielectric permittivity related to the polarization losses and ε_0 is the permittivity of vacuum. Providing ε_d'' is low, the equation shows that at low frequencies, the term $\omega\varepsilon_0\varepsilon_d''$ becomes exceedingly small and the σ' eventually reaches a plateau at the low-frequency limit corresponding to σ_{DC}, which can thus be estimated as σ'~σ_{DC}. Thus, the DC conductivity, set by the plateau of σ' at low frequencies (see dashed lines in Figure 4.5c), clearly increases with increasing concentration of Co. σ' of the 0.25 Co still shows frequency dependence and would probably level off only at lower frequencies than those used for the measurements (due to the comparably low σ_{DC}; see equation 4.1). Assuming this, we can estimate the σ_{DC} as $< \sim 5.0 \times 10^{-11}$ $\Omega^{-1}m^{-1}$ for this composition. By extrapolating the plateau of σ' (or the onset of the plateau in the case of 0.25 Co) at low frequencies, it can be inferred that the value of σ_{DC} spans from $\sim 5.0 \times 10^{-11}$ (0.25 Co) to $\sim 4.5 \times 10^{-7}$ $\Omega^{-1}m^{-1}$ (1.5 Co), thus showing an almost 4-orders-of-magnitude difference within the entire doping range (see estimated values of σ_{DC} in Figure 4.5c). These σ_{DC} values are in a reasonable agreement with those determined from static current density vs. electric field (j-E) measurements (see σ_{DC} values in Figure 4.5d and its inset), confirming the increasing trend of σ_{DC} with increasing Co concentration. Note that the j-E measurements were performed by applying both positive and negative field polarities, though, for clarity, the data are shown only for positive electric fields.

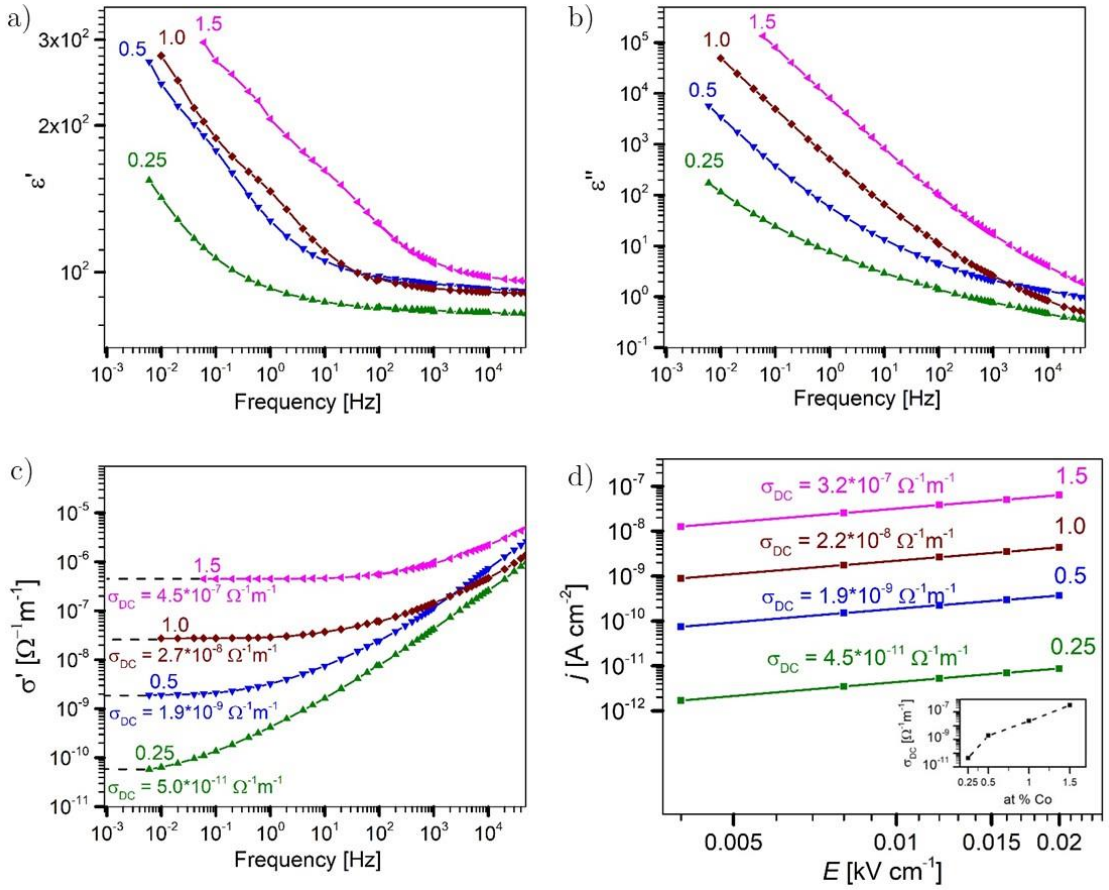

Figure 4.5: a) The real (ε') and b) imaginary (ε'') components of the dielectric permittivity and c) the real part of the electrical conductivity (σ') as a function of driving-field frequency for Co-doped BFO ceramics. In panel d) the j-E curves for positive electric fields are displayed for Co-doped BFO ceramics. The inset shows the log-linear plot of σ_{DC} as a function of Co concentration. The dashed line between the experimental points is drawn as a guide to the eye.

Several reported experimental and theoretical studies [49], [52], [65], [66], [74], [141] demonstrate that BFO-based ceramics exhibit p-type conductivity (associated with the presence Fe^{4+} oxidation states, i.e., trapped electron holes at Fe sites), when sintered in air (Chapter 1.2.1). In line with the defect chemistry model [49], explained in detail in chapter 1.2.1, the increase of electrical conductivity in the range 0.25-1.5 at.% Co (see Figure 4.5) could be explained with an increase in the concentration of electron holes (Fe^{4+}). Therefore, these results indicate that Co acts as acceptor dopant according to the defect reaction in equation (4.2) where the Co^{2+} acceptor substituting on the Fe^{3+} site in BFO is proposed to be charge compensated by oxygen vacancies ($V_O^{\bullet\bullet}$):

$$CoO + Fe_{Fe}^{x} + \frac{1}{2}O_O^{x} \rightarrow \frac{1}{2}Fe_2O_3 + Co'_{Fe} + \frac{1}{2}V_O^{\bullet\bullet} \tag{4.2}$$

Considering that the concentration of $V_O^{\bullet\bullet}$ is closely related to the valence state of Fe through equation (1.6), increasing the $V_O^{\bullet\bullet}$ concentration by Co doping will shift equation (1.6) towards the right side, resulting in more Fe^{4+}, which thus enhances the p-type conductivity. This is in agreement with the synchrotron XAS study on Co-doped BFO

ceramics, which confirmed the presence of Fe^{4+} states induced by Co doping [68]. Moreover, this is also in agreement with a recent photoelectron spectroscopy study on Co-doped BFO thin films, which revealed that Co is mostly in the 2+ oxidation state [142].

Using similar reasoning as for the electrical conductivity trend with respect to the dopant concentration, the increase of the hysteresis pinching and biasing with increasing Co concentration (Figure 4.4) could be attributed to the increased concentration of defects, i.e., $V_O^{\bullet\bullet}$ and $Fe_{Fe}^{\bullet}$. Both types of defects can, in fact, act as pinning centers for the domain walls, restricting their motion and thus resulting in impeded polarization switching as indicated in Figure 4.4. The question is though whether and which defects are dominant in the pinning behavior.

4.2.1.3 Piezoelectric response

In this chapter we present the results of the resonance measurements of the different Co-doped samples. From Figure 4.6 it can be observed that Q_m increases steadily, while k_p decreases first abruptly (from 0.25 to 0.5 % Co) and then less dramatically with increasing Co concentration. The value of Q_m is the reciprocal of the mechanical losses, which are in piezoelectric ceramics strongly affected by DW dynamics [143]. The increase of Q_m and thus the decrease of mechanical losses is commonly attributed to DW-pinning and/or lattice stiffness effects [9]. Therefore, the Q_m trend strongly suggests that the DW-pinning effects increase with increasing Co concentration, which is in agreement with pinching of P-E loops in Figure 4.4a. In addition, several studies showed that Q_m and E_{ib} are correlated [144], which can be observed also in Co-doped BFO ceramics (see trend of E_{ib} in Figure 4.4d).

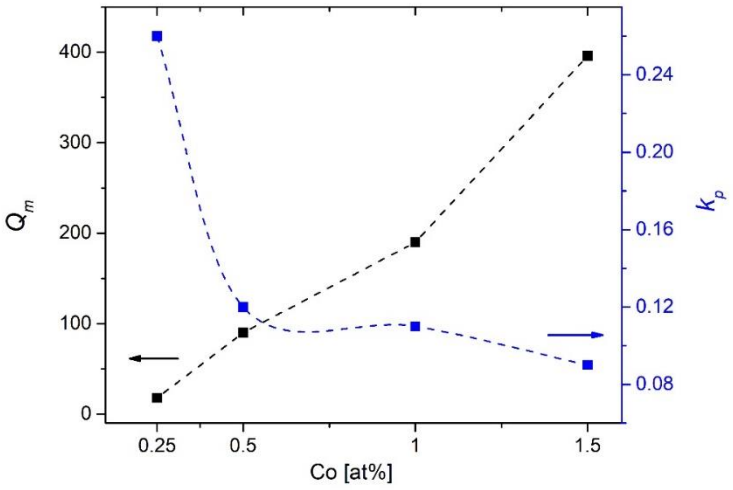

Figure 4.6: The electromechanical quality factor (Q_m) and planar quality factor (k_p) as a function of Co concentration. The dashed lines between the experimental points are drawn as guide to the eye.

The decrease of k_p, which defines the ability of the material to convert electrical energy into mechanical and vice versa, with increased Co concentration (and thus increased hardening) is expected. Namely, lower DW mobility leads to lower efficiency, resulting in

lower k_p. These results are consistent with the observations from a number of lead-based and lead-free materials [144], [145].

It should be pointed out that Q_m (and k_p) can be affected by GS either due to the different domain structure and/or due to the contribution of grain boundaries acting as pinning centers [138], [146]. The observation of Q_m in Figure 4.6 and the GSs of the measured samples (summarized in Table 4.2) show that Q_m increases as the GS decreases. In order to distinguish between the GS and the hardening effect, the following experiment was performed.

The GS of the 0.25 Co composition was reduced to 5.5 μm by reducing the sintering time from 4 h to 1 h. In terms of GS, this 0.25 Co sample was thus comparable to the 0.5 Co (with the GS of 5.7 μm). Both samples were poled to comparable d_{33} (22 pC N^{-1}). The Q_m of 0.25 Co BFO was found to be 25, which is still significantly lower that the Q_m of the 0.5 Co sample (Q_m=90) despite the similar GS. These results (summarized in Table 4.2) suggest that the increase of Q_m with Co concentration is predominantly due to the hardening effect rather than the GS effect. Nevertheless, it is not excluded that the GS effect could have some minor contribution in 1.5 Co as the GS is close to 1 μm [137], [138].

Table 4.2: Summarized grain sizes, direct d_{33} coefficients, electromechanical quality factors (Q_m) and planar coupling factor (k_p) of Co-doped BFO ceramics. Label 0.25 (1 h) refers to sample where the sintering time was reduced from 4 h to 1 h in order to decrease the GS.

Co concentration [at.%]	Grain size [µm]	d_{33} [pC N^{-1}]	Q_m [/]	k_p [/]
0.25	8.2	21	18	0.26
0.5	5.7	20	90	0.12
1.0	2.0	23	190	0.11
1.5	1.2	22	396	0.09
0.25 (1 h)	5.5	22	25	0.21

4.2.1.4 Summary and next steps

The electrical conductivity, ferroelectric hysteresis loops and piezoelectric response under resonance conditions have been measured for different Co concentrations. It has been found that the electrical conductivity and hardening, as observed from the domain-switching behavior and piezoelectric properties, increases with Co concentration, which has been attributed to increased concentration of $V_O^{\bullet\bullet}$ and $Fe_{Fe}^{\bullet}$.

In order to further evaluate whether and which of these defects dominate the effect of pinching and conductivity, the control of their mutual concentrations is required. This can be achieved by the thermal treatment of samples in atmospheres with different p(O_2) as their concentration is interrelated through equation (1.6).

Considering the significant differences observed in the hysteresis pinching (Figure 4.4) and electrical conductivity (Figure 4.5) between 0.25 and 1.5 at.% Co-doped BFO ceramics, further studies are focused on these two extreme compositions. In order to investigate the influence of different types and concentrations of defects on the domain switching and electrical conductivity, the annealing of sintered samples in 10 atm O_2 and N_2 at 700 °C was adopted.

4.2.2 Influence of annealing atmosphere on 0.25 at.% Co-doped BFO ceramics

4.2.2.1 Domain switching

In Figure 4.7, the *P-E* hysteresis loops of 0.25 at.% Co-doped BFO ceramics after annealing in 10 atm O_2 and N_2 are displayed along with the *P-E* loop of the as-sintered sample as a reference. The difference between the loops of the as-sintered and the 10-atm-O_2-annealed sample is very small. On the other hand, the *P-E* loop after annealing in N_2 exhibits higher E_c (40 kV cm^{-1}) and lower P_r (7 μC cm^{-2}) in comparison to the as-sintered samples (E_c=36 kV cm^{-1}, P_r =11 μC cm^{-2}), indicating a hardening effect.

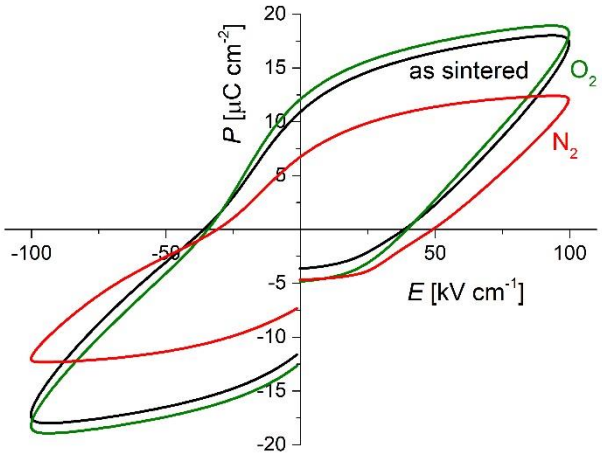

Figure 4.7: *P-E* hysteresis loops of as-sintered 0.25 at.% Co-doped BFO ceramics, annealed in 10 atm O_2 and N_2 at 100 kV cm^{-1}.

The results suggest that the domain-switching behavior and thus the DW-pinning effects in the 10-atm-O_2- (or as-sintered) and N_2-annealed samples are dominated by an expected different concentration of $V_O^{\bullet\bullet}$, which are known to act as strong pinning centers for DWs in, e.g., undoped and acceptor-doped PZT [16], [23]. The small difference in domain switching between the as-sintered and the 10-atm-O_2-annealed sample could be potentially explained by a relatively low concentration of $V_O^{\bullet\bullet}$ in the as-sintered sample (due to the low Co concentration, which generates a low amount of compensating $V_O^{\bullet\bullet}$; see equation (4.2)) with only a subtle decrease of the $V_O^{\bullet\bullet}$ concentration when the sample is annealed in 10 atm O_2. On the other hand, the reduced switching due to pinning effects observed after annealing in N_2 could be explained by the increased concentration of $V_O^{\bullet\bullet}$ due to the decreased concentration of $Fe_{Fe}^{\bullet}$ (eq. (1.6) shifted to the left side). The concentration of $V_O^{\bullet\bullet}$ could also be increased in the case when Co ions are nominally (in as-sintered sample) present as a mixture of Co^{2+} and Co^{3+} states. Namely, during N_2-annealing, the Co^{3+} could be reduced to Co^{2+}, promoting the formation of $V_O^{\bullet\bullet}$ (eq. (4.3) shifted to the right).

$$2Co_{Fe}^{x} + O_O^{x} \leftrightarrow 2Co'_{Fe} + V_O^{\bullet\bullet} + \frac{1}{2}O_2(g) \tag{4.3}$$

Note also that the stronger effect of N_2 could obviously be affected by the much higher difference in p(O_2) between N_2 (p(O_2)=10^{-6}) and air (p(O_2)=2×10^{-1}), as compared to the difference between the 10-atm-O_2-annealing (p(O_2)=10) and the air (p(O_2)= 2×10^{-1}). In equilibrium, the concentration of $V_O^{\bullet\bullet}$ is proportional to p(O_2).

4.2.2.2 Room-temperature electrical conductivity

In Figure 4.8, ε', ε'' and σ' as a function of frequency for 0.25 at.% Co-doped ceramics annealed in 10 atm O_2 and N_2 are shown together with the as-sintered sample as a reference. Strong dispersion of both ε' and ε'' at low frequencies (<1 Hz) can be observed after annealing in O_2 and N_2, similar to the as-sintered sample. By estimating the σ_{DC} from the plateau in σ' at low frequencies (see eq. (4.1)) it appears that the conductivity increases after annealing in both 10 atm O_2 and N_2 with respect to as-sintered sample, which could be explained as follows.

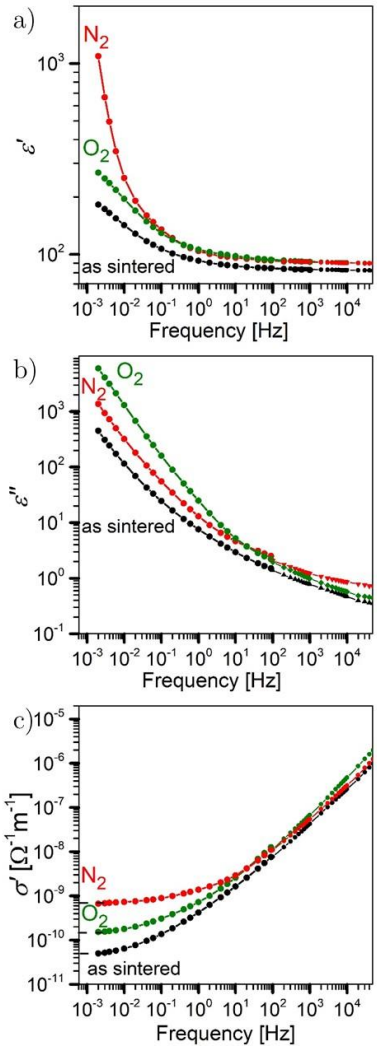

Figure 4.8: a) ε′, b) ε′′ and c) σ′ as a function of driving-field frequency for 0.25 at.% Co-doped BFO ceramics annealed in 10 atm O_2 and N_2 together with an as-sintered sample for reference.

According to the literature, the intrinsic defects in undoped BFO ceramics are $V_{Bi}^{'''}$, $V_O^{\bullet\bullet}$ and $Fe_{Fe}^{\bullet}$ when processed in air (i.e., oxygen-rich conditions) [49], [52]. Considering the results presented so far, it has been assumed that Co acts as acceptor, i.e., $Co_{Fe}^{'}$, thereby promoting the formation of extrinsic $V_O^{\bullet\bullet}$ and $Fe_{Fe}^{\bullet}$ in order to maintain the charge neutrality (eq. (1.6)). The concentration of the dopant in this composition is low (0.25 at.%), thus also the concentration of $Co_{Fe}^{'}$ and extrinsic $V_O^{\bullet\bullet}$ and $Fe_{Fe}^{\bullet}$ should be low. During annealing in 10 atm O_2, the concentration of $V_O^{\bullet\bullet}$ is decreased (eq. (1.6) to the right), promoting the formation of holes. Although further experiments and evidences

would be required, it might be considered that the holes released in the lattice will rather oxidize Co^{2+} into Co^{3+} than Fe^{3+} to Fe^{4+} [142]. This assumption could be potentially supported with a study in ref. [147], where the oxidation of Co-doped BFO thin films resulted in the formation of Co^{3+}; however, the oxidation of Fe^{3+} to Fe^{4+} was not confirmed. Nevertheless, considering that the concentration of Co^{2+} is low in 0.25 at.% Co-doped BFO due to low absolute concentration of Co, there is not much Co^{2+} to be oxidized into Co^{3+}. Therefore, the holes released in the lattice will further oxidize Fe^{3+} into Fe^{4+}, resulting in an increased concentration of $Fe^{\bullet}_{Fe}$ and thus a slightly increased conductivity.

On the other hand, the apparent increase of the conductivity after annealing in N_2 with respect to the as-sintered sample is more difficult to explain as such behavior, in the first approximation, would not be consistent with the assumed p-type conductivity. While one reasonable explanation is the reduction of Fe^{3+} to Fe^{2+} and thus the onset of n-type conductivity induced after annealing in N_2, the results of the Seebeck-coefficient measurements shown in the next chapter (Figure 4.9) clearly demonstrate p-type conductivity upon heating and cooling in N_2. Nevertheless, the data on 1.5 Co presented subsequently in Chapter 4.2.3 suggests an alternative possible explanation related to M-W relaxation. The results shown here for 0.25 at.% Co-doped BFO will be explained later in Chapter 4.2.3, where data on 1.5 Co are presented.

4.2.2.3 Temperature-dependent electrical conductivity and Seebeck coefficient

The discussion on RT electrical conductivity measurements considers that in the used post-annealing $p(O_2)$ range (from ~10^{-6} to 10 atm), the conductivity is still p-type. In order to confirm this, *in-situ* measurements of AC conductivity and the Seebeck coefficient as a function of temperature and annealing atmosphere, i.e., in synthetic air and N_2, are analyzed next. The results are presented in Figure 4.9, where the curves labeled 1, 2 and 3 refer to the cooling cycle in air, the heating cycle in N_2 and the cooling cycle in N_2, respectively. In the case of annealing in air, only the curve obtained during the cooling cycle is shown (curve 1) as no noticeable changes between the heating and cooling cycles were observed.

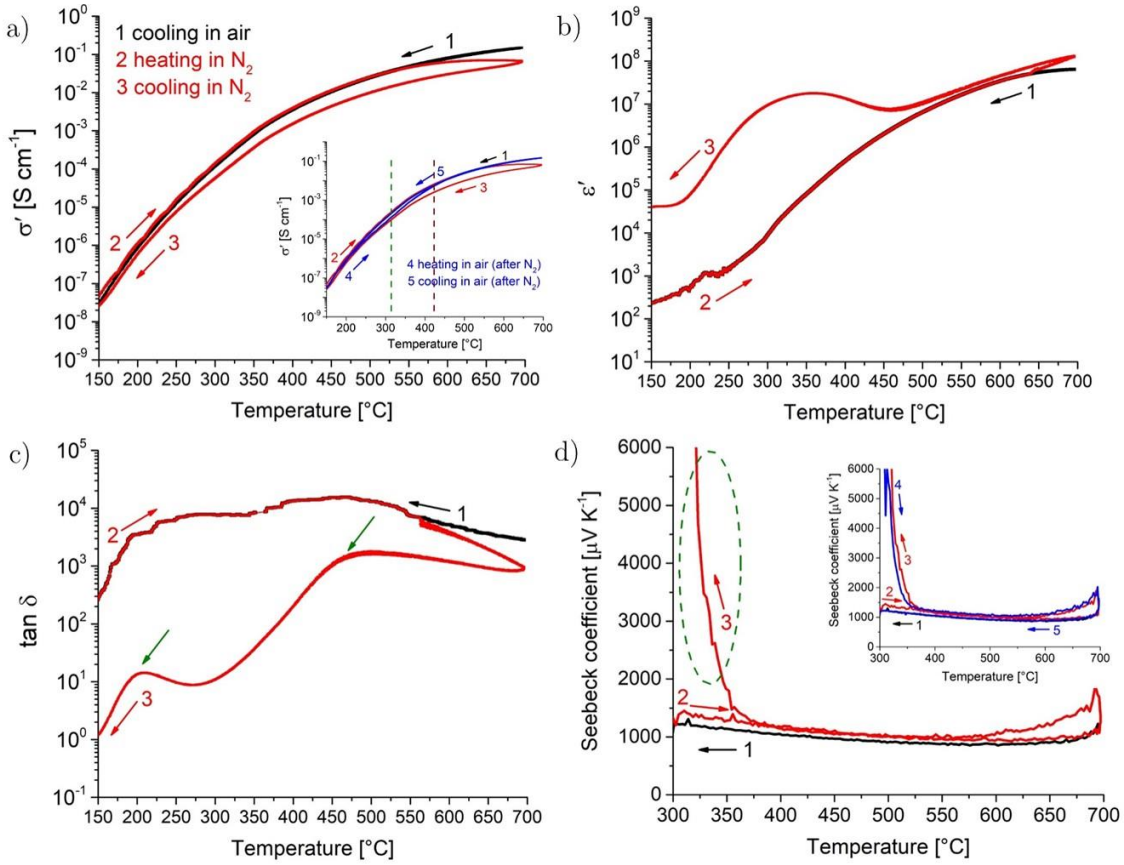

Figure 4.9: a) σ' , b) ε', c) $tan\,\delta$ and d) Seebeck coefficient as a function of temperature and annealing atmosphere measured on 0.25 at.% Co-doped BFO ceramics. Curves 1, 2, 3, 4 and 5 correspond to cooling in air (first cycle), heating in N_2, cooling in N_2, heating in air (second cycle done after that in N_2) and cooling in air (after N_2), respectively. The insets in a) and d) demonstrate the reversibility of the redox processes. The dashed green and maroon lines in the inset of a) correspond to the temperature where the re-oxidation starts and finishes, respectively. Green arrows in c) indicate the peak in $tan\,\delta$ and green oval in d) indicates the increase of the Seebeck coefficient below ~350 °C during cooling in N_2. See main text for further details regarding these notations.

From Figure 4.9a it can be seen that the conductivity (σ'), decreases with decreasing temperature (curve 1, air), as expected. Upon heating in N_2 (curve 2), the curve traces that were measured in air during cooling (curve 1) but only up to ~550°C when the conductivity in N_2 reaches a plateau and deviates from the trend measured in air (compare curves 1 and 2 above 550°C in Figure 4.9a). Upon cooling in N_2 (curve 3), the conductivity decreases as expected; however, the absolute conductivity value is lower than that measured during heating in N_2 (curve 2), all the way down to 150 °C, suggesting a decrease in the conductivity of the sample after annealing in N_2. In order to evaluate the reversibility of the observed changes, the sample was re-annealed in air and the results are displayed in the inset of Figure 4.9a. The curves 4 and 5 refer to the heating and cooling cycles in air, respectively, which were made after the sample was already annealed in N_2. It can be observed that upon re-annealing in air (curve 4), the curve traces that were measured in N_2 during cooling (curve 3) only up to ~310 °C (indicated by dashed green line) and afterwards deviates from the trend (compare curves 3 and 4 above 300 °C). Moreover, upon re-annealing in air (curve 4), the curve starts to trace the one measured in air during

cooling (curve 1) at ~425 °C (indicated by dashed maroon line), implying that the conductivity has been recovered to its initial state and that the sample has been re-oxidized. This is confirmed by the fact that the last cooling part (curve 5) traces exactly the cooling curve from the first annealing in air (curve 1). These results demonstrate that the changes observed during annealing in different $p(O_2)$ are reversible and therefore not related to secondary phenomenon such as, e.g., the formation of secondary phases. Qualitatively, a similar decrease of the electrical conductivity during annealing in N_2 was reported for KBT-modified BFO ceramics [148], in agreement with the p-type conductivity of BFO and related materials [49], [52], [65], [148].

Further inspection of the real part of the dielectric permittivity presented in Figure 4.9b reveals that during cooling in N_2 (curve 3), a strong step-like feature appears in ε', accompanied by peaks in $tan\,\delta$ (indicated by green arrows in Figure 4.9c, curve 3). Note that this effect is clearly induced by the N_2 annealing as it appears during cooling of the sample. It is assumed that this anomaly is not related to a phase transition as there is no expected structural transformation in this temperature range in BFO [149]. This anomaly is probably of a M-W origin, as discussed for BFO-related materials [148], [150], arising due to local differences in the electrical conductivity inside the sample. According to the proposed defect model for BFO [49], annealing in N_2 leads to the reduction of Fe^{4+} into Fe^{3+}, creating positively charged $V_O^{\bullet\bullet}$ (equation (1.6) shifted to the left). These local differences in electrical conductivity might stem from the inhomogeneous reduction in N_2 and thus the uneven distribution of major charge carriers (Fe^{4+}), similarly to that previously suggested for KBT-modified BFO [148]. This scenario is later confirmed by local conductive AFM measurements (see Chapter 4.3.1 and discussion therein).

The Seebeck coefficients of 0.25 at.% Co-doped BFO ceramics obtained during a cooling cycle in air (curve 1), a heating cycle in N_2 (curve 2) and a cooling cycle in N_2 (curve 3) are presented in Figure 4.9d. First, the Seebeck coefficient is positive in the whole temperature range by annealing both in air and N_2, confirming that the sample maintains a dominating p-type conductive behavior where Fe^{4+} are the major charge carriers. However, in N_2 the magnitude of the Seebeck coefficient significantly and exponentially increases at lower temperatures, <350 °C, during cooling (curve 3 in Figure 4.9d; dashed green oval). This effect is reproducible and completely reversible by post-annealing the N_2-annealed samples back in air (see inset, curve 4), which is consistent with conductivity measurements (compare with inset in Figure 4.9a). We propose that the large increase in S at low temperatures during cooling in N_2 is intimately related to the relaxation in the dielectric permittivity induced by N_2 annealing, arising due to an inhomogeneous reduction in N_2 and the creation of regions inside the ceramics with variable electrical conductivity (M-W effects). Considering the general relationship between the Seebeck coefficient (S) and the charge-carrier concentration (C) expressed as [151]

$$S \propto ln\frac{1-C}{C} \tag{4.4}$$

we can infer that regions of reduced p-type carrier concentration inside BFO upon reduction in N_2 should exhibit a higher Seebeck coefficient. Indeed, simple modeling of the Seebeck effects in composites between inorganic filler (SnSe) and conducting polymer poly(3,4-ethylenedioxythiohene):polystyrene-sulfate (PEDOT:PSS) showed that introducing a component with lower conductivity in series with a component having a comparably elevated conductivity can considerably increase (by a factor of ~7) the total Seebeck coefficient of the composite [152]. In analogy, we may envisage in BFO regions of the sample (e.g., grain boundaries and/or DWs) which were reduced in N_2

inhomogeneously, resulting in a composite-like effect and a large effective coefficient S, as observed experimentally.

4.2.3 Influence of annealing atmosphere on 1.5 at.% Co-doped BFO ceramics

4.2.3.1 Domain switching

In Figure 4.10, the P-E hysteresis loops of 1.5 at.% Co-doped BFO ceramics after annealing in 10 atm O_2 and N_2 are displayed along with the P-E loop of the as-sintered sample as a reference. It can be observed that after annealing in 10 atm O_2, the loop is still pinched but opens up, suggesting facilitated polarization switching. On the contrary, after annealing in N_2, switching is remarkably reduced, as seen by the underdeveloped hysteresis in Figure 4.10. To further allow the development of the loop, the inset shows the P-E loop of N_2-annealed samples obtained at a higher field of 160 kV cm^{-1}. Relative to the sample annealed in air with E_c = 80 kV cm^{-1}, the E_c is reduced after annealing in O_2 (E_c =70 kV cm^{-1}), while strongly increased after annealing in N_2 (E_c = 120 kV cm^{-1}).

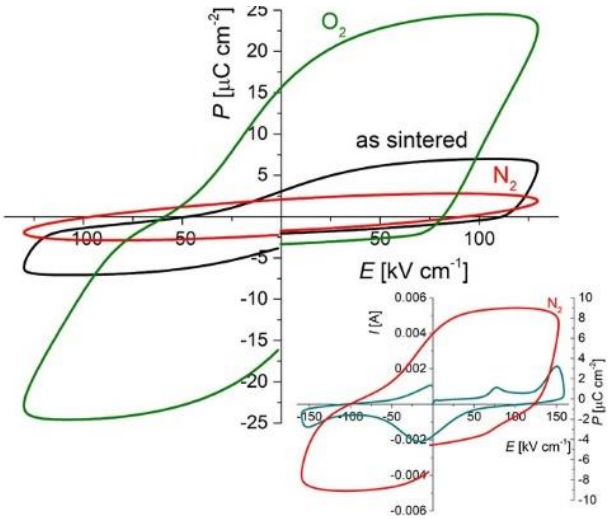

Figure 4.10: P-E loops of as-sintered 1.5 at.% Co-doped BFO ceramics, annealed in 10 atm O_2 and N_2 at 130 kV cm^{-1}. The inset displays P-E and the corresponding I-E loop of N_2-annealed sample measured at 160 kV cm^{-1}.

The distinct differences in the domain-switching behavior after annealing in 10 atm O_2 and N_2 give a strong indication that the DW-pinning effects are governed by $V_O^{\bullet\bullet}$. The facilitated domain switching after annealing in 10 atm O_2 could be related to a decreased concentration of $V_O^{\bullet\bullet}$ pinning centers due to oxidation (see eq. (1.6) shifted to the right side) and, potentially, a reduction of the Co'_{Fe} pinning centers (due to Co^{2+}-to-Co^{3+} oxidation as shown by eq. (4.3) shifted to the left). This possibility was not considered for the 10-atm-O_2-annealed BFO with 0.25 at.% Co (previous Chapter 4.2.2) due to the assumption that the concentration of Co^{2+} and the compensating $V_O^{\bullet\bullet}$ is low in that sample, which is further supported by the negligible difference in domain switching between the 10-atm-O_2-annealed and as-sintered samples (Figure 4.7).

On the other hand, the reduced polarization switching due to pinning effects observed after annealing in N_2 could be, inversely, explained with an increased concentration of $V_{\dot{O}}^{\bullet\bullet}$ (eq. (1.6) shifted to the left side) and potentially also an increased concentration of Co'_{Fe} (eq. (4.3) shifted to the right side).

4.2.3.2 Room-temperature electrical conductivity

In Figure 4.11, ε', ε'' and σ' as a function of frequency for 1.5 at.% Co-doped ceramics annealed in 10 atm O_2 and N_2 are shown together with the as-sintered sample as a reference. As can be observed, there are only small differences between the permittivity/conductivity of the as-sintered and the 10-atm-O_2-annealed samples. On the other hand, the sample annealed in N_2 exhibits a strong step-like increase in ε' at low frequencies, accompanied by a peak in ε'' and a step in σ', clearly suggesting a relaxation process that is induced by annealing in N_2.

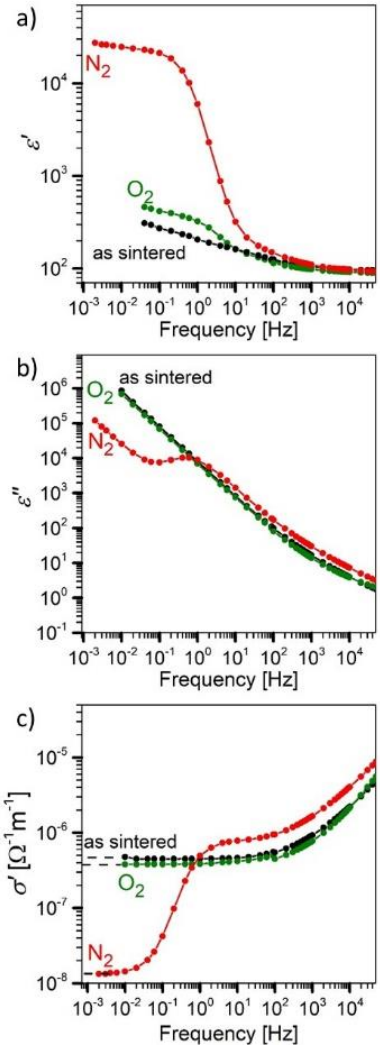

Figure 4.11: a) ε', b) ε'' and c) σ' as a function of driving-field frequency for 1.5 at.% Co-doped BFO ceramics annealed in 10 atm O_2 and N_2 together with as-sintered sample for reference.

As already discussed in the previous chapter, the relaxation induced by N_2 annealing is likely of a M-W origin, associated with local differences in the electrical conductivity due

to local reduction in N_2 and thus an uneven distribution of Fe^{4+}. In the simplest scenario, assuming in the first qualitative approximation an equivalent circuit model consisting of a low conductive thin layer connected in series with a conductive bulk [148], [153], the lower plateau in the σ' step at low frequencies ($<10^{-2}$ Hz) in Figure 4.11c (dashed line) should correspond to the low-conductive (reduced) region(s). Following this reasoning, from the plateau (dashed line) in σ' (see eq. (4.1)), it was estimated that the N_2 annealing lowered the σ_{DC} by more than an order of magnitude, i.e., from $\sim 5 \times 10^{-7}$ (as-sintered) to $\sim 1 \times 10^{-8}$ $\Omega^{-1}m^{-1}$ (N_2).
In contrast to the reduced conductivity in N_2, which is very consistent with the literature data and the p-type conductivity [49], [52], [64], [65], [154] (see introduction, Chapter 1.2.1), the negligible change in the conductivity after annealing in 10 atm O_2, with respect to air annealing, i.e., as-sintered sample, (see Figure 4.11c), is more difficult to explain. However, taking into consideration the proposed defect energy states within the bandgap in Co-doped BFO by Bien *et al.* [147], it is possible that Co^{2+} is easier to oxidize into Co^{3+} than Fe^{3+} into Fe^{4+}, leading to minor changes in the Fe^{4+} concentration and thus in the conductivity.

Finally, a clear relaxation behavior in the permittivity after N_2 annealing, as seen here for the 1.5 Co sample (Figure 4.11, red curve), is not observed in the 0.25 Co sample (Figure 4.8, red curve). While the relaxation in the 0.25 Co could be easily shifted to lower frequencies, outside the measured frequency window ($<10^{-3}$ Hz), the clear peak in $tan\,\delta$ and the step in ε' observed after cooling in N_2 (Figure 4.9b,c; curves 3), strongly support the M-W mechanism in this sample (0.25 Co). Similarly, we show next this same temperature behavior appearing in the 1.5 Co, suggesting a common M-W-like mechanism induced in Co-doped BFO ceramics by N_2 annealing.

4.2.3.3 Temperature-dependent electrical conductivity and Seebeck coefficient

In-situ measurements of the AC conductivity and Seebeck coefficient as a function of temperature and annealing atmosphere, i.e., in synthetic air and N_2, are analyzed in this section, like for the 0.25 Co sample in Chapter 4.2.2. The results are presented in Figure 4.12 with the same labelling as in Chapter 4.2.2, thus the curves 1, 2 and 3 refer to the cooling cycle in air, the heating cycle in N_2 and the cooling cycle in N_2, respectively.

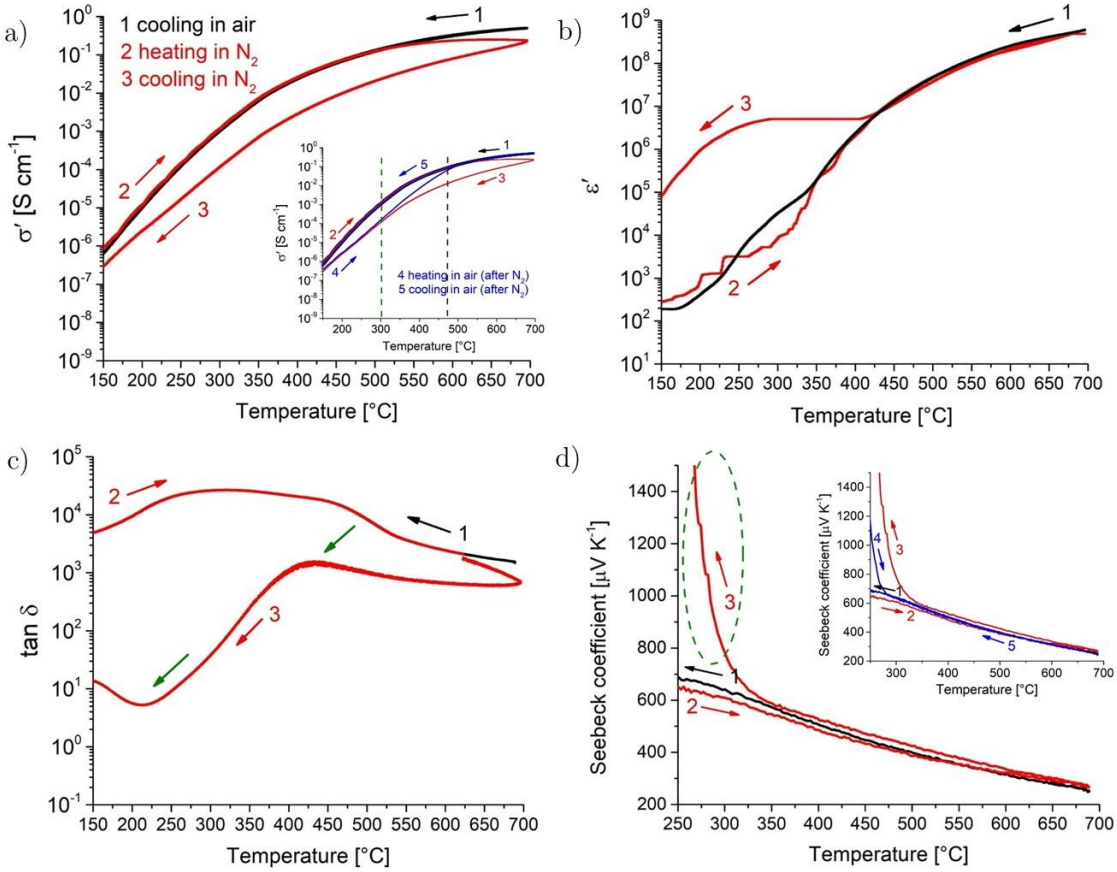

Figure 4.12: a) σ' , b) ε', c) $tan\,\delta$ and d) Seebeck coefficient as a function of temperature and annealing atmosphere for 1.5 at.% Co-doped BFO ceramics. Curves 1, 2, 3, 4 and 5 correspond to cooling in air (first cycle), heating in N_2, cooling in N_2, heating in air (second cycle done after that in N_2) and cooling in air (after N_2), respectively. The insets in a) and d) demonstrate the reversibility of redox processes. The dashed green and maroon lines in the inset of a) indicate the temperature of the initiated and completed oxidation, respectively. Green arrows in c) indicate the peak in $tan\,\delta$, while the dashed green oval in d) marks the increase of the Seebeck coefficient at lower temperatures upon cooling in N_2. See the main text for further details regarding these notations.

Figure 4.12a shows that upon heating in N_2 (curve 2), the curve traces that measured in air during cooling (curve 1) only up to ~550°C when the conductivity in N_2 reaches a plateau and deviates from the trend measured in air (compare curves 1 and 2 above 550 °C). Upon cooling in N_2 (curve 3), the conductivity decreases as expected; however, the absolute conductivity value is lower than that measured during heating in N_2 (curve 2), all the way down to 150°C, suggesting a decrease in the conductivity of the sample after annealing in N_2. The behavior is thus qualitatively the same as that observed in the 0.25 Co composition (Figure 4.9a). The reversibility was checked by re-annealing the sample in air and the results are displayed in the inset. The curves 4 and 5 refer to heating and cooling cycles in air, respectively. It can be observed that upon re-annealing in air (curve 4), the curve traces that measured in N_2 during cooling (curve 3) only up to ~300 °C (indicated by dashed green line) and afterwards deviates from the trend measured in N_2 (compare curves 3 and 4 above 300 °C). Moreover, upon re-annealing in air (4), the curve starts to trace the one measured in air during cooling (curve 1) at ~475 °C (indicated by

the dashed maroon line), demonstrating that the conductivity was recovered to its initial state and that the sample was re-oxidized.

The real part of the dielectric permittivity displayed in Figure 4.12b shows that during cooling in N_2 (curve 3), a strong increase in ε' appears, accompanied by peaks in $tan\,\delta$ (indicated by the green arrow in Figure 4.12c, curve 3). As discussed for the 0.25 Co sample (Chapter 4.2.2), we infer to the same M-W-like relaxation mechanism induced by N_2 annealing, which is consistent with the relaxation measured in the permittivity at room temperature after annealing in N_2 (see Figure 4.11).

The Seebeck coefficients of 1.5 at.% Co-doped BFO ceramics obtained during the cooling cycle in air (curve 1), the heating cycle in N_2 (curve 2) and the cooling cycle in N_2 (curve 3) are presented in Figure 4.12d. The Seebeck coefficient is positive in the whole temperature range by annealing both in air and N_2, confirming that the sample maintains a dominating p-type conductive behavior. Exactly as in the case of the 0.25 Co sample, in N_2 the magnitude of the Seebeck coefficient significantly increases at lower temperatures during cooling (curve 3 in Figure 4.12d; the increase is indicated by a dashed green oval). This effect is reproducible and reversible by post-annealing the N_2-annealed samples back in air (see inset), which is consistent with conductivity measurements (see the inset in Figure 4.12a). The increase in S is presumably associated with the inhomogeneous reduction of the sample during annealing in N_2, i.e., composite-like effect, analogous to observations in 0.25 at.% Co-doped BFO (see Section 4.2.2.3 for details).

In order to explore the redox kinetics and possibly explain the local nature of the reduction in N_2, leading to the relaxation in the permittivity data and the increase of the Seebeck coefficient at lower temperatures (Figure 4.11, Figure 4.12), isothermal DC conductivity measurements were performed at 600 °C upon changing the atmosphere between O_2 and N_2. As can be observed in Figure 4.13, the conductivity decreases upon switching the atmosphere from O_2 to N_2 and increases again upon switching from N_2 to O_2. This is consistent with the p-type behavior of BFO. Moreover, it can be seen that the relaxation time upon the step-like decrease in $p(O_2)$ (i.e., switch from O_2 to N_2) and the increase in $p(O_2)$ (i.e., switch from N_2 to O_2), appears to be extremely fast, i.e., of the order of minutes.

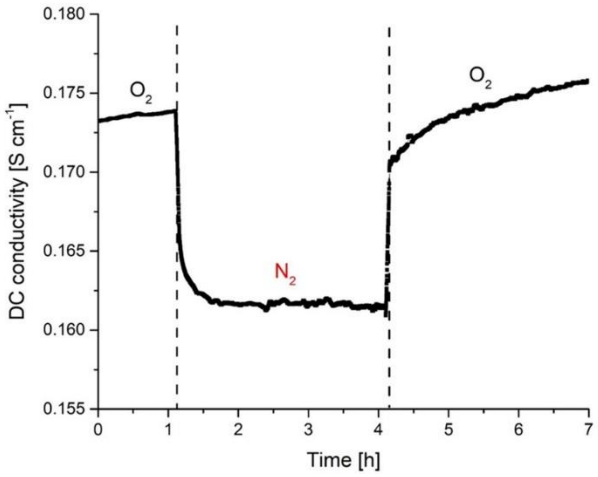

Figure 4.13: Relaxation of electrical conductivity upon switching between O_2 and N_2 atmospheres at 600 °C for 1.5 at.% Co-doped BFO ceramics.

Fast redox kinetics has been observed in hexagonal manganites [155] due to the highly mobile interstitial oxygen ions. The close-packed structure of BFO, however, is not

favorable for interstitial defects. In addition, fast redox kinetics cannot simply be attributed to microstructural origins, e.g., porosity, as the BFO samples exhibited close porosity (relative density ~93%). Another possibility to explain the fast conductivity relaxation is that the redox processes occur at the surface of the sample. We note, however, that a decrease in the electrical conductivity, i.e., a reduction in N_2, has also been observed in the permittivity measurements performed at room temperature (see Figure 4.11), where the surface layer with a few hundred microns was removed prior to the analysis. A final possibility is localized redox processes, which may preferentially occur along grain boundaries and/or domain walls, as has been recently reported in ref. [52].

To sum up, considering the results presented in Chapters 4.2.2 and 4.2.3, it can be concluded that the behavior of 0.25 and 1.5 at.% Co-doped ceramics is qualitatively comparable. Furthermore, the results of *in-situ* AC conductivity and Seebeck coefficient measurements performed on 0.5 and 1.0 at.% Co-doped samples, presented in Appendix A, demonstrate the qualitatively comparable behavior of all the Co-doped compositions. For this reason, we consider a qualitatively common pinning mechanism for Co-doped BFO in the whole concentration range.

The results for 0.25 and 1.5 at.% Co-doped ceramics (Chapters 4.2.2 and 4.2.3) indicate localized redox processes after annealing in N_2, which may preferentially occur, e.g., along grain boundaries and/or domain walls [52]. In the next chapter we investigate the possibility of localized redox processes using, for simplicity, only the 1.5 at.% Co-doped BFO ceramics.

4.3 Experimental Investigation of Point Defects in Co-Doped BFO Ceramics

4.3.1 Local electrical conductivity

In order to investigate the conductivity of the GBs and DWs on a local scale in ceramics, conductive atomic-force microscopy (c-AFM) combined with piezo-response force microscopy (PFM) analyses were performed. We were particularly interested in the changes in the local conductivity induced after annealing in N_2 to explain the macroscopic M-W behavior suggested in previous chapters. This analysis was made based on recent data in $BiFeO_3$ [52], [92] showing that the local conductivity at DWs, as identified by c-AFM, is closely related to the accumulation of p-type defects (electron holes).

Figure 4.14 shows the results for the as-sintered and N_2-annealed samples of 1.5 at.% Co-doped BFO ceramics. Note that while these are representative images, a more rigorous statistical analysis of conductive DWs and GBs is presented at a later stage.

In the as-sintered sample, an enhanced current signal can be observed in several regions (Figure 4.14b, see bright lines and arrows), which were (Figure 4.14a) identified as DWs (green arrow) and GBs (red arrow) with PFM. The increased current signal at these interfaces is clearly confirmed by the c-AFM profiles shown in Figure 4.14c,d. An increased current signal at DWs in BFO ceramics has been observed also in a recent study by Rojac *et al.* [52], where the origin of DW conduction was attributed to the presence of Fe^{4+}. No evidence, however, was reported for conductive GBs, which are clearly identified in Figure 4.14d.

After annealing in N_2, a similar PFM and c-AFM analysis was performed, shown in Figure 4.14e-h. While we qualitatively identified the conductive DWs and GBs also in the N_2 annealed sample, statistically, they are less conductive in this N_2-annealed sample as compared to the as-sintered sample. In order to get a more quantitative insight into conductive GBs and DWs in the as-sintered and N_2-annealed samples, a statistical analysis of the local current at GBs and DWs was performed and the fractions of conductive DWs and GBs were determined (details regarding the analysis and statistical representation of a single DW and a single GB can be found in the experimental section, Chapter 3.2.5). Multiple areas in as-sintered and N_2-annealed samples were analyzed with c-AFM, probing a total of ~140 grains and ~180 DWs per sample. The fractions of conductive GBs were 26 % and 17 % and of the conductive DWs were 49 % and 26 % for as-sintered and N_2-annealed sample, respectively. From these results, we can conclude that the local conductivity of the analyzed regions is reduced after annealing in N_2. This is related to the local reduction of the major charge carriers, Fe^{4+}, by N_2 annealing. We are aware that in the case of GBs, the local current signal can be altered by the cross talk with topography [156]. However, the results of statistical analyses of the conductive GBs in as-sintered and N_2-annealed samples (polished by the same procedure) indicate that not only the topography, but also the charge defects are responsible for the enhanced current at GBs.

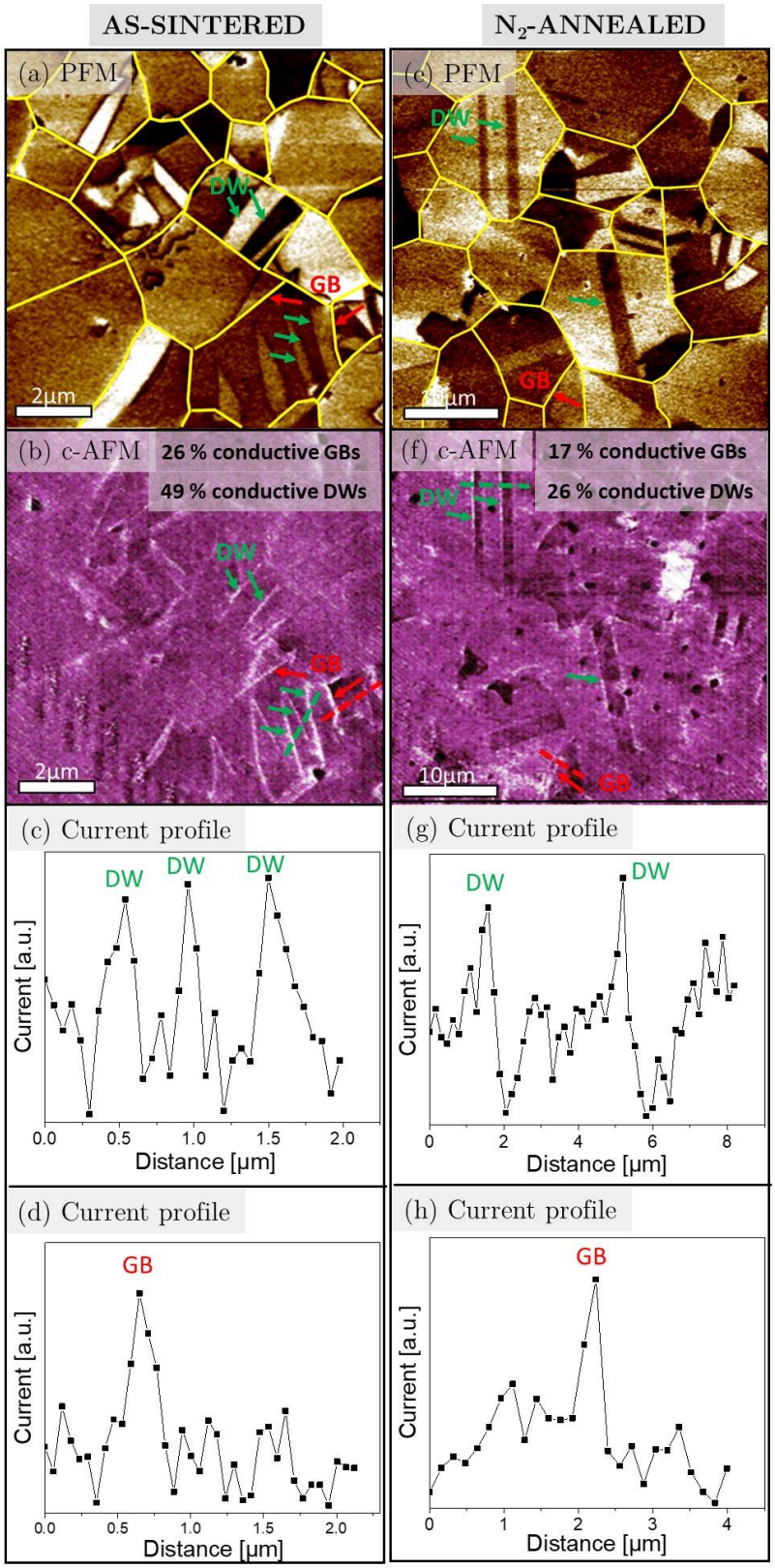

Figure 4.14: Local conductivity measurements on Co-doped BFO ceramics. (a,e) Out-of-plane PFM amplitude images, (b,f) c-AFM maps and (c-h) electric-current profiles corresponding to as-sintered (left column) and N_2-annealed sample (right column) of 1.5 at.% Co-doped BFO ceramics. Yellow lines in PFM images mark the grain boundaries (GBs). The green and red arrows in the PFM and c-AFM images denote those DWs and

GBs, respectively, where the enhanced electric current-signal was clearly observed by c-AFM. The green and arrow dashed lines in the c-AFM images correspond to the distance along which the electric-current profiles, shown in panels (c-h), were extracted. The DW and GB positions along this distance are indicated on the profiles (DW-domain wall, GB-grain boundary).

To summarize, the results presented in this chapter demonstrate the enhanced conductivity of DWs and GBs in an as-sintered sample. However, the conductivity of DWs and GBs was on average lower after annealing in N_2, indicating a local chemical reduction of Fe^{4+} to Fe^{3+} [52]. While details of the complex M-W mechanism are currently not completely understood, we interpret this partial reduction in the local conductivity to be implicated in the macroscopic M-W behavior, as observed in the dielectric at RT (Figure 4.11) and *in-situ* DC, AC and Seebeck coefficient measurements (Figure 4.12).

4.3.2 Type of point defects

4.3.2.1 Atomic-scale investigation by atomic-resolution microscopy

In this section we further investigate point defects responsible for the enhanced local conductivity of GBs and DWs (Figure 4.14). The chemical analysis was performed on the atomic scale using the HAADF STEM and EELS techniques on as-sintered and N_2-annealed samples of 1.5 at.% Co-doped ceramics.

The results obtained on the as-sintered sample are collected in Figure 4.15. In Figure 4.15a a HAADF image is shown with identified DW (dashed-orange box). The position of DW was identified by analyzing the direction of Fe displacements from the center of the Bi sub-lattice (denoted by blue arrows). The presence of Bi vacancies was analyzed by measuring the intensities of Bi columns inside the red box with the resulting map of the normalized Bi intensities shown in Figure 4.15b. In the middle of DW, the intensity is ~10 % lower with respect to the maximum Bi-atom column intensity. As reported previously, the lower Bi column intensity is because of the Bi atoms missing from their regular places, confirming the presence of Bi vacancies accumulated inside the DW region.

Furthermore, the oxidation state of Fe on and off the DW was investigated by measuring the energy-onset difference (ΔE) between the O-K and Fe-L_3 edges from the EELS spectra (details of the method are reported in Chapter 3.2.4). The EELS spectra acquired on and off the DW are shown in Figure 4.15c, respectively. The obtained value of ΔE on the DW was 179.25 eV, while ΔE off the DW was 178.5 eV. These results imply that the oxidation state of Fe is different inside the DW region than outside it. From the comparison of the obtained ΔE values with standard ΔE values for different Fe oxidation states reported in the literature [52], there is an indication that the Fe oxidation state at DWs tends towards 4+ (ΔE: on Fe^{4+} standard=179.9±0.4 eV, on DW= 179.25 eV) [93], while the domain contains mainly Fe^{3+} states (ΔE: on Fe^{3+} standard=178.3±0.2 eV, off DW= 178.5 eV). The results suggest the presence of V_{Bi}''' and $Fe_{Fe}^{\bullet}$ defects inside the DW region, which is consistent with the literature data on BFO ceramics [52], [93].

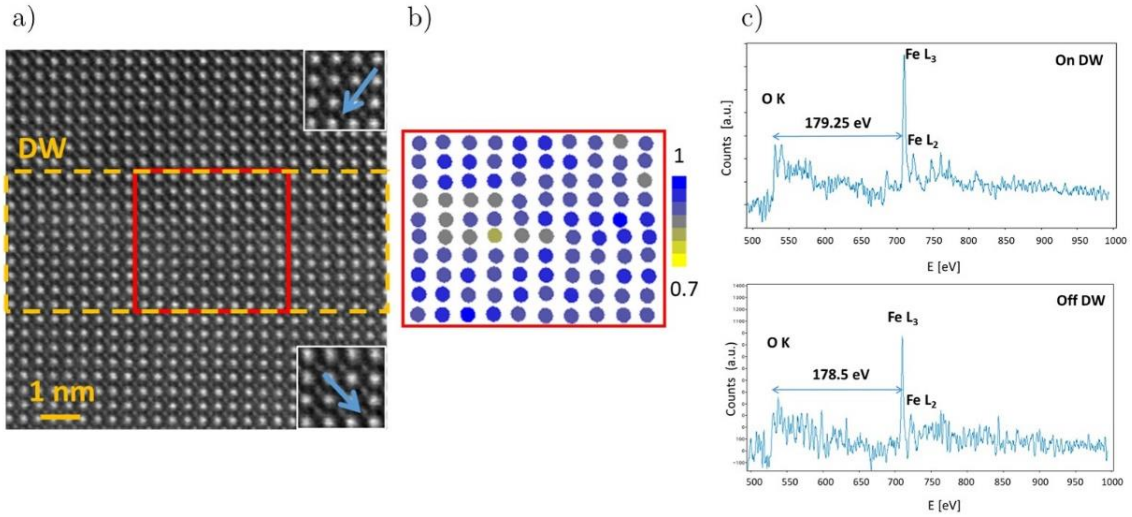

Figure 4.15: Identification of point defects at a neutral (head-to-tail) DW in **as-sintered** sample of 1.5 at.% Co-doped BFO ceramics. a) HAADF-STEM image with indicated DW region (dashed-orange box). The blue arrows indicate the direction of the Fe displacements from the center of the Bi sub-lattice, confirming the head-to-tail DW. The red box indicates the region that was considered for the analysis of the intensity distribution of Bi-columns. b) Normalized distribution map of the Bi-atom column intensities inside the DW region (corresponding to the red box in a)). The reduction of the Bi-column intensities inside the DW region (yellowish circles) indicates the presence of Bi vacancies. c) Experimental EELS spectra acquired on and off the DW, from which the energy onset difference (ΔE) between O-K and Fe-L_3 edges was evaluated. The ΔE on the DW was 179.25 eV and the ΔE off the DW was 178.5 eV.

Next, for comparison with the as-sintered sample, the N_2-annealed sample was analyzed and the HAADF-STEM image with the indicated DW region is shown in Figure 4.16a. The blue arrows indicate the direction of Fe displacements from the center of Bi sub-lattice. The presence of Bi vacancies was evaluated by measuring the intensities of Bi columns inside the red box and the normalized map is shown in Figure 4.16b. Similarly, as observed in the as-sintered sample (Figure 4.15b), the ~10% intensity drop in the middle of the DW region confirms the presence of the accumulated Bi vacancies. The measured ΔE between the O-K and Fe-L_3 edges from the EELS spectra is 178.25 eV on the DW and 178.5 eV off the DW (Figure 4.16c).

In contrast to the as-sintered sample (Figure 4.15), the N_2-annealed sample is characterized by the oxidation state of Fe^{3+} both on and off the DW [51]. This is consistent with the local reduction of Fe^{4+} into Fe^{3+} inside the DW region by annealing in N_2 and could therefore explain the statistically observed decrease of the DW electrical conductivity after the sample was annealed in N_2 (Figure 4.14).

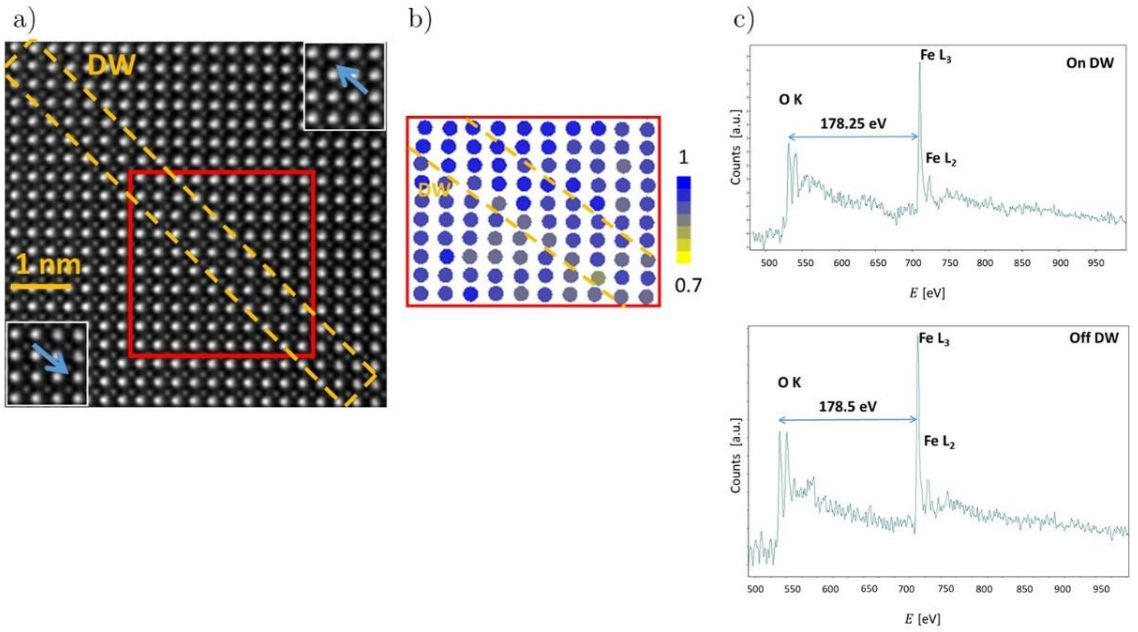

Figure 4.16: Identification of point defects at a neutral (head-to-tail) DW in **N_2-annealed** sample of 1.5 at.% Co-doped BFO ceramics. a) HAADF-STEM image with indicated DW region (dashed-orange box). The blue arrows indicate the direction of the Fe displacements from the center of the Bi sub-lattice. The red box indicates the region that was considered for the analysis of the intensity distribution of Bi-columns. b) The normalized distribution map of the Bi-atom column intensities inside the red box in a). The reduction of the Bi-atom column intensities (yellowish circles) inside the DW region (inside dashed-orange box) indicates the presence of Bi vacancies. c) Experimental EELS spectra acquired on and off the DW, from which the energy onset difference (ΔE) between O-K and Fe-L_3 edges was evaluated. The ΔE on and off the DW was 178.25 eV and 178.5 eV, respectively (for EELS results on standards see ref. [52]).

As opposed to Fe^{4+}, the analysis of the Bi-column intensities indicates the presence of V_{Bi}''' inside the DW region of the N_2-annealed sample, consistent with the observations from the as-sintered sample. Considering the results of the electrical conductivity and Seebeck-coefficient measurements (Figure 4.12), which showed the reversibility of redox processes, the overall concentration of Bi vacancies is not expected to change by annealing in N_2. However, the STEM analysis revealed that both samples exhibit ~10 % lower intensity of Bi columns in the middle of DW, thus it might be concluded that not only the concentration, but also location of Bi vacancies, is not changed after N_2 annealing. Nevertheless, this leaves open the question about the compensating defects, which are assumed to be $V_O^{\bullet\bullet}$. Based solely on these data, we cannot infer the presence of $V_O^{\bullet\bullet}$ at DWs. For $V_O^{\bullet\bullet}$ identification, we instead use EPR spectroscopy presented in the following chapter.

4.3.2.2 Macro-scale investigation by electron paramagnetic resonance spectroscopy

The presence of $Fe_{Fe}^{\bullet}$ and V_{Bi}''' inside the DW region of an as-sintered 1.5 at.% Co-doped sample has been directly confirmed with STEM analysis (Figure 4.15). However, the evidence about the presence of Co_{Fe}' and $V_O^{\bullet\bullet}$ is still lacking. According to the literature on

acceptor-doped lead-based (e.g., PT [30]–[32]) and lead-free materials (e.g., BNT [37], KNN [38]), $V_O^{\bullet\bullet}$ tend to form defect complexes with acceptor centres.

In order to further identify defects in Co-doped BFO ceramics, EPR was adopted as it is an extremely powerful tool for studying point defects in semiconductors and insulators. Moreover, this method has been proven to be appropriate for the identification of different acceptor-oxygen-vacancy defect complexes in several ferroelectric systems [157]. For this purpose, three different samples of 1.5 at.% Co-doped BFO ceramics were investigated by EPR, i.e., as-sintered, N_2-annealed and 10-atm-O_2-annealed.

The X-band spectra of as-sintered, N_2-annealed and 10-atm-O_2-annealed samples are presented in Figure 4.17 (empty symbols) together with the corresponding fits of a powder-averaged line (full line), which agree with the experimental data very well. Note that the spectra shown here were obtained above the Neel temperature of BFO ($T_N = 370$ °C) [149], i.e., at 400 °C, in order to avoid contributions of static internal fields due to antiferromagnetic ordering and therefore, to observe intrinsic contributions to spin-orbit coupling.

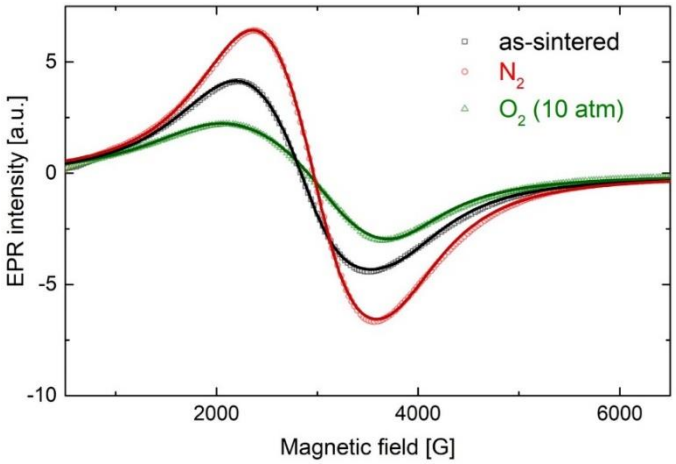

Figure 4.17: EPR spectra of as-sintered, N_2- and 10-atm-O_2-annealed sample of 1.5 at.% Co-doped BFO ceramics recorded at 400 °C (empty symbol) together with the corresponding fit (full lines).

Starting from the as-sintered sample, an anisotropic spectrum with $g_x = 1.80$, $g_y = 3.13$ and $g_z = 2.36$ was found by numerical spectrum simulations; the values of the fitting parameters are presented in Table 4.3. The principal g values for N_2- and 10-atm-O_2-annealed samples are $g_x = 1.82$, $g_y = 2.90$, $g_z = 2.28$ and $g_x = 2.23$, $g_y = 3.38$ and $g_z = 1.84$, respectively. Similar values were reported in the literature for low-spin Co^{2+} in square planar or pseudo-tetrahedral geometry [158], [159]. In the case of Co-doped BFO, we safely assume that Co occupies the B site of the perovskite structure and is surrounded by oxygen octahedra. The determined g values are thus consistent with the presence of Co^{2+} ions placed in a square-planar coordination of oxygen ions. This could be interpreted in terms of the presence of Co^{2+} surrounded by $V_O^{\bullet\bullet}$ and thus $Co'_{Fe} - V_O^{\bullet\bullet}$ defect complexes. According to the literature data, these g values could be alternatively attributed to high-spin Co^{2+} in a distorted tetrahedral geometry, which is again consistent with the presence of $V_O^{\bullet\bullet}$ residing in the vicinity of Co^{2+} [160]. However, it should be noted that the information about the defect complex structure (e.g., dimeric, trimeric configurations) could not be provided based on these EPR spectra.

The identification of Co^{2+} in the current study is in agreement with ref. [142] on Co-doped BFO thin films sintered in an O_2 flow, where it was found by X-ray photoelectron

spectroscopy that the Co ions are mostly in the oxidation state 2+ (a smaller fraction is in the 3+ state). Furthermore, the existence of cobalt-oxygen-vacancy defect complexes has been reported in a DFT study on Co-doped $SrTiO_3$, with a linear arrangement of $Co''_{Ti} - V_O^{\bullet\bullet}$ being energetically favored [161].

Table 4.3: EPR spectral fitting parameters of as-sintered, N_2-annealed and 10-atm-O_2-annealed 1.5 at.% Co-doped BFO ceramics.

Sample	g factors	Linewidth [mT]	Intensity [arb. units]
As-sintered	g_x= 1.80	141	895
	g_y = 3.13	177	
	g_z = 2.36	126	
N_2-annealed	g_x = 1.82	140	1186
	g_y = 2.90	164	
	g_z = 2.28	122	
10-atm-O_2-annealed	g_x = 2.23	149	668
	g_y =3.38	209	
	g_z =1.84	132	

The intensity of the EPR signal is directly proportional to the numbers of unpaired electrons in the sample. In this study, the masses of the powders were the same in all the three cases, which means that the intensity of the EPR signal can be directly linked to the defect concentration. If the observed signal is indeed related to $Co'_{Fe} - V_O^{\bullet\bullet}$ type of defects, the highest intensity should be seen in the N_2- and the lowest in the O_2-annealed sample, which is indeed observed experimentally (Figure 4.17). The concentration of $Co'_{Fe} - V_O^{\bullet\bullet}$ defect complexes is increased by annealing in N_2 and decreased by annealing in O_2, relative to the as-sintered sample. The increased concentration of $Co'_{Fe} - V_O^{\bullet\bullet}$ defect complexes could be related to reduction of Co^{3+} into Co^{2+} and the formation of $V_O^{\bullet\bullet}$ considering that the as-sintered sample most likely contains a mixture of Co^{3+} and Co^{2+} [142]. Another possibility for the increased concentration of $Co'_{Fe} - V_O^{\bullet\bullet}$ defect complexes is the formation of $V_O^{\bullet\bullet}$ due to the reduction of Fe^{4+} into Fe^{3+}, which then diffuses close to the Co^{2+} ions as $V_O^{\bullet\bullet}$ should be attracted to acceptor centers.

4.4 Proposed Defect Model and Hardening Mechanism in Co-Doped BFO Ceramics

The results of this study demonstrate that by increasing the concentration of Co, the electrical conductivity increases (Figure 4.5) as well as the hysteresis-loop pinching related to hardening effects (Figure 4.4). Based on this behavior, we assumed that Co acts as acceptor, promoting the formation of $V_O^{\bullet\bullet}$ (eq. (4.2)) and $Fe_{Fe}^{\bullet}$ (eq. (1.6)). For this case, the charge neutrality condition can be expressed as

$$3[V_{Bi}'''] + [Co_{Fe}'] = 2[V_O^{\bullet\bullet}] + [Fe_{Fe}^{\bullet}] \tag{4.5}$$

We next explain the results and possible pinning mechanisms using this neutrality equation. We begin with the 1.5 Co sample, followed by other concentrations.

In 1.5 at.% Co-doped BFO ceramics, the high concentration of extrinsic Co_{Fe}' and $V_O^{\bullet\bullet}$ probably dominates the defect chemistry of BFO over intrinsic V_{Bi}''', $V_O^{\bullet\bullet}$ and $Fe_{Fe}^{\bullet}$. We infer that the concentration of V_{Bi}''' is frozen-in at lower temperatures (<700 °C) by the quasi-equilibrium achieved during sintering and is not altered by post-annealing in N_2. This is supported by the confirmed reversibility of the redox processes (see insets in Figure 4.12). The results also indicate that the major contribution to the elevated p-type electrical conductivity is due to $Fe_{Fe}^{\bullet}$ (Figure 4.14, Figure 4.15 and Figure 4.16), consistent with the literature data. Furthermore, we assume there are two types of pinning centers, i.e., i) V_{Bi}''' and $Fe_{Fe}^{\bullet}$ defects that have a tendency to accumulate at DWs (STEM results in Figure 4.15) from which they can provide pinning effects, and ii) Co_{Fe}' and $V_O^{\bullet\bullet}$ which are bound into complexes (EPR results, Figure 4.17). The question to be answered is whether and which defect(s) dominates the DW-pinning behavior at switching electric fields (hysteresis pinching; Figure 4.10).

We found that annealing in N_2 results in strongly impeded polarization switching (Figure 4.10). The reduction in N_2 occurs locally, as evidenced by the relaxation in ε' at RT (Figure 4.11a) and at elevated temperatures (Figure 4.12b), increased Seebeck coefficient at lower temperatures (Figure 4.12d) and fast redox kinetics (Figure 4.13). Moreover, the results of the c-AFM analysis in Figure 4.14 demonstrate that the conductivity of GBs and DWs is on average, as observed from a local scale, lower after annealing in N_2 with respect to the as-sintered sample. This is related to the reduction of Fe^{4+} into Fe^{3+} at these local regions of the sample and has been confirmed with STEM analysis (Figure 4.15, Figure 4.16). Therefore, it can be concluded that the concentration of $Fe_{Fe}^{\bullet}$-related pinning centers is lowered the most after annealing in N_2 and thus cannot explain the stronger pinning behavior of N_2-annealed BFO, if they would be the dominant pinning centers in the first place. We leave open the possibility, however, that the different switching behavior after annealing in N_2 might be affected by the internal field distribution inside the grain matrix related to the M-W effects. In contrast, the concentration of $Co_{Fe}' - V_O^{\bullet\bullet}$ complexes increases after annealing in N_2 (EPR results in Figure 4.17); the strong hardening induced by N_2 annealing thus originates from the increased concentration of $Co_{Fe}' - V_O^{\bullet\bullet}$ pinning centers.

Relative to the as-sintered sample, annealing in 10 atm O_2 results in facilitated polarization switching (Figure 4.10), with small changes observed in the electrical conductivity (Figure 4.11c). Considering that the p-type conductivity in BFO is dominated by $Fe_{Fe}^{\bullet}$, this conductivity behavior indicates that the concentration of $Fe_{Fe}^{\bullet}$ was only subtly affected by the annealing in 10 atm O_2. Assuming a quasi-constant concentration of $Fe_{Fe}^{\bullet}$ and V_{Bi}''', the latter fixed at the sintering conditions, the concentration of Co_{Fe}' must

have been reduced in order to satisfy the charge-neutrality condition (eq. (4.5)) as the concentration of $V_O^{\bullet\bullet}$ has been decreased. This suggests that Co^{2+} is (partially) oxidized to Co^{3+} (eq. (4.3) shifted to the left). Furthermore, this scenario is in agreement with the EPR results (Figure 4.17), which show a reduced concentration of $Co'_{Fe} - V_O^{\bullet\bullet}$ complexes after annealing in 10 atm O_2. Finally, considering the totality of the results, it can be concluded that pinching (hardening) in 1.5 at.% Co-doped ceramics, as evidenced by the high-field polarization hysteresis loops, is dominated by $Co'_{Fe} - V_O^{\bullet\bullet}$ defect complexes.

To sum up, the results on 1.5 at.% Co-doped BFO ceramics indicate that the p-type conductivity is dominated by $Fe_{Fe}^{\bullet}$. However, the polarization switching behavior and piezoelectric properties under resonance conditions suggest that $Co'_{Fe} - V_O^{\bullet\bullet}$ complexes play the key role in the hardening of BFO.

We point out that qualitatively similar behavior as found in 1.5 at.% Co-doped ceramics was also observed in the composition containing 0.25 at.% Co, discussed in Chapter 4.2.2, and also in 0.5 and 1.0 at.% Co-doped ceramics (see Appendix A). These results imply that the proposed conductivity and pinning mechanisms are valid for the entire Co concentration range, i.e., 0.25–1.5 at.%.

4.5 Frequency-Dependent Converse Piezoelectric Response and Implications of p-type Conductive DWs

Previous studies, presented in the introduction (Chapter 1.2.3), revealed an unusually large nonlinear piezoelectric response in BFO ceramics at low-driving-field frequencies (typically in the Hz to mHz region). The authors assumed that this nonlinear response is associated with conductive DWs that move irreversibly at low driving frequencies together with the hopping charges ($Fe_{Fe}^{\bullet}$) that are responsible for the local DW conductivity [93], [95].

The results of this PhD study on Co-doped BFO ceramics demonstrate that the increased dopant concentration results in a higher concentration of the compensating p-type charge carriers, responsible for the DW conductivity. It is naturally assumed that both the conductivity of individual DWs and the total fraction of DWs will increase with Co concentration. This provides a unique opportunity to test the DW displacements at low frequencies in samples with different fractions of conductive DWs.

In order to obtain an insight into the influence of the fraction of conductive DWs on piezoelectric nonlinearity, the converse piezoelectric response under sub-switching conditions was studied in 0.25 and 1.5 at.% Co-doped BFO, as most observable differences are expected.

Following the concepts from hard PZT, where frequency-independent piezoelectric coefficient was reported [10], one would initially assume that a stronger pinning of DWs and thus lower nonlinearity would occur in the sample with the higher concentration of pinning centers, i.e., in 1.5 at.% Co BFO. However, as it will be shown next, the PZT hardening concepts are clearly not valid for BFO ceramics.

4.5.1 Link between Co concentration and fraction of conductive DWs

Figure 4.18 shows the results of the local conductivity analyzed by c-AFM, combined with PFM analysis, on as-sintered samples of 0.25 and 1.5 at.% Co-doped BFO. Note that the PFM and c-AFM images and the results of the statistical analysis obtained on 1.5 Co were already presented in Chapter 4.3.1 (as-sintered sample in Figure 4.14); however, for the sake of comparison and clarity, the results are shown again.

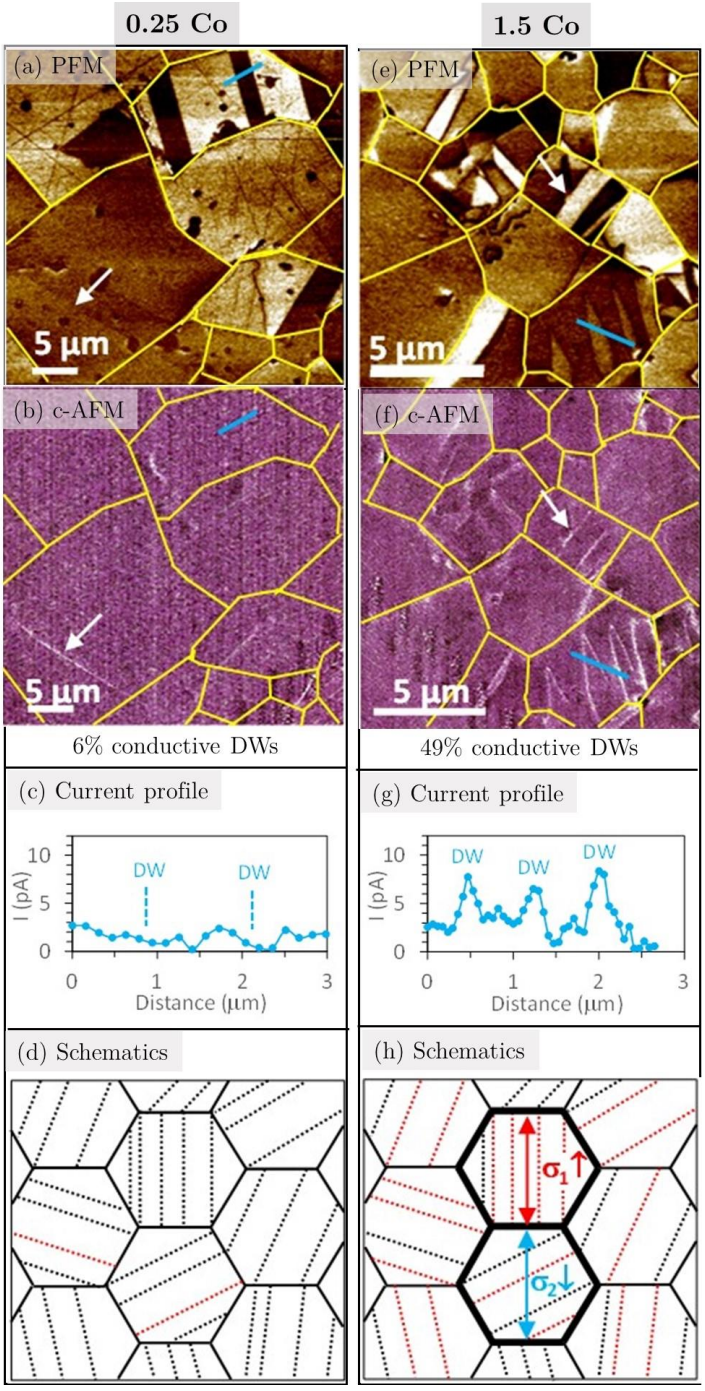

Figure 4.18: Local conductivity measurements on 0.25 and 1.5 at.% Co-doped BFO ceramics. (a,e) Out-of plane PFM amplitude and the corresponding (b,f) c-AFM images in 0.25 (left column) and 1.5 at.% Co (right) column sample. The grains in PFM and c-AFM images are for clarity encircled in yellow. The white arrows in PFM and c-AFM images denote examples of DW, where an enhanced current signal was observed, indicating an increased conductivity. The percentage number below the c-AFM image corresponds to the fraction of conductive DWs determined by probing 65 DWs in total. (c,g) show the electric-current profiles measured along the blue lines indicated in PFM and c-AFM images. (d,h) Schematic illustration of conductive DWs inside grains based on the c-AFM results. The full black lines indicate grain boundaries, the black dotted lines indicate DWs and the red

dotted lines indicate conductive DWs. The sample with 1.5 at.% Co exhibits a larger fraction of conductive DWs (~49 %), therefore higher local anisotropy in the electrical conductivity arises, resulting in observable differences in the conductivity between grains. Such an example is presented in (h), where σ_1 and σ_2 indicate the conductivity in the two grains measured along the vertical direction. The differences in the conductivity between the grains are associated with the different orientations of the conductive DWs in the grains. The local anisotropy in the electrical conductivity is much lower in 0.25 at.% Co-doped sample presented in (d) since a low fraction of conductive DWs (~6 %) was found in this composition.

The sample regions, which were with PFM (Figure 4.18a,e) identified as DWs (an example is denoted by a white arrow), were subsequently analyzed in terms of local current measurements using c-AFM, shown in Figure 4.18b,f. The conductive DWs are clearly identified by an enhanced current signal, as it can be seen from the example denoted by white arrows in Figure 4.18b,f. In addition, the increased current signal is clearly confirmed by the c-AFM profiles shown in Figure 4.18c,g with the corresponding profile lines indicated with blue in PFM and c-AFM images. Comparing the c-AFM images of 0.25 and 1.5 Co sample, it can be clearly observed that 1.5 Co contains a larger fraction of conductive DWs. This has been confirmed by performing statistical analysis at 65 DWs (not shown here) in several regions of both samples, which showed that only 6 % of the DWs were conductive in 0.25 Co, while 49 % in 1.5 Co. These results confirm that by increasing the p-type conductivity of BFO ceramics with Co introduction, the fraction of p-type conductive DWs increases as well.

The piezoelectric M-W effect reported in BFO was attributed to the anisotropy in the electrical conductivity, most probably arising from different orientations of the conductive DWs in different grains with respect to the external field axis [92], [95]. Considering those studies and results presented in Figure 4.18, it is assumed that the 1.5 Co sample will exhibit a strong piezoelectric M-W effect due to the high fraction of conductive DWs. A simplified illustration of the anisotropic effect is schematically presented in Figure 4.18h, highlighting a basic M-W unit composed of two grains with different conductivities measured in the vertical direction. Note that in this vertical direction the conductivity of the upper grain is higher than in the bottom grain as the DWs are oriented in the same (vertical) direction, providing a conductive path through the grain. Considering that the fraction of conductive DWs in 0.25 Co is very low (~6 %), there should be weak anisotropic effects in the conductivity from grain to grain, resulting in the absent (or weak) piezoelectric M-W effect.

4.5.2 Link between fraction of conductive DWs and DW dynamics

In order to evaluate the effect of conductive DWs on their dynamics under sub-switching conditions, the converse piezoelectric measurements were performed. The results are presented in Figure 4.19 as the weak-field piezoelectric d_{33} coefficient (Figure 4.19a) and tangent of the piezoelectric phase angle ($tan\,\delta$; Figure 4.19b) as a function of driving field frequency (f) and electric field amplitude (E_0). The arrows in Figure 4.19a,b denote increase of E_0 from 3.5 kV cm^{-1} (yellow curve) up to 16 kV cm^{-1} (black curve).

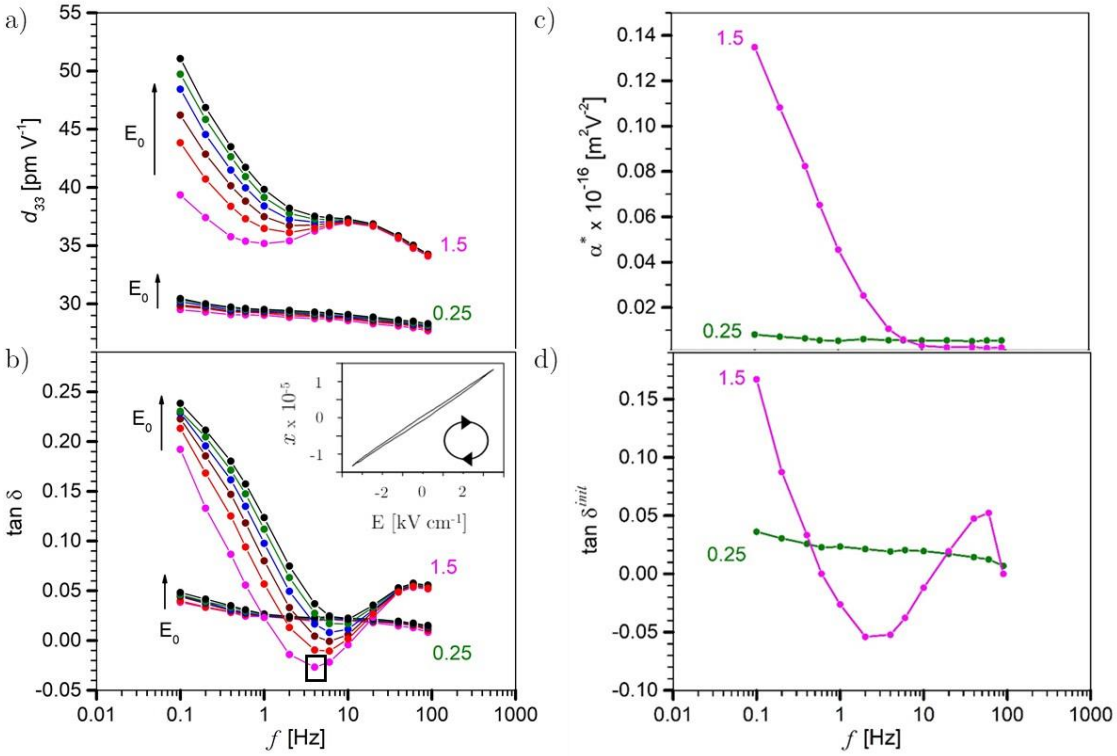

Figure 4.19: Domain-wall dynamics of Co-doped BFO under sub-switching conditions. a) Piezoelectric d_{33} coefficient and b) piezoelectric phase angle ($tan\,\delta$) as a function of frequency (f) and electric field amplitude (E_0) for 0.25 and 1.5 at.% Co-doped BFO. The arrows in (a,b) denote increase of E_0 from 3.5 kV cm^{-1} (yellow curve) up to 16 kV cm^{-1} (black curve) with increasing steps of 2.5 kV cm^{-1}. The inset in b) shows strain (x) as a function of electric field (E) measured at f=4 Hz and E_0=3.5 kV cm^{-1}. This measurement point is denoted by a black square in panel b) and indicates the measurement point where the negative piezoelectric phase angle was observed. c) The irreversible non-linear coefficient α^* calculated for the maximum E_0 of 16 kV cm^{-1} and d) piezoelectric $tan\,\delta^{init}$ extrapolated at$E_0 = 0$, both plotted as a function of frequency for the 0.25 and 1.5 Co sample. (For more details on the fitting procedure see Appendix A.)

The inspection of Figure 4.19 immediately reveals a distinctly different piezoelectric response of 0.25 and 1.5 at.% Co-doped BFO ceramics. The 0.25 at.% Co-doped sample shows no (or only weak) frequency dispersion and significant linearity of the d_{33} coefficient and $tan\,\delta$, i.e., little E_0 dependence (Figure 4.19a,b). On the other hand, the 1.5 at.% Co-doped sample exhibits strong frequency dispersion in the d_{33} coefficient and $tan\,\delta$, especially below ~10 Hz, where the dispersion becomes nonlinear, i.e., E_0 dependent (Figure 4.19a,b). The results obtained on 1.5 Co are consistent with previous reports on BFO, which showed that this low-frequency nonlinearity and nonlinear hysteresis arise from irreversible displacements of conductive DWs [92], [95].

The low-frequency nonlinearity and its relation with M-W effect can be described with the irreversible nonlinear coefficient α^*, extensively used in the frame of the Rayleigh law [162]:

$$d_{33}(E_0) = d_{33}^{init} + \alpha \cdot E_0 \tag{4.6}$$

where $d_{33}(E_0)$ and d_{33}^{init} correspond to the total (field-dependent) and initial coefficient (extrapolated at zero field), respectively. The coefficient α is the proportionality coefficient describing the slope of the linear dependence of the d_{33} coefficient on E_0 due to the irreversible displacement of the domain walls. It should be noted, however, that in the case of 1.5 at.% Co-doped sample, the d_{33} coefficient is not linearly dependent on E_0 (for more information see Appendix A). For this reason, we use the widely adopted field-dependent α^* and the nonlinearity (α^*) at maximum E_0 of 16 kV cm^{-1} is represented in Figure 4.19c.

The frequency-dependent $tan\,\delta^{init}$ shown in Figure 4.19d was determined by extrapolating the E_0-dependent $tan\,\delta$ to E_0=0. This parameter was used to evaluate the negative piezoelectric phase angle, where the displacement signal is in the time domain leading the electric-field signal, resulting in a clock-wise rotational sense of hysteresis loop (see inset of Figure 4.19b). This case is distinctly different from the more common positive piezoelectric phase angle, where the displacement signal is lagging the electric field signal, resulting in a counter-clockwise rotation of the hysteresis loop. The negative piezoelectric phase angle has been already reported in BFO ceramics and it has been shown that it is induced by internal electric field redistribution due to a large local anisotropy in the electrical conductivity and therefore the M-W effect [92], [95].

The 0.25 Co sample is characterized by nearly constant α^* in the whole frequency range (Figure 4.19c) and positive $tan\,\delta^{init}$ showing little frequency dispersion (Figure 4.19d). On the other hand, the 1.5 Co samples show the strong frequency dependence of α^* and $tan\,\delta^{init}$. The considerable increase of α^* at frequencies below 10 Hz in 1.5 Co suggests large irreversible DW displacements at low frequencies. This sample also clearly shows a negative phase angle in a wide frequency range (Figure 4.19b), confirming the M-W piezoelectric mechanism. Based on these experiments we may envisage that in the sample with large anisotropy (1.5 Co), at low frequencies the internal field will drop in a set of conductive grains (such as the upper grain in Figure 4.18h) and will be counterbalanced by an increase of the internal field in other grains of the ceramic matrix (such as the bottom grain in Figure 4.18h). It is this increase of the internal field that will promote DW displacements at low frequencies, leading to large macroscopic α^*.

To confirm the correlation between the Co concentration, i.e., the fraction of conductive DWs, and the low-frequency nonlinearity, the nonlinear piezoelectric measurements were also performed on the 0.5 and 1.0 Co samples. Figure 4.20 shows α^* as a function of f for all the Co-doped compositions. The α^* is nearly frequency-independent in 0.25 and 0.5 Co samples; however, the onset of the low-frequency nonlinearity becomes evident in 1.0 Co. This characteristic nonlinear behavior further increases in magnitude and shifts to higher frequencies in the 1.5 Co sample. These results clearly confirm the correlation between Co concentration, i.e., fraction of conductive DWs, and the strength of the low-frequency nonlinearity (related to enhanced DW displacements owing to the internal field redistribution mediated by conductive DWs).

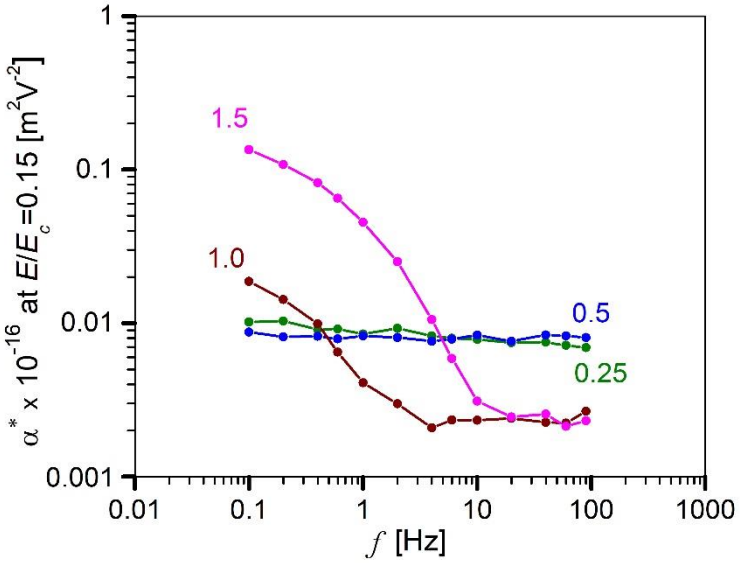

Figure 4.20: Irreversible nonlinear coefficient (α^*) as a function of driving field frequency (f) for BFO samples doped with 0.25, 0.5, 1.0 and 1.5 at.% Co. The field dependent α^* shown here was determined at 15 % of E_c of the individual composition in order to make a proper comparison. The values of E_c considered here were 40, 50, 70 and 90 kV cm^{-1} for 0.25, 0.5, 1.0 and 1.5 at.% Co, respectively.

To sum up, it has been shown that the increased dopant (Co) concentration leads to a larger fraction of conductive DWs due to a higher concentration of the p-type charge carriers (compensating the acceptor charges). It is naturally assumed that the higher dopant concentration will result in stronger pinning effects due to the higher concentration of pinning defects at the DWs. However, it has been shown that the sample with the highest Co concentration, i.e., 1.5 Co, exhibits the strongest low-frequency nonlinearity arising from large DW displacements.

Charge redistribution at the conductive DWs causes a redistribution of the internal field at low frequencies. The internal field will thus drop in a set of grains but, on the other hand, will increase in some other grains within the ceramic matrix. This increase of the internal field promotes the DW displacements, resulting in a significant non-linearity. That this is happening only at low driving frequencies clearly confirms the role of conductivity. In addition to the internal field redistribution, the DWs may become more mobile at low driving frequencies because their conductivity helps in the depinning from charged point defects such as holes [96].

4.6 Theoretical Investigation of the Point Defects in Co-Doped BFO Ceramics by DFT

We have so far provided a detailed experimental survey of the defect chemistry in Co-doped BFO (BFCO). To provide a fundamental understanding of how Co doping influences the defect chemistry, we next investigate the defect chemistry in BFO and BFCO using DFT calculations.

4.6.1 Stoichiometric BFO and BFCO

The lattice constants (a, c), electronic bandgap (E_g), magnetic moments on Fe (M_{Fe}) and Co (M_{Co}) atoms, and average Bader charges on the Fe and Co atoms in a DFT relaxed stoichiometric BFO (chemical formula $BiFeO_3$) and BFCO (chemical formula $Bi(Fe_{0.958}Co_{0.042})O_3$) supercells are summarized in Table 4.4. The results on BFO are in good agreement with earlier reports [75], [163], [164].

Table 4.4: Lattice constants a and c, bandgap E_g, spin magnetic moments on the Fe (M_{Fe}) and Co (M_{Co}) atoms and the average Bader charge on Fe and Co atom of stoichiometric BFO and BFCO.

	BFO	BFCO
a [Å]	5.553	-
c [Å]	13.748	-
E_g [eV]	2.15	1.39
M_{Fe} [μ_B]	4.1	4.1
M_{Co} [μ_B]	/	3.0
Fe Bader charge	1.75	1.75
Co Bader charge	/	1.59

Note that after introducing Co into BFO, the optimization of ionic positions was enabled; however, changes in cell shape and volume were not allowed due to the assumption that the defect concentration is low enough (close to the dilute limit) and it does not affect the volume of the cell. Therefore, this is the reason for not observing any chemical expansion/contraction by Co introduction.

Considering the literature data on BFO [68], [142] and the experimental results of this PhD study, we propose that Co acts as an acceptor dopant. According to the defect reaction in eq. (4.2), if Co^{2+} substitutes on the Fe^{3+} site in BFO, it should be charge compensated by $V_O^{\bullet\bullet}$. However, the concentration of $V_O^{\bullet\bullet}$ is closely related to the valence state of Fe through equation (1.6), thus the increased concentration of $V_O^{\bullet\bullet}$ by Co doping results in more Fe^{4+}, giving rise to p-type conductivity, which was confirmed by the Seebeck-coefficient measurements (see Chapters 4.2.2.3 and 4.2.3.3). Considering this, it might be concluded that some changes in the valence state of the Fe ions are expected by Co introduction, which is exactly what was observed by STEM/EELS analysis, where Fe^{4+} were identified in DW region of 1.5 at.% Co-doped as-sintered sample (Figure 4.15) .

To corroborate this, the electronic density of states (DOS) of BFO and BFCO was calculated (Figure 4.21). For undoped BFO (Figure 4.21a) we find a bandgap of 2.15 eV with the top of the valence band dominated by the occupied O $2p$ states, while unoccupied Fe $3d$ states dominate at the bottom of the conduction band. For BFCO, we calculate the electronic bandgap as the difference in the energy between the valence band maximum and

the defect state within the forbidden band gap, equal to 1.39 eV. Note, however, that the intrinsic band gap determined by the energy difference between O $2p$ states and the Fe $3d$ states is unchanged by the introduction of co-dopants.

Finally, the defect state in the bandgap consists mainly of Co $3d$ and O $2p$ states with no significant Fe $3d$ character. These results indicate that there are no significant changes in the valence state of Fe by Co introduction, which is in contrast to expectations (see eq. (4.2) and (1.6)). Note, however, that the unoccupied defect state in the bandgap corresponds to a deep acceptor state and p-type like conductivity, which is in agreement with our previous assumptions.

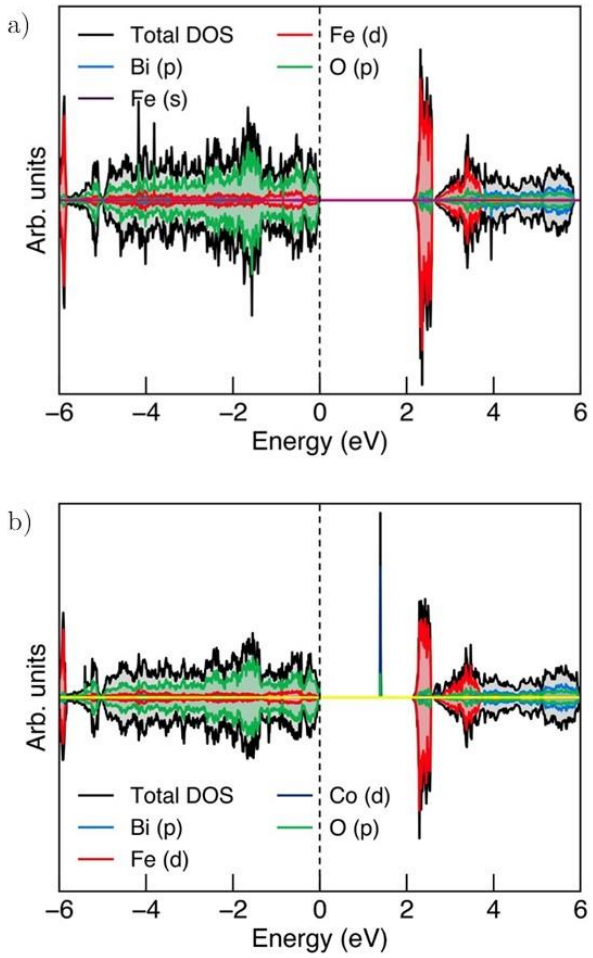

Figure 4.21: Density of states (DOS) for stoichiometric a) BFO and b) BFCO. The dashed black line denotes the Fermi level. The band gap for BFCO reported in Table 4.4 is calculated as the energy difference between the valence band maximum and the defect state within the band gap in b).

4.6.2 Defect cells

4.6.2.1 Defect clustering in BFCO

In order to evaluate if Co is an acceptor or a donor dopant, we next investigate the tendency of V_{Bi}''' and $V_O^{\bullet\bullet}$ to form defect complexes with Co. We assume that Co acts as

an acceptor dopant, therefore, no significant tendency of Co-V_{Bi}''' clustering is expected from an electrostatic point of view (two acceptor defects are expected to repel each other). On the other hand, $V_O^{\bullet\bullet}$ is considered as donor defect, thus significant Co-$V_O^{\bullet\bullet}$ clustering is expected as one acceptor and one donor defect should be attracted to each other based on electrostatics.

Defect clustering was examined by introducing V_{Bi}''' and $V_O^{\bullet\bullet}$ at different distances from the Co atom and evaluating the total energy of the system. The segregation enthalpy (ΔE_{seg}), i.e., the relative energy of forming a defect far or close to Co, as a function of distance between $V_{Bi}'''/V_O^{\bullet\bullet}$ and the Co atom, is displayed in Figure 4.22. The calculated ΔE_{seg} for the closest V_{Bi}'''-Co and $V_O^{\bullet\bullet}$-Co distances was found to be +0.39 and -2.05 eV, respectively. While no clear trend between ΔE_{seg} and V_{Bi}'''-Co distance can be observed, we note that the ΔE_{seg} is in principle positive, implying that defect clustering is not favorable for the system. On the other hand, in case of $V_O^{\bullet\bullet}$ it is evident that the ΔE_{seg} is the lowest when $V_O^{\bullet\bullet}$ and Co are separated by the shortest distance with ΔE_{seg} of -2.05 eV indicating a strong driving force for clustering. In addition, the ΔE_{seg} is mainly negative in all cases, indicating that defect clustering is favorable for this system.

To summarize, these results imply that V_{Bi}''' and Co have no tendency for clustering, while $V_O^{\bullet\bullet}$ and Co show tendency to form defect complexes, which is consistent with assumptions that Co acts as acceptor dopant. More importantly, this is consistent with results of EPR analysis, where defect complexes consisting of $V_O^{\bullet\bullet}$ and Co'_{Fe} defects have been identified (see chapter 4.3.2.2).

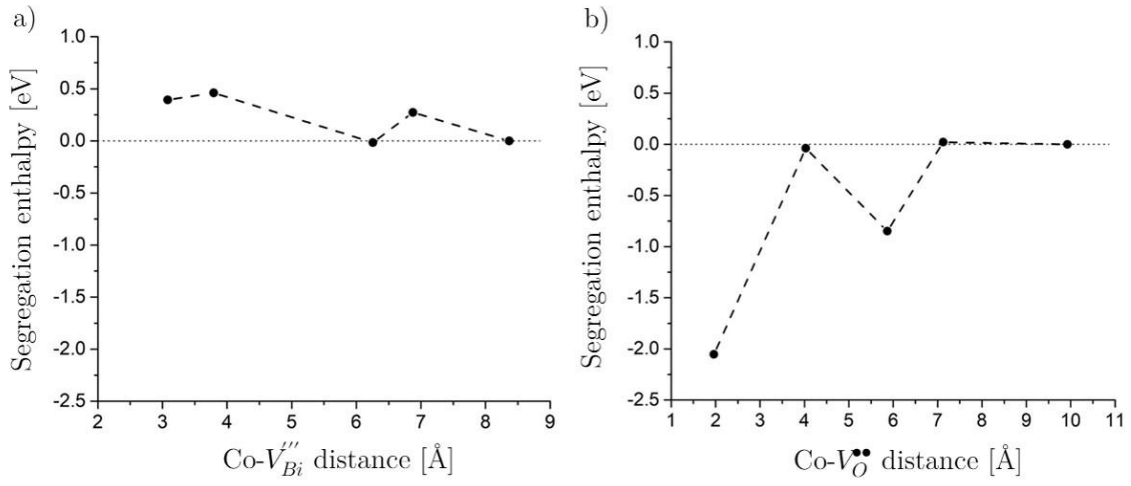

Figure 4.22: Segregation enthalpy as a function of distance between a) V_{Bi}''' and Co and b) $V_O^{\bullet\bullet}$ and Co in BFCO. The black dotted horizontal line corresponds to ΔE_{seg}=0 eV.

4.6.2.2 Electronic properties in defect cells of BFO and BFCO

We next investigated the effect of V_{Bi}''' and $V_O^{\bullet\bullet}$ on the electronic properties of BFO and BFCO. In the case of the latter, the closest Bi and O from the Co atom were removed.

The introduction of V_{Bi}''' in BFO gives rise to at least two unoccupied defect states within the band gap (Figure 4.23a), which show mainly Fe *d* character. This corresponds to deep acceptor states and p-type conductivity, in agreement with earlier theoretical studies [74], [75]. Furthermore, the indication of p-type behavior is in agreement with experimental observations and proposed defect model for BFO-based materials [49], [52], [148]. However, the Bader charge analysis did not reveal any observable changes in the

average charge on Fe atoms thus the charge compensation mechanism is not completely clear in this case.

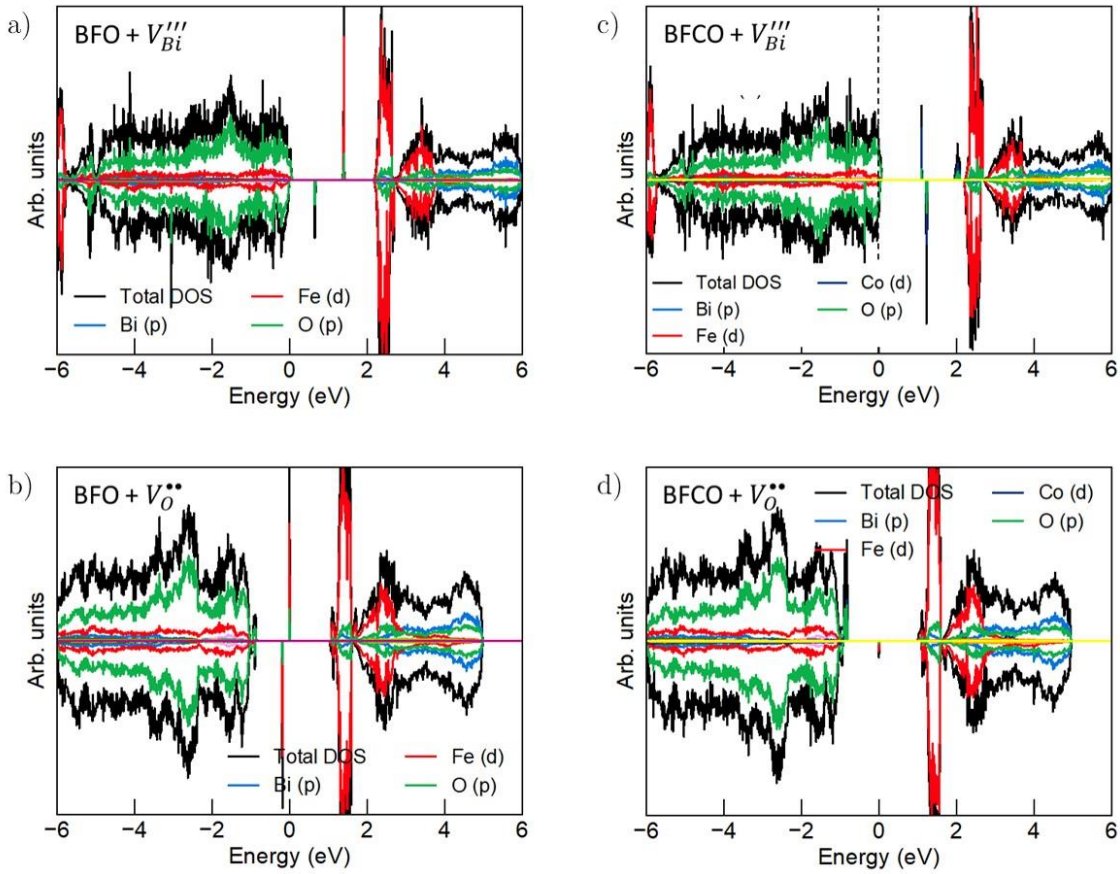

Figure 4.23: Density of states (DOS) for BFO with one a) V_{Bi}''' and b) $V_O^{\bullet\bullet}$ defect and for BFCO with one c) V_{Bi}''' and d) $V_O^{\bullet\bullet}$.

The donor behavior of $V_O^{\bullet\bullet}$ in BFO is corroborated by the presence of two occupied defects states with opposite spin within the bandgap (Figure 4.23b), showing mainly Fe d character, which indicates n-type like behavior by reducing two Fe^{3+} into two Fe^{2+}. This is confirmed by a reduction of the Bader charges for two Fe atoms surrounding the $V_O^{\bullet\bullet}$ from 1.74 to 1.30, accompanied by a decrease in the magnetic moments from 4 μ_B to 3.6 μ_B. These results are consistent with the literature [74], [75] and with the defect reaction in eq. (1.5).

The introduction of V_{Bi}''' in BFCO (Figure 4.23c) results in at least two unoccupied defect states in the band gap, in qualitative agreement with V_{Bi}''' in BFO (Figure 4.23a), indicating p-type conductivity through deep acceptor states. Note, however, that the relative positions of the defect states are changed, and that the defect states are now of mainly Co 3d character, as well as some Fe 3d and O 2p character. This suggests that the holes are localized mainly on the Co atom rather than on surrounding Fe atoms, which is further confirmed by the unperturbed Bader charges and magnetic moments on Fe.

The introduction of $V_O^{\bullet\bullet}$ in BFCO (Figure 4.23d) results in one occupied state in the band gap, consisting of mainly Fe 3d and O 2p character, suggesting n-type conductivity through the reduction of one Fe^{3+} into one Fe^{2+}. While the charge compensation mechanism for BFCO from the DOS in Figure 4.21b was inconclusive, as described above, we still assume that Co is an acceptor dopant with the formal charge of Co^{2+}, introducing one hole

into the system. On the other hand, the formation of $V_O^{\bullet\bullet}$ introduces two electrons, as evident from the DOS in Figure 4.23b. Hence, one extra electron is needed in order to charge compensate and this requirement is satisfied by reducing one Fe^{3+} into Fe^{2+}, as described in eq. (1.5). Therefore, the results in Figure 4.23d give a strong indication that Co indeed acts as a monovalent acceptor dopant, i.e., Co'_{Fe}.

4.6.2.3 Defect formation energies in BFO and BFCO

In the next step we calculated the defect formation energies (E^f_{def}) of V'''_{Bi} and $V_O^{\bullet\bullet}$ in BFO and BFCO under oxygen-rich conditions (see Table 4.5). We found that in BFO, the E^f_{def} for V'''_{Bi} is lower than for $V_O^{\bullet\bullet}$, demonstrating that V'''_{Bi} are the prevailing defects in oxygen-rich conditions, which is consistent with the literature [74]. The E^f_{def} for V'''_{Bi} is lower than E^f_{def} for $V_O^{\bullet\bullet}$ also in BFCO; however, it should be noted the E^f_{def} for both defects are very comparable, which is in contrast to observations from undoped BFO. Note that the existence of V'''_{Bi} in 1.5 at.% Co-doped BFO ceramics was experimentally demonstrated by STEM analysis (chapter 4.3.2.1).

Table 4.5: The total energy of stoichiometric BFO and BFCO with defect formation energy (E^f_{def}) of V'''_{Bi} and $V_O^{\bullet\bullet}$ under oxygen rich conditions. The difference in defect formation energy between BFCO and BFO ($E^f_{BFCO} - E^f_{BFO}$) is given as well.

System	BFO		BFCO		Difference
	Energy [eV]	E^f_{def} [eV]	Energy [eV]	E^f_{def} [eV]	$E^f_{BFCO} - E^f_{BFO}$ [eV]
Stoich.	-803.13	-	-800.23	-	-
V'''_{Bi}	-793.47	2.12	-790.32	2.37	+0.25
$V_O^{\bullet\bullet}$	-794.27	3.45	-792.29	2.53	-0.92

Moreover, we calculated the difference between E^f_{def} for V'''_{Bi} and $V_O^{\bullet\bullet}$ formation in BFCO and BFO (Table 4.5). It is clear that the formation of $V_O^{\bullet\bullet}$ is energetically more favored in BFCO than in BFO. Therefore, these results indicate that the formation of $V_O^{\bullet\bullet}$ is promoted by Co introduction. This is consistent with an increase of the pinching with Co concentration (Figure 4.4) since $V_O^{\bullet\bullet}$ act as strong pinning centers [16], [23]. On the other hand, it appears that the formation of V'''_{Bi} becomes less favorable with Co-doping, which is consistent with XPS studies on Co-doped ceramics [142]. The study showed that Co doping inhibits the reduction of BFO by reducing Co^{3+} into Co^{2+} rather than forming Fe^{2+} and BiO.

To summarize, the results of the DFT calculations on BFCO show that $V_O^{\bullet\bullet}$ tend to be as close as possible to Co. Therefore, this confirms that Co acts as acceptor when introduced to BFO, i.e., Co'_{Fe}, as two defects with different charges are expected to attract each other. This is further confirmed with results on V'''_{Bi}, where no affinity to the Co atom was found. Finally, our calculations revealed that the formation of $V_O^{\bullet\bullet}$ is energetically favored in BFCO compared to BFO, confirming the acceptor role of Co (see eq. (4.2)). This is in agreement with the increase of conductivity and pinching with the Co concentration (Chapter 4.2.1). In addition, the tendency of $V_O^{\bullet\bullet}$ and Co'_{Fe} to form defect complexes is also supported by the EPR results (presented in Chapter 4.3.2.2).

Chapter 5

Summary and Conclusions

In the first part of the PhD thesis we investigated the influence of Co concentration on the structural and functional properties of $Bi(Fe_{1-x}Co_x)O_3$ ceramics, where x=0, 0.25, 0.5, 1.0 and 1.5. The results can be summarized as follows:

- All the compositions exhibit a low (<1 wt%) and comparable amount of secondary sillenite phase. We found that Co introduction affects the grain growth; however, as no dopant or secondary-phase segregation was identified by STEM/EELS analysis on the grain boundaries, the inhibited grain growth in ceramics with a high Co concentration (1 and 1.5 at.%) is probably associated with doping-related point defects.
- We showed that the electrical conductivity and hardening, as observed from the domain-switching behavior and the piezoelectric response, increases with Co concentration, which was attributed to the increased concentration of $V_O^{\bullet\bullet}$ and $Fe_{Fe}^{\bullet}$. Based on these observations, we concluded (and subsequently confirmed) that Co acts as acceptor, i.e., $Co_{Fe}^{'}$.

Next, we investigated the influence of annealing atmosphere on the domain switching and electrical conductivity in Co-doped BFO ceramics. The conclusions are:

- We showed that post-annealing in 10 atm O_2 facilitates domain switching, while the domain switching is impeded after annealing in N_2. These changes were attributed to the decreased or increased concentration of $V_O^{\bullet\bullet}$, respectively. We concluded that $V_O^{\bullet\bullet}$ act as strong pinning centers in Co-doped BFO.
- The electrical conductivity decreases after post-annealing in N_2, demonstrating the p-type conductivity. This decrease of the conductivity was attributed to a reduced concentration of Fe^{4+} (reduction of Fe^{4+} into Fe^{3+}). However, dielectric spectroscopy data gave an indication of the relaxation process. This was ascribed to local differences in the electrical conductivity, i.e., M-W relaxation, due to a local reduction in the N_2 and thus an uneven distribution of Fe^{4+}.
- *In-situ* measurements of AC conductivity as a function of temperature and annealing atmosphere showed a decrease in the conductivity in N_2 and features of M-W relaxation, consistent with measurements at room temperature.
- The Seebeck coefficient was positive across the whole temperature range when annealing in both air and N_2, demonstrating the p-type conductivity and confirming that Fe^{4+} are the major charge carriers. Furthermore, upon cooling in N_2, the magnitude of the Seebeck coefficient significantly increased at lower temperatures (<~350 °C), which was attributed to inhomogeneous reduction during annealing in N_2.

- The fast redox kinetics upon isothermally switching the atmosphere between O_2 and N_2 gave an indication of the local redox reactions.

In the last part of the thesis, we investigated the location and type of point defects responsible for the elevated electrical conductivity and hardening in Co-doped BFO ceramics. The conclusions are:

- The c-AFM analysis showed enhanced conductivity of the DWs in as-sintered samples; however, these local regions were on average less conductive after annealing in N_2, indicating the local reduction of Fe^{4+} into Fe^{3+}. This correlates well with M-W relaxation, observed by several measurements (dielectric at RT, *in-situ* AC, Seebeck and DC, fast redox kinetics).
- The investigation of DWs with STEM/EELS analysis confirmed the presence of V_{Bi}''' and $Fe_{Fe}^{\bullet}$ in the as-sintered sample, while the N_2-annealed sample showed V_{Bi}''' and Fe^{3+} states at the DW, implying the local reduction of Fe^{4+} into Fe^{3+} during N_2 annealing
- The $Co_{Fe}' - V_O^{\bullet\bullet}$ defect complexes were identified by EPR. Furthermore, we showed that their concentration decreases when annealing in 10 atm O_2 and increases when annealing in N_2, as expected
- Our DFT calculations on Co-doped BFO showed that $V_O^{\bullet\bullet}$ tend to be as close as possible to Co and thus gave a strong indication that Co acts as acceptor, i.e., Co_{Fe}'. The formation of $Co_{Fe}' - V_O^{\bullet\bullet}$ defect complexes is in agreement with the EPR results. Furthermore, we found that the formation of $V_O^{\bullet\bullet}$ is energetically more favored in Co-doped BFO than in BFO, confirming the acceptor role of Co and explaining the increase of conductivity and pinching with increasing Co concentration (due to increased concentration of $Fe_{Fe}^{\bullet}$ and $V_O^{\bullet\bullet}$, respectively).

In addition, we thoroughly investigated the effect of Co on the frequency and field-dependent converse piezoelectric response. Surprisingly, we found that the ceramics with the highest concentration of Co (1.5 at.%), which contains the highest concentration of pinning centers ($Fe_{Fe}^{\bullet}$ and $V_O^{\bullet\bullet}$), exhibited the strongest low-frequency nonlinearity arising from large DW displacements. We attributed this effect to the local anisotropy in the electrical conductivity, arising from different orientations of conductive DWs in different grain families with respect to the direction of applied field, which causes the redistribution of internal fields inside the grains during field driving. The internal field reduced in a set of grains and increased in other grains. It is this internal-field increase that promotes the DW displacements, resulting in a significant non-linearity at low driving frequencies.

Finally, the results of this study show that the p-type conductivity and the piezoelectric nonlinearity in Co-doped BFO are dominated by $Fe_{Fe}^{\bullet}$. On the other hand, the hardening behavior is dominated by $Co_{Fe}' - V_O^{\bullet\bullet}$ defect complexes.

Appendix A

Appendix

A.1 Electrical Properties of Undoped BFO Ceramics

The electrical properties of undoped BFO, including P-E hysteresis loop, impedance (Z), angle between the current and the voltage (θ) and real part of electrical conductivity (σ') are shown in Figure A.1.

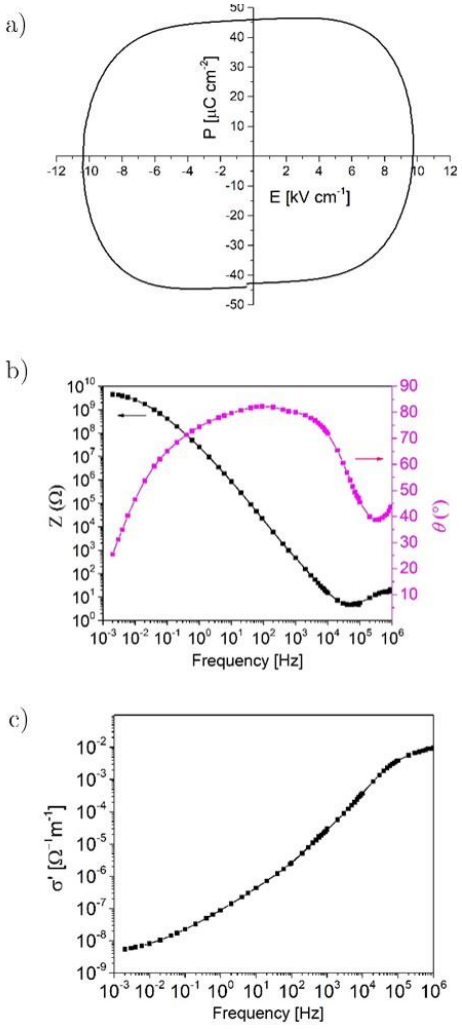

Figure A.1: Electrical properties of undoped BFO ceramics. a) P-E hysteresis loop measured at 100 Hz and 10 kV cm^{-1}, b) impedance (Z) together with phase angle (θ) and

c) real part of electrical conductivity (σ'), as a function of driving-field frequency. The electric field amplitude for the dielectric measurements was 0.02 kV cm^{-1}.

The *P-E* loop (Figure A.1a) is dominated by a high leakage-current, which is evident from the rounded shape of the loop. The real part of dielectric permittivity shows relaxation, observed as a step-like feature, which is accompanied by a peak in $tan\,\delta$ (Figure A.1b). This relaxation results in apparently high values of ε' at the low-frequency end (Figure A.1c). The relaxation is most likely associated with the Maxwell-Wagner effect arising due to local differences in the electrical conductivity, which are known to dominate the response of unmodified BFO [150]

A.2 Influence of Annealing Atmosphere on 0.5 and 1.0 at.% Co-Doped BFO Ceramics

In order to confirm a qualitatively comparable behavior of all the Co-doped compositions used in this PhD study, *in-situ* measurements of the AC conductivity and Seebeck coefficient as a function of temperature and annealing atmosphere, i.e., in synthetic air and N_2, were performed on 0.5 and 1.0 at.% Co-doped BFO. The results are presented in Figure A.2, with the same labelling as used for 0.25 and 1.5 at.% Co (chapters 4.2.2.3 and 4.2.3.3), thus the curves 1, 2 and 3 refer to cooling cycle in air, heating cycle in N_2 and cooling cycle in N_2, respectively.

Figure A.2a,e show that no changes in the measured conductivity can be observed during heating in N_2 (curve 2) up to ~550°C if compared to the measurement in air (curve 1). However, during cooling in N_2 (curve 3), the conductivity decreases and remains lower with respect to that in air (curve 1) down to 150°C. These results demonstrate a decrease of the conductivity in both compositions after annealing in air, which is in line with the p-type conductivity and is qualitatively the same as observed in 0.25 and 1.5 Co compositions (see Figure 4.9 and Figure 4.12 in chapters 4.2.2.3 and 4.2.3.3, respectively).

From the real part of the dielectric permittivity presented in Figure A.2b,f, a strong increase in ε' during cooling in N_2 (curve 3) can be observed, accompanied by peaks in $tan\,\delta$ (indicated by green arrows in Figure A.2c,g, curve 3). As has been already suggested in relation with 0.25 and 1.5 Co compositions, we assume this relaxation is of a M-W origin associated with the local (inhomogeneous) reduction and thus local differences in the electrical conductivity inside the sample.

The Seebeck coefficient in Figure A.2d,h remains positive during measurements in air and N_2 in both compositions, demonstrating the p-type behavior where Fe^{4+} are the major charge carriers. However, the magnitude of the Seebeck coefficient significantly increases during cooling in N_2 at lower temperatures (indicated by the green oval), consistent with observations from 0.25 and 1.5 Co (see Figure 4.9 and Figure 4.12). Such behavior has been explained by the inhomogeneous reduction in N_2, resulting in a composite-like (M-W) effect (more details can be found in Chapter 4.2.2.3).

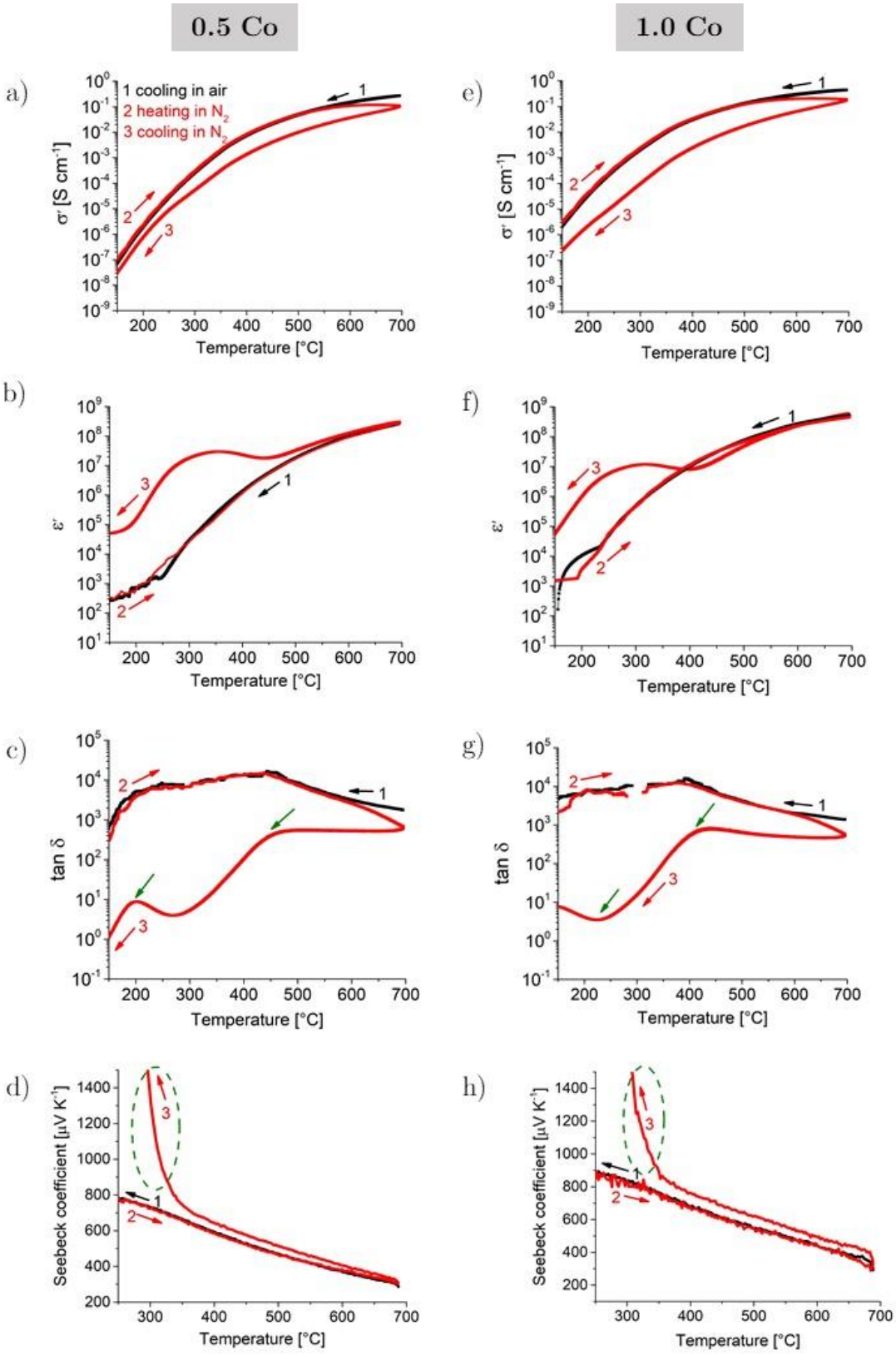

Figure A.2: (a,e) σ' , (b,f) ε', (c,g) $tan\,\delta$ and (d,h) Seebeck coefficient as a function of temperature and annealing atmosphere for 0.5 (left column) and 1.0 (right column) at.% Co-doped BFO ceramics. Curves 1, 2 and 3 correspond to cooling in air (first cycle), heating in N_2 and cooling in N_2, respectively. Green arrows in (c,g) indicate peaks in $tan\,\delta$, while

dashed green oval in (d,h) marks the increase of Seebeck coefficient at lower temperatures upon cooling in N_2.

A.3 Field and Frequency Dependence of Piezoelectric Response in Co-Doped BFO Ceramics

The electric field amplitude (E_0) dependence of piezoelectric d_{33} coefficient and piezoelectric phase angle ($tan\,\delta$) for 0.25 and 1.5 at.% Co-doped BFO ceramics measured at several frequencies is displayed in Figure A.3.

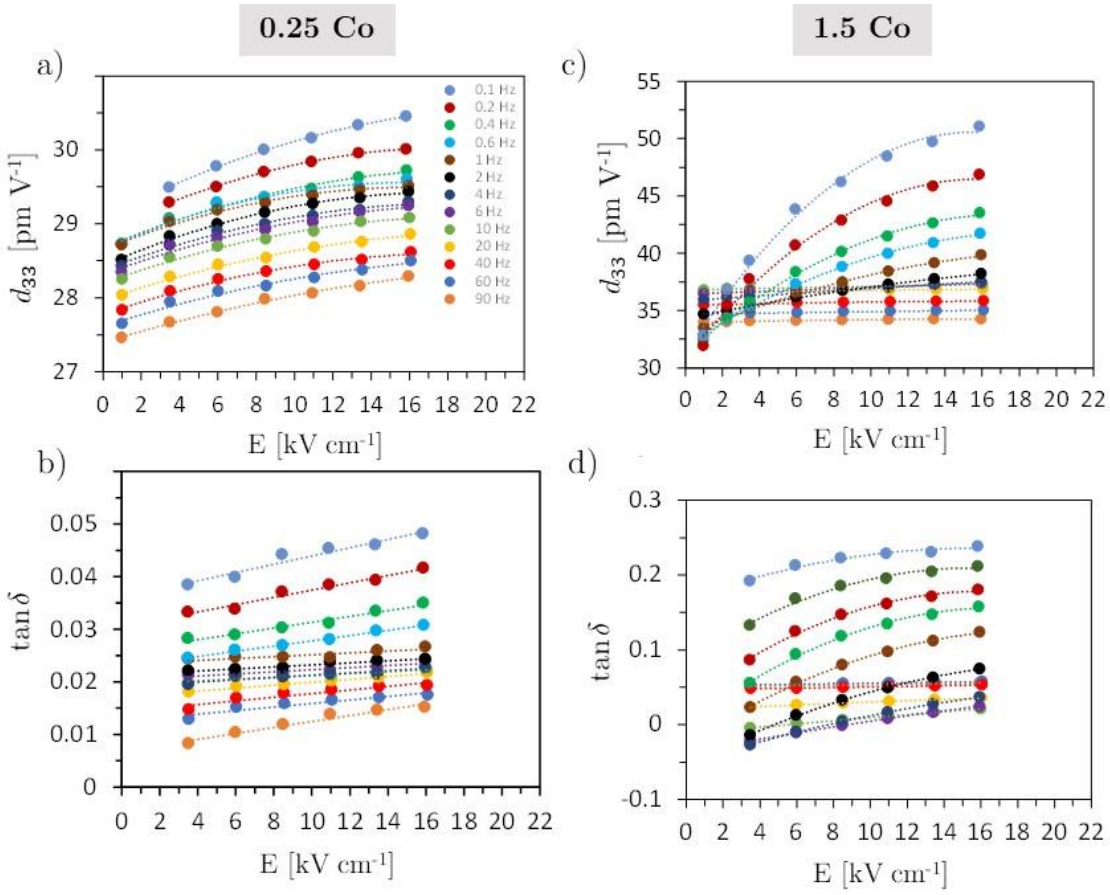

Figure A.3: Piezoelectric d_{33} coefficient (a,c) and piezoelectric phase angle ($tan\,\delta$) (b,d) dependence on electric field amplitude (E_0) in 0.25 (left panel) and 1.5 (right panel) at.% Co-doped BFO ceramics measured at several frequencies (see notations in panel a)). The data were fitted with a second-order polynomial function with the exception of the data shown in b), where a linear function was used, since no corresponding polynomial relationship was found in this case.

The irreversible coefficient α^*, used to identify the fingerprint of the piezoelectric M-W effect (Figure 4.19c), was extracted from the d_{33} data in Figure A.3a,c using Rayleigh law [162]:

$$d_{33}(E_0) = d_{33}^{init} + \alpha \cdot E_0 \tag{5.1}$$

where $d_{33}(E_0)$, d_{33}^{init}, α and E_0 correspond to total d_{33} coefficient, reversible Rayleigh coefficient, irreversible Rayleigh coefficient and electric field amplitude, respectively. However, the dependence of d_{33} on E_0 is not linear (see Figure A.3a,c), which means that the α in eq. (5.1) is not constant. The Rayleigh law is then modified by using the polynomial approach, where the field-independent α is replaced by field-dependent irreversible coefficient denoted for this occasion as α^* [162]:

$$d_{33}(E_0) = d_{33}^{init} + \alpha^* \cdot E_0 \tag{5.2}$$

where

$$\alpha^*(E_0) = \alpha_1 + \alpha_2 \cdot E_0 + \alpha_3 \cdot E_0^2 + \cdots \tag{5.3}$$

In eq. (5.3), α_1, α_2 and α_3 are the individual coefficients of the polynomial extension of the irreversible Rayleigh coefficient α^*.

The d_{33} dependence on E_0 was fitted using eq. (5.2) with a second order polynomial, thus corresponding to $\alpha_n = 0$ for $n \geq 3$ in eq. (5.3). The fitted α_n values ($n = 1,2$) were then used to calculate α^* at E_0 of 16 kV cm^{-1}, which is shown for comparison in Figure 4.19c.

The frequency-dependent $tan\,\delta^{init}$ shown in Figure 4.19d was obtained by fitting the $tan\,\delta$ dependence on E_0 (see Figure A.3b,d) and by extracting the zero-field $tan\,\delta^{init}$ [92]:

$$tan\,\delta\,(E_0) = \ tan\,\delta^{init} + a \cdot E_0 + b \cdot E_0^2 + \cdots \tag{5.4}$$

where a and b represent the coefficients of the fitting polynomial function.

References

[1] G. H. Haertling, "Ferroelectric ceramics: History and technology," *J. Am. Ceram. Soc.*, vol. 82, pp. 797–818, 1999.

[2] L. E. Cross, "Ferroelectric Ceramics: tailoring properties for specific applications," in *Ferroelectric Ceramics*, N. Setter and E. L. Colla, Eds. Basel, 1993, pp. 1–86.

[3] R. Tazaki, D. Fu, M. Itoh, and M. Daimon, "Lattice distortion under an electric field in $BaTiO_3$ piezoelectric single crystal," *J. Phys. Condens. Matter*, vol. 21, no. 215903, 2009.

[4] H. Jaffe, B., Cook, W.R.J., Jaffe, *Piezoelectric Ceramics*, US. New York: Academic Press, 1971.

[5] D. M. Smyth, *The Defect Chemistry of Metal Oxides*, First. London: Oxford University Press, 2000.

[6] M. Morozov, "Softening and Hardening Transitions in Ferroelectric $Pb(Zr,Ti)O_3$ Ceramics," vol. 3368, 2005.

[7] D. Damjanovic, N. Klein, J. Li, and V. Porokhonskyy, "What can be expected from lead-free piezoelectric materials?," *Funct. Mater. Lett.*, vol. 3, no. 1, pp. 5–13, 2010.

[8] J. E. García, R. Ṕrez, D. A. Ochoa, A. Albareda, M. H. Lente, and J. A. Eiras, "Evaluation of domain wall motion in lead zirconate titanate ceramics by nonlinear response measurements," *J. Appl. Phys.*, vol. 103, no. October 2007, 2008.

[9] S. Takahashi and M. Takahashi, "Effects of impurities on the mechanical quality factor of lead zirconate titanate ceramics," *Jpn. J. Appl. Phys.*, vol. 11, pp. 31–35, 1972.

[10] D. Damjanovic, *Hysteresis in piezoelectric and ferroelectric materials*, vol. 3. 2006.

[11] L. Eyraud, B. Guiffard, L. Lebrun, and D. Guyomar, "Interpretation of the softening effect in PZT ceramics near the morphotropic phase boundary," *Ferroelectrics*, vol. 330, no. June 2013, pp. 51–60, 2006.

[12] Y. Xu, *Ferroelectric materials and their applications*. Amsterdam: Elsevier Science, 1991.

[13] R. Gerson, "Variation in ferroelectric characteristics of lead zirconate titanate ceramics due to minor chemical modifications," *J. Appl. Phys.*, vol. 31, no. 1960, pp. 188–194, 1960.

[14] R. A. Eichel, H. Mestric, H. Kungl, and M. J. Hoffmann, "Multifrequency electron paramagnetic resonance analysis of polycrystalline gadolinium-doped $PbTiO_3$ — Charge compensation and site of incorporation," *Appl. Phys. Lett.*, vol. 88, no. 122506, 2006.

[15] G. Arlt and H. Neumann, "Internal bias in ferroelectric ceramics: Origin and time

dependence," *Ferroelectrics*, vol. 87, no. 1, pp. 109–120, 1988.

[16] A. Chandrasekaran, D. Damjanovic, N. Setter, and N. Marzari, "Defect ordering and defect-domain-wall interactions in $PbTiO_3$: A first-principles study," *Phys. Rev. B - Condens. Matter Mater. Phys.*, vol. 88, no. 21, pp. 1–9, 2013.

[17] K. Carl and K. H. Hardtl, "Electrical after-effects in $Pb(Zr,Ti)O_3$ ceramics," *Ferroelectrics*, vol. 17, pp. 476–486, 1978.

[18] Y. A. Genenko, J. Glaum, M. J. Hoffmann, and K. Albe, "Mechanisms of aging and fatigue in ferroelectrics," *Mater. Sci. Eng. B Solid-State Mater. Adv. Technol.*, vol. 192, no. C, pp. 52–82, 2015.

[19] L. X. Zhang and X. Ren, "In situ observation of reversible domain switching in aged Mn-doped $BaTiO_3$ single crystals," *Phys. Rev. B - Condens. Matter Mater. Phys.*, vol. 71, no. 17, pp. 1–8, 2005.

[20] U. Robels and G. Arlt, "Domain wall clamping in ferroelectrics by orientation of defects," *J. Appl. Phys.*, vol. 73, no. 7, pp. 3454–3460, 1993.

[21] L. Zhang and X. Ren, "Aging behavior in single-domain Mn-doped $BaTiO_3$ crystals: Implication for a unified microscopic explanation of ferroelectric aging," *Phys. Rev. B - Condens. Matter Mater. Phys.*, vol. 73, no. 9, 2006.

[22] P. V. Lambeck and G. H. Jonker, "The nature of domain stabilization in ferroelectric perovskites," *J. Phys. Chem. Solids*, vol. 47, no. 5, pp. 453–461, 1986.

[23] P. Erhart, P. Traskelin, and K. Albe, "Formation and switching of defect dipoles in acceptor-doped lead titanate: A kinetic model based on first-principles calculations," *Phys. Rev. B - Condens. Matter Mater. Phys.*, vol. 88, no. 2, pp. 1–10, 2013.

[24] P. Erhart, R. Eichel, P. Träskelin, and K. Albe, "Association of oxygen vacancies with impurity metal ions in lead titanate," *Phys. Rev. B*, vol. 76, no. 174116, pp. 1–12, 2007.

[25] P. Jakes, E. Erdem, R. Eichel, L. Jin, and D. Damjanovic, "Position of defects with respect to domain walls in Fe^{3+} -doped Pb $(Zr_{0.52}Ti_{0.48})O_3$ piezoelectric ceramics," vol. 72907, no. 2011, pp. 210–213, 2016.

[26] L. He and D. Vanderbilt, "First-principles study of oxygen-vacancy pinning of domain walls in $PbTiO_3$," *Phys. Rev. B*, vol. 68, no. 134103, pp. 1–7, 2003.

[27] Y. A. Genenko, "Drift of charged defects in local fields as aging mechanism in ferroelectrics," *Phys. Rev. B*, vol. 75, no. 184107, pp. 1–10, 2007.

[28] X. Ren, "Large electric-field-induced strain in ferroelectric crystals by point-defect-mediated reversible domain switching," *Nat. Mater.*, vol. 3, no. 2, pp. 91–94, 2004.

[29] E. Cockayne and B. P. Burton, "Dipole moment of a Pb-O vacancy pair in $PbTiO_3$," *Phys. Rev. B - Condens. Matter Mater. Phys.*, vol. 69, pp. 1–5, 2004.

[30] H. Meštrić, R. A. Eichel, K. P. Dinse, A. Ozarowski, J. Van Tol, and L. C. Brunel, "High-frequency electron paramagnetic resonance investigation of the Fe^{3+} impurity center in polycrystalline $PbTiO_3$ in its ferroelectric phase," *J. Appl. Phys.*, vol. 96, no. 12, pp. 7440–7444, 2004.

[31] H. Meštrić, R. a. Eichel, T. Kloss, K. P. Dinse, S. Laubach, S. Laubach, P. C. Schmidt, K. a. Schönau, M. Knapp, and H. Ehrenberg, "Iron-oxygen vacancy defect centers in $PbTiO_3$: Newman superposition model analysis and density functional calculations," *Phys. Rev. B - Condens. Matter Mater. Phys.*, vol. 71, pp. 1–10, 2005.

[32] D. J. Keeble, M. Loyo-Menoyo, Z. I. Y. Booq, R. R. Garipov, V. V. Eremkin, and V. Smotrakov, "Fe^{3+} defect dipole centers in ferroelectric $PbTiO^3$ studied using electron paramagnetic resonance," *Phys. Rev. B - Condens. Matter Mater. Phys.*, vol. 80, pp. 1–7, 2009.

[33] R. R. Garipov, J. M. Spaeth, and D. J. Keeble, "Measurement of Cu(II) copper defect dipoles in ferroelectric $PbTiO_3$ using electron-nuclear double resonance," *Phys. Rev. Lett.*, vol. 101, no. December, pp. 8–11, 2008.

[34] R. A. Eichel, P. Erhart, P. Träskelin, K. Albe, H. Kungl, and M. J. Hoffmann, "Defect-dipole formation in copper-doped $PbTiO_3$ ferroelectrics," *Phys. Rev. Lett.*, vol. 100, no. March, pp. 1–4, 2008.

[35] L. Zhang, E. Erdem, X. Ren, and R. A. Eichel, "Reorientation of $(Mn''_{Ti}\text{-}V^{\bullet\bullet}_{O})$ defect dipoles in acceptor-modified $BaTiO_3$ single crystals: An electron paramagnetic resonance study," *Appl. Phys. Lett.*, vol. 93, no. 2008, pp. 2006–2009, 2008.

[36] R. A. Maier, T. A. Pomorski, P. M. Lenahan, and C. A. Randall, "Acceptor-oxygen vacancy defect dipoles and fully coordinated defect centers in a ferroelectric perovskite lattice : Electron paramagnetic resonance analysis of Mn^{2+} in single crystal $BaTiO_3$," *Journal of Applied Physics*, vol. 164102, 2015.

[37] B. Tio, E. Aksel, E. Erdem, P. Jakes, J. L. Jones, R. Eichel, "Defect structure and materials ' hardening ' in Fe_2O_3-doped ferroelectrics," vol. 12903, pp. 10–13, 2010.

[38] R. Eichel, E. Erünal, P. Jakes, S. Körbel, C. Elsässer, and N. Nbo, "Interactions of defect complexes and domain walls in CuO-doped ferroelectric $(K,Na)NbO_3$ Interactions of defect complexes and domain walls in CuO-doped," vol. 242908, pp. 1–6, 2013.

[39] D. J. Keeble, S. Singh, R. A. Mackie, M. Morozov, S. Mcguire, and D. Damjanovic, "Cation vacancies in ferroelectric $PbTiO_3$ and $PbZrO_3$: A positron annihilation lifetime spectroscopy study," pp. 1–5, 2007.

[40] C. Slouka, T. Kainz, E. Navickas, G. Walch, H. Hutter, K. Reichmann, and J. Fleig, "The effect of acceptor and donor doping on oxygen vacancy concentrations in lead zirconate titanate (PZT)," *Materials (Basel).*, vol. 9, 2016.

[41] P. Taylor, G. Suchaneck, A. Deyneka, L. Jastrabik, and M. Savinov, "Ferroelectrics Lead Excess in $Pb(Zr,Ti)O_3$ Thin Films Deposited by Reactive Sputtering at Low Temperatures," no. October 2014, pp. 37–41.

[42] R. W. Whatmore, Z. Huang, and M. Todd, "Sputtered lead scandium tantalate thin films: Pb^{4+} in B sites in the perovskite structure," *J. Appl. Phys.*, vol. 82, no. 1997, pp. 5686–5694, 1997.

[43] W. L. Warren, K. Vanheusden, D. Dimos, G. E. Pike, and B. A. Tuttle, "Oxygen Vacancy Motion in Perovskite Oxides," *J. Am. Ceram. Soc.*, vol. 79, no. 2, pp. 536–38, 1996.

[44] M. I. Morozov and D. Damjanovic, "Charge migration in $Pb(Zr,Ti)O_3$ ceramics and its relation to ageing, hardening, and softening," *J. Appl. Phys.*, vol. 107, no. 3, pp. 0–10, 2010.

[45] J. J. Dih and R. M. Fulrath, "Electrical Conductivity in Lead Zirconate-Titanate Ceramics," no. July 1977, pp. 448–451, 1978.

[46] Y. P. Wang, L. Zhou, M. F. Zhang, X. Y. Chen, J. Liu, Z. G. Liu, Y. P. Wang, L.

Zhou, M. F. Zhang, X. Y. Chen, J. Liu, and Z. G. Liu, "Room-temperature saturated ferroelectric polarization in $BiFeO_3$ ceramics synthesized by rapid liquid phase sintering," vol. 1731, no. 2004, pp. 1–4, 2005.

[47] F. Chen, Q. F. Zhang, J. H. Li, Y. J. Qi, C. J. Lu, X. B. Chen, X. M. Ren, and Y. Zhao, "Sol-gel derived multiferroic $BiFeO_3$ ceramics with large polarization and weak ferromagnetism," *Appl. Phys. Lett.*, vol. 89, no. 2006, pp. 210–213, 2006.

[48] T. Rojac, A. Bencan, B. Malic, G. Tutuncu, J. L. Jones, J. E. Daniels, and D. Damjanovic, "$BiFeO_3$ Ceramics: Processing, Electrical, and Electromechanical Properties," *J. Am. Ceram. Soc.*, vol. 97, no. 7, pp. 1993–2011, Jul. 2014.

[49] E. T. Wefring, M. Einarsrud, and T. Grande, "Electrical conductivity and thermopower of (1-x)$BiFeO_3$-x$Bi_{0.5}K_{0.5}TiO_3$ (x = 0.1, 0.2) ceramics near the ferroelectric to paraelectric phase transition," *Phys. Chem. Chem. Phys.*, vol. 17, pp. 9420–9428, 2015.

[50] J. König, M. Spreitzer, B. Jancar, D. Suvorov, Z. Samardzic, and A. Popovic, "The thermal decomposition of $K_{0.5}Bi_{0.5}TiO_3$ ceramics," *J. Eur. Ceram. Soc.*, vol. 29, pp. 1695–1701, 2009.

[51] A. V Mikhailov, N. A. Gribchenkova, E. N. Kolosov, A. R. Kaul, and A. S. Alikhanyan, "Mass Spectrometric Investigation of Vaporization in the Bi_2O_3 – Fe_2O_3 System," *Russ. J. Phys. Chem. A*, vol. 85, no. 1, pp. 31–35, 2011.

[52] T. Rojac, A. Bencan, G. Drazic, N. Sakamoto, H. Ursic, B. Jancar, G. Tavcar, M. Makarovic, J. Walker, B. Malic, and D. Damjanovic, "Domain-wall conduction in ferroelectric $BiFeO_3$ controlled by accumulation of charged defects," *Nat. Mater.*, vol. 16, no. 3, 2017.

[53] K. Brinkman, T. Iijima, and H. Takamura, "The oxygen permeation characteristics of $Bi_{1-x}Sr_xFeO_3$ mixed ionic and electronic conducting ceramics," *Solid State Ionics*, vol. 181, no. 1–2, pp. 53–58, 2010.

[54] M. I. Morozov, M. Einarsrud, and T. Grande, "Control of conductivity and piezoelectric performance in bulk $Bi_{0.5}K_{0.5}TiO_3$-$BiFeO_3$," *Appl. Phys. Lett.*, vol. 104, no. 12, pp. 1–4, 2014.

[55] A. K. Pradhan, K. Zhang, D. Hunter, J. B. Dadson, G. B. Loiutts, P. Bhattacharya, R. Katiyar, J. Zhang, J. Sellmyer, U. N. Roy, Y. Cui, and A. Burger, "Magnetic and electrical properties of single- phase multiferroic $BiFeO_3$," *J. Appl. Phys.*, vol. 97, no. 93903, 2008.

[56] M. Kumar, K. L. Yadav, and G. D. Varma, "Large magnetization and weak polarization in sol – gel derived $BiFeO_3$ ceramics," *Mater. le*, vol. 62, no. 8–9, pp. 1159–1161, 2008.

[57] S. Hunpratub, P. Thongbai, T. Yamwong, R. Yimnirun, and S. Maensiri, "Dielectric relaxations and dielectric response in multiferroic $BiFeO_3$ ceramics," *Appl. Phys. Lett.*, vol. 94, no. December 2008, pp. 1–4, 2009.

[58] J. Prado-Gonjal, D. Ávila, M. E. Villafuerte-Castrejón, F. González-García, L. Fuentes, R. W. Gómez, J. L. Pérez-Mazariego, V. Marquina, and E. Morán, "Structural, microstructural and Mössbauer study of $BiFeO_3$ synthesized at low temperature by a microwave-hydrothermal method," *Solid State Sci.*, vol. 13, pp. 2030–2036, 2011.

[59] Y. P. Wang, L. Zhou, M. F. Zhang, X. Y. Chen, J.-M. Liu, and Z. G. Liu, "Room-temperature saturated ferroelectric polarization in $BiFeO_3$ ceramics synthesized by rapid liquid phase sintering," *Appl. Phys. Lett.*, vol. 84, no. 10, p. 1731, 2004.

[60] H. Ke, W. Wang, Y. Wang, H. Zhang, D. Jia, Y. Zhou, X. Lu, and P. Withers, "Dependence of dielectric behavior in $BiFeO_3$ ceramics on intrinsic defects," *J. Alloys Compd.*, vol. 541, pp. 94–98, 2012.

[61] E. Markiewicz, B. Hilczer, and M. B, "Dielectric properties of $BiFeO_3$ ceramics obtained from mechanochemically synthesized nanopowders," pp. 154–161, 2011.

[62] G. L. Yuan, Y. Yang, and S. W. Or, "Aging-induced double ferroelectric hysteresis loops in $BiFeO_3$ multiferroic ceramic," *Appl. Phys. Lett.*, vol. 91, no. 2007, pp. 2005–2008, 2007.

[63] K. H. Buschow, Ed., *Encyclopedia of materials: Science and tehnology*. Elsevier Science, 2001.

[64] M. I. Morozov, M. A. Einarsrud, and T. Grande, "Control of conductivity and electric field induced strain in bulk $Bi_{0.5}K_{0.5}TiO_3$-$BiFeO_3$ ceramics," *Appl. Phys. Lett.*, vol. 104, pp. 0–4, 2014.

[65] N. Masó and A. R. West, "Electrical Properties of Ca-Doped $BiFeO_3$ Ceramics: From p -Type Semiconduction to Oxide-Ion Conduction," *Chem. Mater.*, vol. 24, pp. 2127–2132, 2012.

[66] M. Schrade, N. Maso, A. Perejón, L. Perez-Maqueda, and A. R. West, "Defect chemistry and electrical properties of $BiFeO_3$," *J. Mater. Chem. C*, vol. 5, pp. 10077–10086, 2017.

[67] A. Perejón, N. Masó, A. R. West, P. E. Sánchez-Jiménez, R. Poyato, J. M. Criado, and L. A. Pérez-Maqueda, "Electrical Properties of Stoichiometric $BiFeO_3$ Prepared by Mechanosynthesis with Either Conventional or Spark Plasma Sintering," *J. Am. Ceram. Soc.*, vol. 96, no. 4, pp. 1220–1227, Apr. 2013.

[68] Y. Chiang, C. Tu, P. Chen, C. Chen, J. Anthoniappen, Y. Ting, T. Chan, and V. H. Schmidt, "Magnetic and phonon transitions in B-site Co doped $BiFeO_3$ ceramics," *Ceram. Int.*, vol. 42, no. 11, pp. 13104–13112, 2016.

[69] M. Zhang, H.-J. Yang, Y. Li, W.-Q. Cao, X.-Y. Fang, J. Yuan, and M.-S. Cao, "Cobalt doping of bismuth ferrite for matched dielectric and magnetic loss," *Appl. Phys. Lett.*, vol. 115, no. 212902, pp. 1–5, 2019.

[70] H. Hojo, K. Oka, K. Shimizu, H. Yamamoto, and R. Kawabe, "Development of Bismuth Ferrite as a Piezoelectric and Multiferroic Material by Cobalt Substitution," *Adv. Mater.*, vol. 30, no. 1705665, pp. 1–15, 2018.

[71] A. A. Belik, S. Iikubo, K. Kodama, N. Igawa, S. Shamoto, S. Niitaka, M. Azuma, Y. Shimakawa, M. Takano, and F. Izumi, "Neutron Powder Diffraction Study on the Crystal and Magnetic Structures of $BiCoO_3$," *Chem. Mater.*, vol. 18, no. 5, pp. 798–803, 2006.

[72] P. Machado, M. Scigaj, J. Gazquez, E. Rueda, A. Sanchez, I. Fina, M. Gibert-roca, T. Puig, X. Obradors, M. Campoy-quiles, and M. Coll, "Band Gap Tuning of Solution-Processed Ferroelectric Perovskite $BiFe_{1-x}Co_xO_3$ Thin Films," *Chem. Mater.*, vol. 31, pp. 947–954, 2019.

[73] Q. Xu, M. Sobhan, Q. Yang, F. Anariba, K. P. Ong, and P. Wu, "The role of Bi

vacancies in the electrical conduction of $BiFeO_3$: a first-principles approach," *Dalt. Trans.*, vol. 43, pp. 10787–10793, 2014.

[74] T. R. Paudel, S. S. Jaswal, and E. Y. Tsymbal, "Intrinsic defects in multiferroic $BiFeO_3$ and their effect on magnetism," vol. 104409, no. November 2011, pp. 1–8, 2012.

[75] G. Geneste, C. Paillard, and B. Dkhil, "Polarons, vacancies, vacancy associations, and defect states in multiferroic $BiFeO_3$," *Phys. Rev. B*, vol. 99, pp. 1–20, 2019.

[76] R. Mazumder and a. Sen, "Effect of Pb-doping on dielectric properties of $BiFeO_3$ ceramics," *J. Alloys Compd.*, vol. 475, pp. 577–580, 2009.

[77] S. Hunpratub, P. Thongbai, T. Yamwong, R. Yimnirun, and S. Maensiri, "Effects of Mn doping on the dielectric relaxations and dielectric response in multiferroic $BiFeO_3$ Ceramics," *J. Supercond. Nov. Magn.*, vol. 25, pp. 1619–1622, 2012.

[78] V. A. Khomchenko, D. A. Kiselev, M. Kopcewicz, M. Maglione, V. V Shvartsman, P. Borisov, W. Kleemann, A. M. L. Lopes, Y. G. Pogorelov, J. P. Araujo, R. M. Rubinger, N. A. Sobolev, J. M. Vieira, and A. L. Kholkin, "Doping strategies for increased performance in $BiFeO_3$," *J. Magn. M*, vol. 321, pp. 1692–1698, 2009.

[79] Y. A. Chaudhari, C. M. Mahajan, and S. T. Bendre, "Synthesis and characterizations of pure and doped nanocrystalline $BiFeO_3$ ceramics by SHS," *Ceram. - Silikaty*, vol. 58, pp. 65–69, 2014.

[80] Y. Wang and X. Qi, "The Effects of Nickel Substitution on Bismuth Ferrite," *Procedia Eng.*, vol. 36, pp. 455–461, 2012.

[81] Y. Jun, W. Moon, C. Chang, H. Kim, S. Ryu, J. Wook, K. Hoon, and S. Hong, "Effects of Nb-doping on electric and magnetic properties in multi-ferroic $BiFeO_3$ ceramics," vol. 135, pp. 133–137, 2005.

[82] B. Malic, D. Feizpour, and J. Holc, "Synthesis of Sodium Potassium Niobate : A Diffusion Couples Study," *J. Am. Ceram. Soc.*, vol. 91, no. 6, pp. 1916–1922, 2008.

[83] X. Qi, J. Dho, and R. Tomov, "Greatly reduced leakage current and conduction mechanism in aliovalent-ion- doped $BiFeO_3$," *Appl. Phys. Lett.*, vol. 86, no. 62903, 2005.

[84] S. J. Kim, "Multiferroic Properties of Ti-doped $BiFeO_3$ Ceramics," vol. 56, no. 1, pp. 439–442, 2010.

[85] M. Kumar and K. L. Yadav, "Study of room temperature magnetoelectric coupling in Ti substituted bismuth ferrite system Study of room temperature magnetoelectric coupling in Ti substituted bismuth ferrite system," vol. 74111, no. 2006, pp. 6–10, 2016.

[86] J. F. Scott, "Ferroelectrics go bananas," *J. Phys. Condens. Matter*, vol. 20, no. 21001, pp. 1–3, 2008.

[87] G. L. Yuan, S. W. Or, Y. P. Wang, Z. G. Liu, and J. M. Liu, "Preparation and multi-properties of insulated single-phase $BiFeO_3$ ceramics," *Solid State Commun.*, vol. 138, pp. 76–81, 2006.

[88] T. Rojac, M. Kosec, and D. Damjanovic, "Large Electric-Field Induced Strain in $BiFeO_3$ Ceramics," *J. Am. Ceram. Soc.*, vol. 94, no. 12, pp. 4108–4111, Dec. 2011.

[89] T. Rojac, M. Kosec, B. Budic, N. Setter, and D. Damjanovic, "Strong ferroelectric domain-wall pinning in $BiFeO_3$ ceramics," *J. Appl. Phys.*, vol. 108, no. 7, p. 74107,

2010.

[90] J. Seidel, L. W. Martin, Q. He, Q. Zhan, A. Rother, M. E. Hawkridge, P. Maksymovych, P. Yu, M. Gajek, N. Balke, S. V Kalinin, S. Gemming, F. Wang, G. Catalan, J. F. Scott, N. A. Spaldin, J. Orenstein, and R. Ramesh, "Conduction at domain walls in oxide multiferroics," *Nat. Mater.*, vol. 8, no. March, pp. 229–234, 2009.

[91] S. Farokhipoor and B. Noheda, "Conduction through 71° domain walls in $BiFeO_3$ thin films," *Phys. Rev. Lett.*, vol. 107, no. September, pp. 3–6, 2011.

[92] T. Rojac, H. Ursic, A. Bencan, B. Malic, and D. Damjanovic, "Mobile domain walls as a bridge between nanoscale conductivity and macroscopic electromechanical response," *Adv. Funct. Mater.*, vol. 25, pp. 2099–2108, 2015.

[93] A. Bencan, G. Drazic, H. Ursic, M. Makarovic, M. Komelj, and T. Rojac, "Domain-wall pinning and defect ordering in $BiFeO_3$ probed on the atomic and nanoscale," *Nat. Commun.*, vol. 11, pp. 1–9, 2020.

[94] J. Seidel, P. Maksymovych, Y. Batra, a. Katan, S. Y. Yang, Q. He, a. P. Baddorf, S. V. Kalinin, C. H. Yang, J. C. Yang, Y. H. Chu, E. K. H. Salje, H. Wormeester, M. Salmeron, and R. Ramesh, "Domain wall conductivity in La-doped $BiFeO_3$," *Phys. Rev. Lett.*, vol. 105, no. November, pp. 2010–2012, 2010.

[95] L. Liu, T. Rojac, D. Damjanovic, M. Di Michiel, and J. Daniels, "Frequency-dependent decoupling of domain-wall motion and lattice strain in bismuth ferrite," *Nat. communi*, vol. 9, pp. 1–10, 2018.

[96] V. S. Postnikov, V. S. Pavlov, S. K. Turkov, and V. Polytechnicai, "Internal friction in ferroelectrics," *J. Phys. Chem. Solids*, vol. 31, pp. 1785–1791, 1970.

[97] Y. Yoneda and W. Sakamoto, "Electronic and local structures of $BiFeO_3$," *J. Phys. Condens. Matter*, vol. 23, no. 15902, 2011.

[98] J. Anthoniappen, W. Sea, A. Kah, C. Tu, and P. Vashan, "Electric field induced nanoscale polarization switching and piezoresponse in Sm and Mn co-doped $BiFeO_3$ multiferroic ceramics by using piezoresponse force microscopy," *Acta Mater.*, vol. 132, pp. 174–181, 2017.

[99] J. Lv and J. Wu, "Defect dipole-induced poling characteristics and ferroelectricity of quenched bismuth ferrite-based ceramics," *J. Mater. Chem. C*, vol. 4, pp. 6140–6151, 2016.

[100] T. P. Comyn, S. P. McBride, and a. J. Bell, "Processing and electrical properties of $BiFeO_3$–$PbTiO_3$ ceramics," *Mater. Lett.*, vol. 58, pp. 3844–3846, 2004.

[101] D. Wang, G. Wang, S. Murakami, Z. Fan, A. Feteira, D. Zhou, S. Sun, Q. Zhao, and I. M. Reaney, "$BiFeO_3$-$BaTiO_3$: A new generation of lead-free electroceramics," vol. 8, no. 6, pp. 1–35, 2018.

[102] T. Stevenson, D. G. Martin, P. I. Cowin, a. Blumfield, A. J. Bell, T. P. Comyn, and P. M. Weaver, "Piezoelectric materials for high temperature transducers and actuators," *J. Mater. Sci. Mater. Electron.*, vol. 26, no. 12, pp. 9256–9267, 2015.

[103] T. P. Comyn, A. J. Bell, and M. Lyons, "Development of New High Temperature Piezoelectric Materials," *IEEE Int. Symp. Appl. Ferroelectr.*, vol. 15, pp. 232–235, 2006.

[104] S. M. Selbach, M. Einarsrud, and T. Grande, "On the Thermodynamic Stability of

$BiFeO_3$," no. 7, pp. 169–173, 2009.

[105] M. S. Bernardo, T. Jardiel, M. Peiteado, A. C. Caballero, and M. Villegas, "Reaction pathways in the solid state synthesis of multiferroic $BiFeO_3$," *J. Eur. Ceram. Soc.*, vol. 31, pp. 3047–3053, 2011.

[106] R. D. Shannon, "Revised effective ionic radii and systematic studies of interatomic distances in halides and chalcogenides," *Acta Crystallogr. Sect. A*, vol. 32, pp. 751–767, 1976.

[107] "TOPAS version 2.1, Bruker AXS." .

[108] D. Wilcox, B. Dove, M. D., and D. Greer, "UTHSCSA Image Tool for Windows." University of Texas Health Science Center, San Antonio, 2002.

[109] W. H. Walton, "Feret's Statistical Diameter as a Measure of Particle Size," *Nature*, vol. 162, pp. 329–330, 1948.

[110] J. M. Lebeau and S. S. Ã, "Ultramicroscopy Experimental quantification of annular dark-field images in scanning transmission electron microscopy," *Ultramicroscopy*, vol. 108, pp. 1653–1658, 2008.

[111] K. Koch, "Determination of core structure periodicity and point defect density along dislocations," Arizona State University, 2002.

[112] S. Gyergyek, D. Makovec, A. Kodre, I. Arčon, M. Jagodič, and M. Drofenik, "Influence of synthesis method on structural and magnetic properties of cobalt ferrite nanoparticles," *J. Nanoparticle Res.*, vol. 12, pp. 1263–1273, 2010.

[113] K. Mori, T. Kamiyama, H. Kobayashi, K. Oikawa, T. Otomo, and S. Ikeda, "Structural Evidence for the Charge Disproportionation of Fe^{4+} in $BaFeO^3$," *J. Phys. Soc. Japan*, vol. 72, no. 8, pp. 2024–2028, 2003.

[114] The Institute of Electrical and Electronics Engineers, "IEEE standard on piezoelectricity IEEE 176–1987," 1988.

[115] *Piezoelectric Ceramics: Principles and Applications*. Mackeyville, Pennsylvania: APC International Ltd., 2002.

[116] I. Wærnhus, P. Erik, R. Holmestad, T. Grande, and K. Wiik, "Electronic properties of polycrystalline $LaFeO_3$. Part I : Experimental results and the qualitative role of Schottky defects," *Solid State Ionics*, vol. 176, pp. 2783–2790, 2005.

[117] G. Kresse and J. Furthmuller, "Efficient iterative schemes for ab initio total-energy calculations using a plane-wave basis set," *Phys. Rev. B*, vol. 54, no. 16, pp. 169–186, 1996.

[118] G. Kresse and D. Joubert, "From ultrasoft pseudopotentials to the projector augmented-wave method," *Phys. Rev. B*, vol. 59, no. 3, pp. 11–19, 1999.

[119] P. E. Blochl, "Projector augmented-wave method," *Phys. Rev. B*, vol. 50, no. 24, pp. 953–979, 1994.

[120] J. P. Perdew, K. Burke, and M. Ernzerhof, "Generalized Gradient Approximation Made Simple," *Phys. Rev. Lett.*, vol. 77, no. 18, pp. 3865–3868, 1996.

[121] S. L. Dudarev, G. A. Botton, S. Y. Savrasov, C. J. Humphreys, and A. P. Sutton, "Electron-energy-loss spectra and the structural stability of nickel oxide:," *Phys. Rev. B*, vol. 57, no. 3, pp. 1505–1509, 1998.

[122] T. Kanai, S. Ohkoshi, and K. Hashimoto, "Magnetic, electric, and optical functionalities of $(PLZT)_x(BiFeO_3)_{1-x}$ ferroelectric – ferromagnetic thin films," *J.*

Phys. Chem. Solids, vol. 64, no. 3, pp. 391–397, 2003.

[123] F. Gao, Y. Yuan, K. F. Wang, X. Y. Chen, F. Chen, and J. M. Liu, "Preparation and photoabsorption characterization of $BiFeO_3$ nanowires," *Appl. Phys. Lett.*, vol. 89, no. 102506, 2006.

[124] I. Sosnowska, W. Schaffer, W. Kockelmann, K. H. Andersen, and I. O. Troyanchuk, "Crystal structure and spiral magnetic ordering of $BiFeO_3$ doped with manganese," *Appl. Phys. A Mater. Sci. Process.*, vol. 74, pp. S1040–S1042, 2002.

[125] R. P. Feynman, "Forces in Molecules," *Phys. Rev.*, vol. 56, pp. 340–343, 1939.

[126] I. Sosnowska and P. Fischer, "Investigation of crystal and magnetic structure of $BiFeO_3$ using neutron diffraction," *Acta Phys. Pol. A*, vol. 86, no. 4, pp. 629–631, 1994.

[127] G. P. Francis and M. C. Payne, "Finite basis set corrections to total energy pseudopotential calculations," *J. physics. Condens. matter*, vol. 2, no. 4395, p. 4404, 1990.

[128] W. Tang, E. Sanville, and G. Henkelman, "A grid-based Bader analysis algorithm without lattice bias," *J. Phys. Condens. Matter*, vol. 21, no. 84204, 2009.

[129] L. Xia, "Interactions between point defects and internal interfaces in bismuth ferrite," Norwegian University of Science and Technology, 2019.

[130] M. F. Yan and D. W. Johnson, "Impurity-Induced Exaggerated Grain Growth in Mn-Zn Ferrites," *J. Am. Ceram. Soc.*, vol. 61, no. 7, pp. 342–349, 1974.

[131] S. Jyomura, I. Matsuyama, and G. Toda, "Anomalous Grain Growth in PLZT Ceramics," *Commun. Am. Soc.*, no. March, pp. 1–2, 1981.

[132] M. S. Bernardo, T. Jardiel, M. Peiteado, F. J. Mompean, M. Garcia-Hernandez, M. a. Garcia, M. Villegas, and a. C. Caballero, "Intrinsic compositional inhomogeneities in bulk Ti-doped $BiFeO_3$: Microstructure development and multiferroic properties," *Chem. Mater.*, vol. 25, pp. 1533–1541, 2013.

[133] J. Hrescak, G. Drazic, M. Deluca, I. Arcon, M. Dapiaggi, T. Rojac, B. Malic, and A. Bencan, "Donor doping of $K_{0.5}Na_{0.5}NbO_3$ ceramics with strontium and its implications to grain size, phase composition and crystal structure," *J. Eur.*, vol. 37, pp. 2073–2082, 2017.

[134] D. Maurya, H.-C. Song, M.-G. Kang, Y. Yan, R. Bodnar, I. Levine, E. Behnke, H. Borsodi, J. Collar, and S. Priya, "Piezoelectric Response of Sn and Mn Modified Lead Titanate Piezoelectric Ceramics," in *Processing, Properties, and Design of Advanced Ceramics and Composites*, First., G. Singh, A. Bhalla, M. Mahmoud, R. Castro, N. Bansal, D. Zhu, J. O. Singh, and Y. Wu, Eds. 2016, pp. 99–105.

[135] I. Mahmud, M. Yoon, and S. Ur, "Antimony Oxide-Doped $0.99Pb(Zr_{0.53}Ti_{0.47})O_3$–$0.01Bi(Y_{1-x}Sbx)O_3$ Piezoelectric Ceramics for Energy-Harvesting Applications," *Appl. Sci.*, vol. 7, no. 960, pp. 7–10, 2017.

[136] N. M. Rahaman, *Ceramic Processing and Sintering*, 2nd ed. Taylor & Francis Group, LLC, 2003.

[137] C. A Randall, N. Kim, J.-P. Kucera, W. Cao, and T. R. Shrout, "Intrinsic and Extrinsic Size Effects in Fine-Grained Morphotropic-Phase-Boundary Lead Zirconate Titanate Ceramics," *J. Am. Ceram. Soc.*, vol. 81, pp. 677–688, 1998.

[138] T. Hoshina, S. Hatta, H. Takeda, and T. Tsurumi, "Grain size effect on piezoelectric

properties of $BaTiO_3$ ceramics," *Jpn. J. Appl. Phys.*, vol. 57, no. 0902BB, 2018.

[139] T. Schenk, E. Yurchuk, S. Mueller, U. Schroeder, S. Starschich, U. Böttger, and T. Mikolajick, "About the deformation of ferroelectric hystereses," vol. 41103, pp. 0–14, 2014.

[140] A. K. Jonscher, *Dielectric Relaxation in Solids*. London: Chelsea Dielectrics Press Limited, 1983.

[141] Z. Zhang, P. Wu, L. Chen, J. Wang, Z. Zhang, P. Wu, L. Chen, and J. Wang, "Density functional theory plus U study of vacancy formations in bismuth ferrite," *Appl. Phys. Lett.*, vol. 96, no. 23, pp. 210–213, 2010.

[142] N. S. Bein, P. Machado, M. Coll, F. Chen, M. Makarovic, T. Rojac, and A. Klein, "Electrochemical Reduction of Undoped and Cobalt-Doped $BiFeO_3$ Induced by Water Exposure: Quantitative Determination of Reduction Potentials and Defect Energy Levels Using Photoelectron Spectroscopy," *J. Phys. Chem. Lett.*, vol. 10, pp. 7071–7076, 2019.

[143] K. Uchino, "Loss mechanisms in piezoelectrics: How to measure different losses separately," *IEEE Trans. Ultrason. Ferroelectr. Freq. Control*, vol. 48, no. 1, pp. 307–321, 2001.

[144] S. Zhang and T. R. Shrout, "Relaxor-PT Single Crystals : Observations and Developments," *IEEE Trans. Ultrason. Ferroelectr. Freq. Control*, vol. 57, no. 10, pp. 2138–2146, 2010.

[145] Y.-R. Zhang, J.-F. Li, B.-P. Zhang, and C.-E. Peng, "Piezoelectric and ferroelectric properties of lead-free piezoelectric ceramics," *J. Appl. Phys.*, vol. 74109, no. April 2008, 2008.

[146] C. Sakaki, B. Newalkar, S. Komarneni, and K. Uchino, "Grain Size Dependence of High Power Piezoelectric Characteristics in Nb Doped Lead Zirconate Titanate Oxide Ceramics," *Jpn. J. Appl. Phys.*, vol. 40, pp. 6907–6910, 2001.

[147] N. Bein, "The Fermi Level in Bismuth Ferrite," Technical University Darmstadt, 2018.

[148] M. I. Morozov, M.-A. Einarsrud, and T. Grande, "Atmosphere controlled conductivity and Maxwell-Wagner relaxation in $Bi_{0.5}K_{0.5}TiO_3$—$BiFeO_3$ ceramics," *J. Appl. Phys.*, vol. 115, p. 44104, 2014.

[149] G. Catalan and J. F. Scott, "Physics and Applications of Bismuth Ferrite," *Adv. Mater.*, vol. 21, no. 24, pp. 2463–2485, Jun. 2009.

[150] T. Rojac, M. Makarovic, J. Walker, H. Ursic, D. Damjanovic, and T. Kos, "Piezoelectric response of $BiFeO_3$ ceramics at elevated temperatures," vol. 42904, pp. 1–5, 2016.

[151] J. Mizusaki, T. Sasamoto, R. Cannon, and K. Bowen, "Electronic Conductivity, Seebeck Coefficient, and Defect structure of $La_{1-x}Sr_xFeO_3$ (x=0.1, 0.25)," *J. Am. Ceram. Soc.*, vol. 66, no. 4, pp. 247–252, 1983.

[152] H. Ju and J. Kim, "Chemically Exfoliated SnSe Nanosheets and Their SnSe/Poly(3,4-ethylenedioxythiophene):Poly(styrenesulfonate) Composite Films for Polymer Based Thermoelectric Applications," *ACS Nano*, vol. 10, pp. 5730–5739, 2016.

[153] P. Lunkenheimer, V. Bobnar, A. V Pronin, A. I. Ritus, A. A. Volkov, and A. Loidl,

"Origin of apparent colossal dielectric constants," *Phys. Rev. B*, vol. 66, p. 52105, 2002.

[154] A. Y. Kim, Y. J. Lee, and J. S. Kim, "Ferroelectric Properties of $BiFeO_3$ Ceramics Sintered under Low Oxygen Partial Pressure," vol. 60, no. 1, pp. 83–87, 2012.

[155] S. H. Skjærvø, E. T. Wefring, S. K. Nesdal, N. H. Gaukås, G. H. Olsen, J. Glaum, T. Tybell, and S. M. Selbach, "Interstitial oxygen as a source of p-type conductivity in hexagonal manganites," *Nat. Commun.*, vol. 7, 2016.

[156] M. Varenberg, I. Etsion, and G. Halperin, "Crosstalk problems in scanning-by-probe atomic force microscopy," *Rev. Sci. Instrum.*, vol. 74, no. 7, 2003.

[157] R.-A. Eichel, "Structural and dynamic properties of oxygen vacancies in perovskite oxides — analysis of defect chemistry by modern multi-frequency and pulsed EPR techniques," *Phys. Chem. Chem. Phys.*, vol. 13, pp. 368–384, 2011.

[158] S. Hoffman, J. Goslar, and S. Lijewski, "Electron Paramagnetic Resonance and Electron Spin Echo Studies of Co^{2+} Coordination by Nicotinamide Adenine Dinucleotide (NAD^+) in Water Solution," *Appl. Magn. Reson.*, vol. 44, pp. 817–826, 2013.

[159] D. M. Jenkins, A. J. Di Bilio, M. J. Allen, T. A. Betley, and J. C. Peters, "Elucidation of a Low Spin Cobalt (II) System in a Distorted Tetrahedral Geometry," *J. Am. Chem. Soc.*, vol. 124, no. 51, pp. 15336–15350, 2002.

[160] H. Drulis, K. Dyrek, K. P. Hoffmann, S. K. Hoffmann, and A. Weselucha-Birczynska, "EPR Spectra of Low-Symmetry Tetrahedral High-Spin Cobalt (II) in a Cinchoninium Tetrachlorocobaltate (II) Dihydrate Single Crystal," *Inorg. Chem.*, vol. 24, no. 24, pp. 4009–4012, 1985.

[161] C. Mitra, C. Lin, A. B. Posadas, and A. A. Demkov, "Role of oxygen vacancies in room-temperature ferromagnetism in cobalt-substituted $SrTiO_3$," *Phys. Rev. B*, vol. 90, no. April, p. 125130, 2014.

[162] D. Damjanovic and M. DeMartin, "Contribution of the irreversible displacement of domain walls to the piezoelectric effect in barium titanate and lead zirconate titanate ceramics," *J. Phys. Condens. Matter*, vol. 9, pp. 4943–4953, 1997.

[163] J. B. Neaton, C. Ederer, U. V Waghmare, N. A. Spaldin, and K. M. Rabe, "First-principles study of spontaneous polarization in multiferroic $BiFeO_3$," *Phys. Rev. B*, vol. 71, no. 14113, pp. 1–8, 2005.

[164] B. Jiang and S. M. Selbach, "Local and average structure of Mn- and La-substituted $BiFeO_3$," *J. Solid State Chem.*, vol. 250, no. March, pp. 75–82, 2017.

[165] F. A. Kroger and H. J. Vink, "Relations between the Concentrations of Imperfections in Crystalline Solids," *Solid State Phys.*, vol. 3, pp. 307–435, 1956.

[166] M. Eldrup, "Positron Methods for the Study of Defects in Bulk Materials," *J. Phys. IV Colloq.*, vol. 5, no. C1, pp. C1-93-C1-109, 1995.

Bibliography

Publications Related to the Thesis

Journal Articles

M. Makarovič, N. Kanas, A. Zorko, K. Žiberna, H. Uršič Nemevšek, D.R. Småbråten, S.M. Selbach, T. Rojac, "Tailoring the electrical conductivity and hardening in $BiFeO_3$ ceramics," *Journal of the European Ceramic Society,* vol. 40, no. 15, pp. 5483-5493, 2020.

M. Makarovič, M. Çağri Bayir, H. Uršič Nemevšek, A. Bradeško, T. Rojac, "Domain wall conductivity as the origin of enhanced domain wall dynamics in polycrystalline $BiFeO_3$," *Journal of Applied Physics,* vol. 128, no. 6, pp. 064104-1-064104-9, 2020.

T. Rojac, A. Benčan, G. Dražić, N. Sakamoto, H. Uršič Nemevšek, B. Jančar, G. Tavčar, M. Makarovič, J. Walker, B. Malič, D.. Damjanović, "Domain-wall conduction in ferroelectric $BiFeO_3$ controlled by accumulation of charged defects," *Nature Materials,* vol. 16, no. 3, pp. 322-327, 2017.

N. Bein, P. Machado, M. Coll, F. Cheng, M. Makarovil, T. Rojac, A. Klein, "Electrochemical reduction of undoped and cobalt-doped $BiFeO_3$ induced by water exposure: quantitive determination of reduction potentials and defect energy levels using photoelectron spectroscopy," *The Journal of Physical Chemistry Letters,* vol. 10, no. 21, pp. 7071-7076, 2019.

A. Benčan, G. Dražić, H. Uršič Nemevšek, M. Makarovič, M. Komelj, T. Rojac, "Domain-wall pinning and defect ordering in $BiFeO_3$ probed on the atomic nanoscale," *Nature Communications,* vol. 11, pp. 1762-1-1762-8, 2020.

Published scientific conference contribution abstract

M. Makarovič, A. Benčan, B. Malič, T. Rojac, "Tailoring the conductivity of lead-free $BiFeO_3$-based piezoelectric ceramics," in: *Program and book of abstracts.* 25th International Conference on Materials and Technology, October 16-19, 2017, Portorož, Slovenia.

M. Makarovič, T. Rojac, "Effect of cobalt doping on electrical conductivity and electromechanical behavior of $BiFeO_3$ ceramics," in: Conference proceedings 2018.54th International Conference on Microelectronics, Devices and Materials& the Workshop on Sensors and Transducers, October 3-5, 2018, Ljubljana, Slovenia.

M. Makarovič, N. Kanas, D.R. Småbråten, S.M. Selbach, J. Koruza, T. Rojac, "The influence of cobalt doping and annealing atmosphere on electrical conductivity and electromechanical behavior of $BiFeO_3$ ceramics," in: *Joint ISAF-ICE-EMF-IWPM-PFM meeting.* 2019 IEEE International Symposium on Applications of Ferroelectrics (ISAF), July 14-19, 2019, Lausanne, Switzerland.

Other Publications

Journal Articles

E. Khomyakova, J. Pavlič, M. Makarovič, H. Uršič Nemevšek, J. Walker, T. Rojac, B. Malič, A. Benčan, "Integration of $BiFeO_3$ thick film onto ceramic and metal substrates by screen printing," *Journal of the European Ceramic Society,* vol. 35, no. 15, pp. 4163-4171, 2015.

T. Rojac, M. Makarovič, J. Walker, H. Uršič Nemevšek, D. Damjanović, T. Kos, "Piezoelectric response of $BiFeO_3$ ceramics at elevated temperatures," *Applied Physics Letters,* vol. 109, no. 4, pp. 042904-1-042904-4, 2016.

E. Khomyakova, J. Pavlič, M. Makarovič, H. Uršič Nemevšek, J. Walker, V. Shur, T. Rojac, B. Malič, A. Benčan, "Screen printed $BiFeO_3$ thick films on noble metal foils," *Ferroelectrics,* vol. 496, no. 1, pp. 196-203, 2016.

M. Makarovič, J. Walker, E. Khomyakova, A. Benčan, B. Malič, T. Rojac, "Control of electrical conductivity in $0.7BiFeO_3$-$0.3SrTiO_3$ ferroelectric ceramics via thermal treatment in nitrogen atmosphere and Mn doping," *Informacije MIDEM,* vol. 46, no. 3, pp. 154-159, 2016.

J. Ormstrup, M. Makarovič, M. Majkut, T. Rojac, J. Walker, H. Simons, "Dynamics and grain orientation dependence of the electric field induced phase transpormation in Sm modified $BiFeO_3$ ceramics," *Journal of Materials Chemistry C,* vol. 6, no. 18, pp. 7635-7641, 2018.

J. Walker, T. Bayer, M. Makarovič, T. Kos, S. Trolier-McKinstry, B. Malič, T. Rojac, "Cobalt doping to influence the electrical conductivity of $(Bi_{0.91}Dy_{0.09})FeO_3$ ceramics," *Materials letters,* vol. 225, pp. 126-129, 2018.

L. Liu, M. Hinterstein, T. Rojac, J. Walker, M. Makarovič, J.E. Daniels, "In situ study of electric-field-induced ferroelectric and antiferromagnetic domain switching in polycrystalline $BiFeO_3$," *Journal of the American Ceramic Society,* vol. 102, pp. 1768-1775, 2019.

M. Makarovič, A. Benčan, J. Walker, B. Malič, T. Rojac, "Processing, piezoelectric and ferroelectric properties of $(x)BiFeO_3$-$(1\text{-}x)SrTiO_3$," *Journal of the European Ceramic Society,* vol. 39, no. 13, pp. 3693-3702, 2019.

L. Liu, T. Rojac, J. Kimpton, J. Walker, M. Makarovič, J.F. Li, J.E. Daniels, "Poling-induced inverse time-dependent microstrain mechanisms and post-poling relaxation in bismuth ferrite," *Applied Physics Letters,* vol. 116, no. 12, pp. 122901-1-122901-5, 2020.

Published scientific conference contribution abstract

M. Makarovič, J. Walker, E. Khomyakova, A. Benčan, B. Malič, D. Damjanović, T. Rojac, "The potential of polar-to-non-polar phase boundaries in $BiFeO_3$-$SrTiO_3$ piezoelectric ceramics," in: *Piezo2015: Electroceramics for End-Users VIII*, January 25-28, 2015, Maribor, Slovenia.

M. Makarovič, J. Walker, E. Khomyakova, A. Benčan, B. Malič, T. Rojac, "Processing challenges and functional potential of ferroelectric (1-x)$BiFeO_3$-(x)$SrTiO_3$ solid solution," in: *10th Young researchers' day*, March 31, 2016, Ljubljana, Slovenia.

M. Makarovič, J. Walker, E. Khomyakova, A. Benčan, B. Malič, T. Rojac, "Control of electrical conductivity in 0.7$BiFeO_3$-0.3$SrTiO_3$ ferroelectric ceramics via thermal treatment in nitrogen atmosphere and Mn doping," in: *Conference proceedings 2016.* 52nd International Conference on Microelectronics, Devices and Materials & the Workshop on Biosensors and Microfluidics, September 28-30, 2016, Ankaran, Slovenia.

M. Makarovič, J. Walker, A. Benčan, B. Malič, T. Rojac, "Insight into processing, structure and properties of $BiFeO_3$-$SrTiO_3$ ferroelectric ceramics," in: *Piezo2017: Electroceramics for End-Users IX*, February 19-22, 2017, Madrid, Spain.

M. Makarovič, A. Benčan, B. Malič, T. Rojac, "Mechanochemistry – an effective method for producing complex $BiFeO_3$-based high-temperature piezoelectric materials," in: *Program and abstracts.* 9th International Conference on Mechanochemistry and Alloying, September 3-7, 2017, Košice, Slovakia.

M. Makarovič, A. Benčan, B. Malič, T. Rojac, "Processing and properties of lead-free $BiFeO_3$-$SrTiO_3$ piezoceramics," in: *CIMTEC 2018.* 14th International Ceramic Congress & 8th Forum on new Materials, June 10-14, 2018, Perugia, Italy.

M. Makarovič, A. Benčan, H. Simons, J. Walker, J. Ormstrup, T. Rojac, "Exploring the potential of polar-to-non-polar $BiFeO_3$-$SrTiO_3$ ferroelectric solid solution," in: *Electroceramics XVI,* July 9-12, 2018, Hasselt, Belgium.

M. Makarovič, A. Benčan, J. Walker, B. Malič, T. Rojac, "Processing, piezoelectric and ferroelectric properties of (x)$BiFeO_3$-(1-x)$SrTiO_3$," in: *Joint ISAF-ICE-EMF-IWPM-PFM meeting.* 2019 IEEE International Symposium on Applications of Ferroelectrics (ISAF), July 14-19, 2019, Lausanne, Switzerland.

Biography

Maja Makarovič received her BSc degree in 2014 at Department of Inorganic Chemistry at the Faculty of Chemistry and Chemical Technology from the University of Ljubljana, Slovenia. During her bachelor's degree she started to work at Jožef Stefan Institute, Electronic Ceramics Department – K5, under the supervision of Prof. Dr. Tadej Rojac. She became employed at K5 during her MSc study of Nanosciences and Nanotechnologies at the Jožef Stefan International Postgraduate School (JSIPS). In 2016 she received the MSc degree with a thesis on processing and functional characterization of ferroelectric ceramics. In 2016 she became a PhD student of Sensor Technologies at JSIPS under supervision of Prof. Dr. Tadej Rojac and co-supervision of Prof. Dr. Sverre Magnus Selbach from Norwegian University of Science and Technology (NTNU). In 2018 she received a JECS Trust grant for a six-months research visit at NTNU in Trondheim, Norway. In 2019 she went on a one-month research visit to the group of Prof. Dr. Jürgen Rödel at Technical University of Darmstadt. Her research interests are processing and characterization of $BiFeO_3$-based ceramics. Her particular attention is given to the investigation how different types of point defects in $BiFeO_3$ affect functional properties, in particular electrical conductivity and ferroelectric hardening.

Attendance at workshops and courses:

- Winter school on "Advanced Characterization of Piezoceramics" at PIEZO2017, Cercedilla (Madrid), Spain, 19.-22.2.2017.
- Participating in beamtime at The European Synchrotron Radiation Facility (ESRF) on "Kinetics and heterogeneity of the electric-field-induced phase transformation in bismuth ferrite-based multiferroic ceramics", Grenoble, France, 4.-11.7.2017.
- Summer school on "Processing and properties of Electroceramics for Energy applications" at Electroceramics XVI Conference, Hasselt, Belgium, 6.-7.7.2018.
- Workshop on Sensors and Transducers at the 54th International Conference on Microelectronics, Devices and Materials (MIDEM), Ljubljana, Slovenia, 3.-5.10.2018.
- Summer school on "Advanced Materials and Molecular Modelling with Quantum ESPRESSO", Jožef Stefan Institute, Ljubljana, Slovenia, 16.-20.9.2019.

Award:

- Excellent in Science 2017, field Technology, Slovenian Research Agency (co-author of the achievement "Interpretation of electrical conductivity of domain walls in bismuth ferrite".